DEVELOPMENT AND IMPLEMENTATION OF AN EFFICIENT TIME-DOMAIN FACTORIZED WAVE ANALYSIS METHOD FOR DETECTING PIPE LEAKS IN WATER SUPPLY SYSTEMS

MANLI WANG

PhD

The Hong Kong Polytechnic University

2026

The Hong Kong Polytechnic University

Department of Civil and Environmental Engineering

Development And Implementation Of An Efficient Time-Domain Factorized Wave Analysis Method For Detecting Pipe Leaks In Water Supply Systems

Manli Wang

A thesis submitted in partial fulfilment of the requirements for the degree of Doctor of Philosophy

August 2025

CERTIFICATE OF ORIGINALITY

I hereby declare that this thesis is my own work and that, to the best of my knowledge and belief, it reproduces no material previously published or written, nor material that has been accepted for the award of any other degree or diploma, except where due acknowledgement has been made in the text.

_______________ (Signed)

Manli WANG (Name of student)

To my parents

ABSTRACT

As global urbanization accelerates and urban populations continue to grow, concerns over urban water safety, particularly water shortages, are becoming increasingly prominent. Urban water supply systems play a crucial role in water distribution, and their integrity and conveyance efficiency are essential for ensuring a safe and reliable water supply. However, leaks in water distribution networks not only result in significant freshwater and economic losses but also undermine the resilience and long-term sustainability of urban water infrastructure. Nevertheless, achieving fast, accurate, non-intrusive, and wide-ranging leak detection remains a significant challenge. In recent decades, the transient-based method, which utilizes the system information collected by the transient wave, has received immense attention. Among these, the time-domain full-waveform inversion method stands out for its accuracy and robustness by minimizing the discrepancies between the measured and modeled transient signals to identify leaks. However, the inverse analysis requires simultaneous estimation of the coupled leak location and size, resulting in high computational cost and a complex, multidimensional parameter space, especially in large pipe networks. The challenge grows more complex with multiple leaks, where the problem becomes a $2N$-parameter optimization problem (with N being the number of leaks), which is high-dimensional, non-convex, and riddled with local optima. Therefore, a more efficient approach is necessary to enhance the time-domain transient wave analysis and improve the leak detection

technique in the urban water supply systems.

In this thesis, a time-domain factorized wave analysis method is developed. First, a factorized wave model with decoupled leak parameters is analytically derived. Based on this model, an efficient two-stage leak detection algorithm is proposed for single-leak scenarios, which reduces the original two-dimensional optimization to two sequential one-dimensional estimations. For multiple-leak detection, an iterative beamforming algorithm is developed, building on the single leak estimation to decompose the complex $2N$-dimensional optimization problem into $2N$ sequential one-dimensional sub-problems for multiple leak detection. This approach largely reduces the complexity of both forward modeling and inverse estimation, enabling real-time leak localization. Both numerical and experimental applications are applied to validate the proposed time domain factorized wave analysis method for leak detection across different pipe systems. The results confirm its effectiveness and reliability in detecting leaks within both simple and complex pipe systems. Additionally, a sensitivity analysis is performed to assess the method's robustness under various uncertainties, further deepening the understanding of its practical applicability.

The factorized wave model and detection approach developed in this thesis may contribute to advancing the application of current time-domain transient-based methods for leak detection. Based on the findings and achievements presented, recommendations for future research are also provided at the end of the thesis.

LIST OF PUBLICATIONS

Journal papers:

Wang, M., Duan, H. F., Keramat, A., & Che, T. C. (2026). Two-Stage Transient-Based Leak Detection in Water Supply Pipe Networks. *Journal of Hydraulic Engineering*, 152(1), 04025052**.**

Wang, M., Duan, H. F., Chen, Q., Rahmanshahi, M., & Che, T. C. (2025). Time-domain factorized wave model and iterative beamforming for localizing multiple leaks in water pipes. *Water Resources Research*, 61(12), e2025WR041092.

Yan, X. F., Duan, H. F., Wang, X. K., **Wang, M.**, & Lee, P. J. (2021). Investigation of transient wave behavior in water pipelines with blockages. Journal of Hydraulic Engineering, 147(2), 04020095.

Duan, H. F., Pan, B., **Wang, M.**, Chen, L., Zheng, F., & Zhang, Y. (2020). State-of-the-Art Review on the Transient Flow Modeling and Utilization for Urban Water Supply System (UWSS) Management. *Journal of Water Supply: Research and Technology-AQUA*, *69*(8), 858-893.

Wang, M., Duan, H.F., & Che, T.C. (2025). Sensitivity Analysis for Time-Domain Factorized Wave Analysis for Leak Detection in Water Pipelines. Under preparation.

Conference papers:

Wang, M., Pan, B., Keramat, A., Che, T. C., & Duan, H. F. (2024). Development of Efficient Two-Stage Transient-Based Leak Detection Method in Water Pipe Networks. In *15th International Conference on Hydroinformatics* (p. 44).

Pan, B., Duan, H., Che, T., Keramat, A., & **Wang, M.** (2024). Efficient Leakage Detection in Pressurized Looped Pipelines. In *15th International Conference on Hydroinformatics* (p. 329).

Wang, M., Pan, B., Keramat, A., & Duan, H. F. (2023). Efficient Transient Analysis Method for Leak Detection in Pipe Networks. In *40th IAHR World Congress*, 2023 (pp. 3214-3221). International Association for Hydro-Environment Engineering and Research.

Wang, M., Duan, H. F., Zhang, Y., & Keramat, A. (2022). A Holistic Transient Wave Analysis Method for Multiple Defects Detection in Water Pipelines. In *Proceedings of the IAHR World Congress* (pp. 1725-1731). International Association for Hydro-Environment Engineering and Research.

Zhang, Y., Duan, H. F., **Wang, M.**, & Keramat, A. (2022). CFD Investigation of Transient Wave-Blockage Interactions in Water Pipelines. In *Proceedings of the IAHR World Congress* (pp. 1714-1724). International Association for Hydro-Environment Engineering and Research.

ACKNOWLEDGEMENTS

First, I would like to express my sincere gratitude to my supervisor, Prof. Huan-Feng Duan. Throughout my years at PolyU, he has provided unwavering guidance with exceptional professional expertise and has taught me with patience and wisdom, always taking the time to address my questions thoroughly. I feel truly fortunate to have had such a supportive and caring supervisor.

I would also like to express my heartfelt thanks to Dr. Tong-Chuan Che, Dr. Bin Pan, and Dr. Alireza Keramat. During my PhD studies, they generously provided guidance and support with professionalism, patience, and attentive care. Their encouragement and mentorship continually inspired me to make progress in my research.

My sincere thanks go to Prof. Mohamed S. Ghidaoui and Dr. Muhammad Waqar at HKUST for their helpful suggestions on the model development of this study, to Prof. Xun Wang at Beihang University for sharing the MATLAB code, and to the Water Engineering Laboratory (University of Perugia) for the experimental data. I also thank our postdoctoral fellow, Dr. Mostafa Rahmanshahi, for conducting the experiments that supported this research.

Special thanks to Prof. Qing-Zhi Hou for guiding me into the academic field and for providing me with kind support and encouragement through my PhD journey.

I am grateful to PolyU and our department, CEE, for providing the resources and financial support that enabled me to successfully complete my studies, as well as for offering me the opportunity to attend international conferences, which allowed me to engage and exchange ideas with colleagues from around the world.

I am thankful to my group members and dear friends for their company during my years in Hong Kong: Miss Q.R. Chen, Dr. C. Das, Dr. P. Debnath, Mr. T.A. Deng, Ms. L.H. Gan, Miss. M.Y. Ha, Dr. C. He, Dr. U. Herrera, Miss Y.Y. Jia, Miss F. Li, Miss Y.H. Lin, Dr. H.X. Liu, Miss S.M. Liu, Mr. Z.Y. Long, Mr. A. Rahmani, Miss J.Y. Shen, Mr. V. Tjuatja, Dr. Z.H. Xue, Miss Y.H. Zhang (in alphabetical order).

Last but not least, I would like to express my heartfelt gratitude to my parents, Y.W. Wang and A.P. Zhang, for their unconditional love, understanding, and support.

TABLE OF CONTENTS

LIST OF FIGURES

LIST OF TABLES

LIST OF NOTATIONS

A = pipe cross-sectional area

a = wave speed

A_L = leak area

c = constant

C = pipe constraint coefficient

C_d = leak size coefficient

$C_r(\cdot)$ = cross-correlation

D = pipe diameter

df = degrees of freedom

d_i = rank difference

e = pipe wall thickness

E = Young's modulus of pipe elasticity

$\mathbb{E}(\cdot)$ = expectation

$\mathcal{F}$ = external forcing due to the leak

F = norm function

$\mathbf{f}$ = unknown parameter vector

f_s = sampling frequency

g = gravitational acceleration

$\mathbf{G}(x^L)$ = function of leak location

$\tilde{G}$ = Green's function

$\tilde{h}(x^L)$ = transient pressure at the leak

H = pipe pressure head

h = pressure head perturbation

$h(\omega)$ = frequency output

$\tilde{h}$ = head in the frequency domain

H_0 = mean pressure head

H_{L0} = head at the leak location

h^{model} = modeled transient signal

$\hat{h}(n)$ = inverted head magnitude of the peak

h^{NL} = intact transient signal

i = imaginary number

K = bulk modulus of fluid elasticity

k = wave number

k_1, k_2 = empirical coefficients

$\mathcal{L}$ = differential operator

L = length of the pipe section

$\ell(\cdot)$ = log-likelihood function

$\mathbf{n}$ = Gaussian white noise

N = leak number

n = n-th leak

n_i = mode number

P = pressure

$\mathcal{P}(\cdot)$ = the probability

q = discharge perturbation.

Q = pipe discharge

$\tilde{q}$ = discharge in the frequency domain

Q_0 = mean discharge

Q_L = leak discharge

Q_{L0} = steady-state leak discharge

Q_{P0} = pipe section flow rate

R = friction coefficient

R_{nL} = leak-induced damping rate

s = scale parameter

S = success-uncertainty ratio

$\mathbf{s_A}$ = leak size vector

sign(·) = sign function

s^L = leak size

$\hat{s}^L$ = estimated leak size

t = time

t' = a dummy variable

t_1, t_2 = wave transmission times

t_v = closure time

$U(\omega)$ = Fourier transform

U_{ij} = system matrix element

W(·) = weighting function

x = distance along the pipe

$\mathbf{x_A}$ = leak location vector

x^L = leak location

x_L^* = dimensionless leak location.

$\hat{x}^L$ = estimated leak location

x^S is the wave source location

Y = characteristic impedance

$Y(\omega)$ = frequency input

Superscript m, m+1 = upstream and downstream of the pipe section

Superscript U = uncertainty

List of symbols

α, β = coefficients

γ^L = leak size coefficient

δ = the coefficient of variation

$\delta(\cdot)$ = Dirac delta function

Δh = leak-induced transient signal

ΔH_L = pipe internal and external head difference at leak

Δt = time step

Δx = spatial step

Δx^L = distance between two leaks

ε = strain

η = viscosity of viscoelastic material

θ = phase

λ_{min} = minimum probing wavelength

μ = mean value

ρ = fluid density

σ = standard deviation

σ = stress

τ = translation parameter

τ_w = pipe wall shear stress

τ_{ws} = quasi-steady state

τ_{wu} = unsteady state

Φ = unknown leak parameter vector

Ψ = mother wavelet

LIST OF ABBREVIATIONS

1D - one-dimensional

2D - two-dimensional

3D - three-dimensional

AI - artificial intelligence

ANN - artificial neural network

CCTV - Closed-Circuit Television

CFO - central force optimization

CFD - computational fluid dynamics

DMAs - district metered areas

EMD - empirical decomposition method

FDM - Finite Difference Method

FEM - Finite Element Method

FVM - Finite Volume Method

FRF - frequency response function

FWI - full-waveform inversion

GA - genetic algorithms

GPR - ground-penetrating radar

HDPE - high-density polyethylene

IRF - impulse response function

IMFs - intrinsic mode functions

ITA - Inverse transient analysis

K-V model - Kelvin-Voigt model

LM - Levenberg-Marquardt algorithm

MFP - Matched field processing

MOC - Method of Characteristics

ODEs - ordinary differential equations

PDEs - partial differential equations

PSO - particle swarm optimization

PINN - physics-informed neural network

SQP - sequential quadratic programming

SNR - signal-to-noise ratio

TWD - Transient wave damping

TWR - Transient wave reflection

UWSSs - Urban Water Supply Systems

CHAPTER 1 INTRODUCTION

1.1 Research Background

1.1.1 Current status of global UWSS water loss

In modern society, an increasing number of people are choosing to live in cities. Meeting the needs of large urban populations presents a significant challenge for governments, which are responsible for providing high-quality infrastructure and sufficient basic resources, such as freshwater, to ensure the well-being of city residents. Freshwater, as one of the most essential natural and economic resources, has long been a global concern due to issues of shortage and pollution. These challenges affect nearly every aspect of human life, from public health to economic development. Ensuring a sufficient and clean water supply is essential for populations worldwide, making the reliable provision and distribution of freshwater one of the top priorities for all nations (Qin et al., 2011).

Urban Water Supply Systems (UWSSs), responsible for freshwater distribution, serve as the lifeline for billions of urban citizens. Their integrity and efficiency are directly connected to urban water security and public health. Most UWSSs have been buried underground for decades, or even centuries, and over time, prolonged burial leads to the aging and degradation of pipelines and fittings. Continuous exposure to soil and water impurities, internal and external erosion, and the impact of high-pressure flow contribute to the development of various pipe defects, including corrosion, blockages, leaks, and bursts. These issues are often difficult to detect in their early stages, but they gradually compromise the pipeline's structure.

As a result, these defects can lead to freshwater leakage and contamination, increase public health risks, and impose significant financial burdens on local governments and water utilities that strive to provide reliable and comprehensive freshwater services at an affordable cost (Di Pierro et al., 2009; Ostfeld et al., 2008). The global overall water loss rate in UWSS is around 30%, which has been estimated to be 126 billion m3 per year, and its cost value is around 39 billion USD (Liemberger & Marin, 2006; Liemberger & Wyatt, 2019). Figure 1.1 presents the UWSS water loss rate of different counties around the world from Al-Washali (2021), in which a clear regional difference can be observed. Developed regions such as North America, Western Europe, Australia, and Japan exhibit relatively low loss rates, below 20%. In contrast, many countries in Latin America, Africa, the Middle East, and South and Southeast Asia face severe leakage issues with rates exceeding 30% and even surpassing 50% in some.

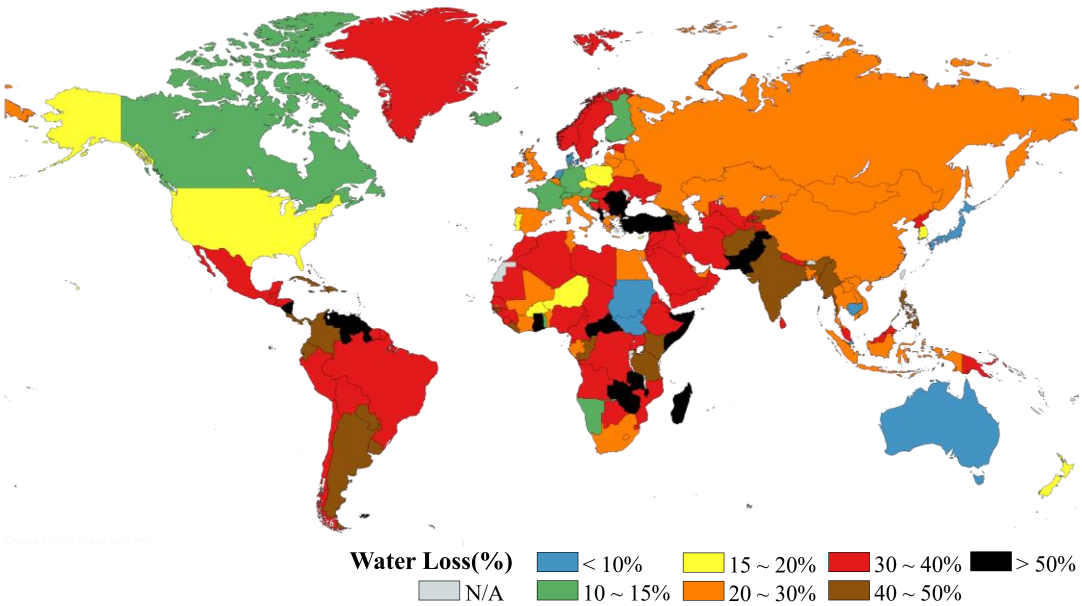

Figure 1.1 World map of UWSS water loss rate (Al-Washali, 2021)

In response to this situation, the replacement or rehabilitation of damaged and aging pipeline infrastructure is urgently needed in many countries and regions, requiring active promotion and substantial investment by local governments. For example, the British government approved 18.7 billion GBP (25 billion USD) for Thames Water from 2025 to 2030, with significant investment allocated to the replacement and rehabilitation of the water pipe system, aiming to reduce the leak rate by 20.1% from the 2022-23 baseline (Ofwat, 2024). In Hong Kong, the government spent around 23 billion HKD (3 billion USD) in the Replacement and Rehabilitation (R&R) Program for 3000 km of aged water mains from 2000 to 2015, resulting in a 98% reduction in pipe burst cases and a significant decrease in water loss (HKWSD, 2025). In recent years, continuous efforts have been made to maintain their enlarged pipe system. In North America, the U.S. and Canada experience more than 260,000 water pipe breaks annually, with 2.6 billion USD in repair expenses each year. Nevertheless, nearly 20% (about 727,500 km) of their water supply pipelines have exceeded their service life but remain unreplaced due to a 452 billion USD funding shortfall (Barfuss & Fugal, 2025). Developing countries and regions, on the other hand, face more severe water shortages and losses, particularly in rapidly growing urban areas. In fact, half of the global water losses occur in these regions, where many utilities are trapped in a vicious revenue cycle, and their customers suffer from intermittent water supply and poor water quality (Liemberger & Marin, 2006). These examples highlight the critical and urgent need for efficient and cost-effective methods of detecting leaks and repairing or replacing water pipelines to maintain a reliable and resilient water supply system.

1.1.2 Common pipe leak detection technologies

Currently, pipe leak detection technologies are commonly grouped into two broad categories, intrusive and non-intrusive methods, based on their operational characteristics and the degree of intervention in the water supply system, providing an intuitive overview of field practices. Intrusive methods involve direct interaction with the pipeline system and often require temporary shutdowns, the injection of detection agents, or physical access through excavation. Typical examples include *the robotic or CCTV inspection*, where a camera-equipped robot is deployed inside the pipeline to capture real-time visual data for defect analysis (Henry & Luxmoore, 1996); and *manual inspection*, which requires excavating the pipeline to assess its condition and identify leaks through direct observation. These methods disrupt the normal operation of the water supply system, require high labor costs, and are time-consuming. Therefore, they are not suitable for large-scale applications.

Non-intrusive methods, represented by acoustic-based methods and ground-penetrating radar, have been widely adopted and achieved commercial success over the decades. Acoustic-based methods work by capturing and analyzing sound signals of specific frequencies generated when water sprays from a leak and strikes the pipe wall and surrounding soil. These signals are then applied to assess the pipe condition and gather information on leaks. Acoustic-based detection often involves specialized hardware devices such as listening rods, leak correlators, and leak noise loggers (Li et al., 2015). These devices rely on different principles, ranging from the noise level caused by a leak to the speed of sound propagation, sound intensity, and frequency (Zhongyu Hu et al., 2021). However, the effectiveness of these methods is highly dependent on the technician's skill and field experience, which in turn leads to relatively high operational costs in terms of both labor and equipment. Additionally, factors such as pipe material, leak size, and environmental noises can significantly influence the acoustic signature, making accurate detection challenging in complex environments and over large areas (Li et al., 2015). Ground-penetrating radar, which utilizes high-frequency electromagnetic waves for the underground pipe systems, faces similar limitations, including high operational costs and reduced accuracy in complex soil environments (Hunaidi, 1998). Other emerging non-intrusive methods include *satellite-based leak detection*, which exploits satellite imagery to identify persistent surface moisture, vegetation anomalies, and ground deformation induced by freshwater leaks (Chen et al., 2020), as well as *fiber-optic sensing* technology, which detects leak-induced acoustic, thermal, or strain disturbances using distributed optical fibers installed along or near pipelines (Wu et al., 2023).

While intrusive and non-intrusive methods mentioned above have been widely used for pipeline investigation under various circumstances, they often face inherent limitations in terms of cost, capability, detection resolution, etc. Few are capable of achieving fast, accurate, non-intrusive, and wide-ranging leak detection while maintaining low operational and maintenance costs. Therefore, it is both important and urgent for researchers to develop a real-time pipeline monitoring method that can detect potential leaks in the system while offering these key advantages (Brunone & Ferrante, 2001; Duan et al., 2011).

1.1.3 Transient-based method for leak detection in UWSSs

The transient-based method is a recently developed solution for investigating water supply systems, offering an improved alternative to traditional acoustic-based detection techniques. Transient wave, also referred to as transient flow, water hammer, or hydraulic shock, is a destructive hydraulic phenomenon in pipelines caused by rapid changes in flow rate, often triggered by the operation of pumps, valves, or pressure fluctuations in reservoirs (Chaudhry, 2014). Initially considered a problematic and unwanted disturbance, the transient wave was widely studied to mitigate its damaging effects. However, it was later discovered to have potential benefits for pipeline health monitoring and defect detection.

The basic principle of the transient-based method is that a transient wave is actively injected into the pipe by actively perturbing the flow field through access points (e.g., a side-discharge valve or a fire hydrant). The injected wave propagates throughout the system with high speed (~ 300m/s in viscoelastic pipes to ~ 1400m/s in elastic pipes) and undergoes additional reflection when encountering physical discontinuities of the pipe, such as junctions, blockages, and leaks, as shown in Figure 1.2 (Chaudhry, 2014). Wave reflections carry information about unknown defect characteristics, such as type, location, and size, which can be inferred through inverse analysis using wave physics and signal processing techniques. For instance, for the case of a leak, when a reflected wave arrives at the sensing station, its amplitude depends on the leak size, while its arrival time depends on the leak location. This information is encoded in the measured pressure transient signals and serves as the basis for estimating leak properties (Capelo et al., 2021; Duan et al., 2011; Ferrante et al., 2007; Keramat et al., 2023; S. Kim, 2022; Zeng et al., 2024; Zhang et al., 2022).

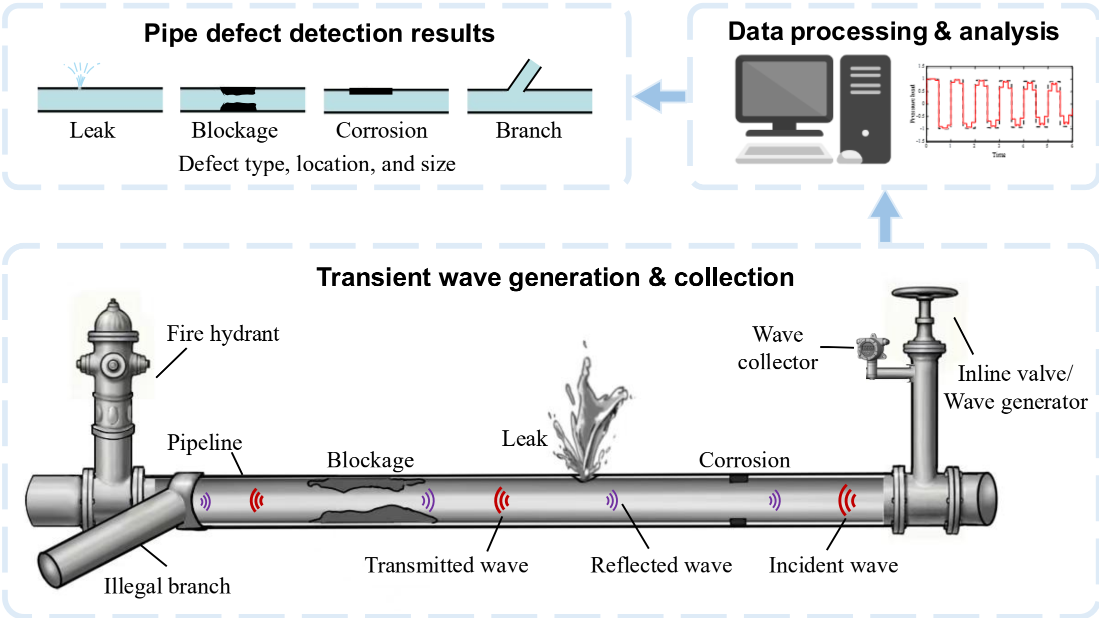

Figure 1.2 Basic principle of the transient-based method

Currently, transient-based leak detection methods can be broadly classified into five main types: the frequency response function (FRF) based method, the transient wave reflection (TWR) based method, the transient wave damping (TWD) based method, the frequency domain matched field processing (MFP) method, and the time-domain full-waveform inversion (FWI) method represented by the inverse transient analysis (ITA) method. Among them, the time-domain FWI method stands out for its robustness, accuracy, and flexibility in signal information utilization. This approach estimates the coupled leak location and size by minimizing the difference between modeled and measured transient signals through multidimensional optimization. However, as system complexity increases, particularly in large pipe network systems, the simultaneous estimation of multiple leak parameters demands a large number of modeled data invocations, resulting in high computational cost and a complex, high-dimensional parameter space. Researchers have studied improving its detection efficiency by optimizing data collection strategies and enhancing optimization techniques, etc. (Kapelan et al., 2004; Sarkamaryan et al., 2018; Shamloo & Haghighi, 2010; Vítkovský, Simpson, et al., 2000; Zhang, Gong, et al., 2018). Despite these advancements, the application of time-domain FWI remains computationally intensive, requiring repeated model invocation and leading to extended processing times and limited detection efficiency. The challenge is further amplified in the presence of multiple leaks, where the problem becomes a $2N$-dimensional optimization (where N represents the number of leaks), which is high-dimensional, non-convex, and plagued by local optima. Therefore, it is necessary to address the low efficiency issue of the time-domain full-waveform inversion to enable its broader application.

In research and pipe system level applications, leak detection technologies are not only distinguished by their operational characteristics (intrusive/non-intrusive), but also organized into more strategic frameworks, which capture scientific approaches such as water balance analyses, inverse modeling, and transient-based methods. To provide a more comprehensive overview of current leak detection methods, the methods are first reviewed in the next chapter, followed by a detailed introduction to the fundamentals and classifications of the transient-based method, which form the theoretical foundation and research focus of this study.

1.2 Research Aim and Objectives

The overall aim of this thesis is to develop an efficient time-domain factorized transient wave analysis framework based on an improved understanding of transient wave dynamics and their interaction with pipe walls. This framework seeks to enhance the computational efficiency and practical applicability of the time-domain full-waveform inversion method for pipeline leak detection, thereby improving the robustness and efficiency of transient-based leak detection in urban water supply systems.

The research aim is divided into three specific objectives, as outlined below. The relationships among these objectives are illustrated in Figure 1.3.

Objective 1: To analytically derive a time-domain factorized wave model and develop an efficient transient wave analysis method for leak detection in UWSSs.

Objective 2: To conduct case studies and discussions on the proposed framework through numerical and experimental studies in both single-pipe systems and pipe network systems.

Objective 3: To conduct sensitivity analysis and evaluate the applicability and robustness of the proposed method under different sources of uncertainty.

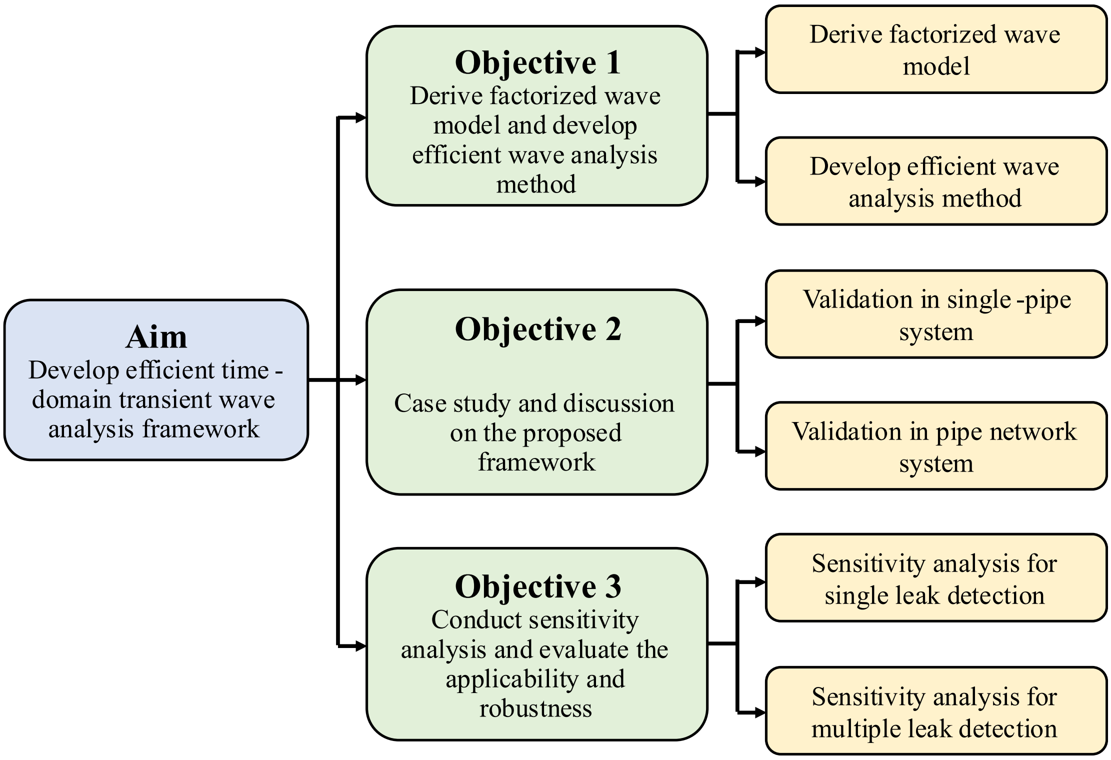

Figure 1.3 Logical structure of the research aim and objectives

1.3 Thesis Outline

The thesis consists of seven chapters. The details are described below:

Chapter 1 provides a brief introduction to the global water loss issue in the urban water supply systems and commonly used leak detection techniques. The concept of transient waves is also preliminarily introduced as the foundation for subsequent chapters.

Chapter 2 gives an extensive literature review of current pipe detection frameworks and methods. The fundamental physics, principles, and simulation techniques of transient waves are reviewed, followed by a detailed review of transient-based leak detection.

Chapter 3 introduces a new time-domain factorized wave analysis model that separates leak location and size, forming the basis for a computationally efficient leak detection method in water pipelines. A combination of an iterative beamforming algorithm and a two-stage process is developed, which reduces the original N-dimensional optimization for leak parameter estimation into two N-dimensional sequential one-dimensional sub-problems. This reduces the complexity of both forward simulation and inverse estimation, making leak localization more efficient.

Chapter 4 presents numerical and experimental case studies in reservoir-pipe-valve (RPV) systems to validate the developed theory and leak detection algorithm for both single and multiple leaks. Additional analyses are conducted to evaluate the applicability and robustness of the proposed method. The results demonstrate its efficiency and effectiveness.

Chapter 5 extends the case studies and discussion to pipe network systems, with a focus on single-leak detection. The feasibility of separating leak parameters is first examined in the network context, followed by a detailed case study of a five-loop network to demonstrate the practicality of the proposed method.

Chapter 6 investigates the sensitivity of the proposed method to uncertainties in single- and multiple-leak detection. Four different types of uncertainty are analyzed, and the results are used to conclude the method's reliability under realistic operating conditions.

Chapter 7 is the summation of the thesis and recommendations for potential future work.

CHAPTER 2 LITERATURE REVIEW

2.1Introduction

As noted in Chapter 1, leakage and water loss have long been one of the major challenges for water supply systems worldwide. To tackle these problems, various monitoring and detection strategies have been developed over the years. Among them, transient-based methods are one of the relatively recent approaches introduced in the past few decades as an alternative to traditional monitoring techniques. This chapter first reviews several classic pipe detection principles and techniques that have been widely applied in practice, followed by a detailed introduction to transient-based methods, emphasizing their underlying theories, implementation strategies, and classification schemes for leak detection in pipeline systems.

2.2 Commonly used pipe control and detection methods

Apart from the operation characteristic-based category for pipe detection methods discussed in the last chapter, a strategic perspective category is adopted to reflect research and system-level applications. Researchers have developed various frameworks to evaluate and manage pipe flow and water leakage, such as water balance analysis, district metered areas (DMAs), inverse modeling, and transient-based wave analysis. These methods not only provide practical applications but also enhance the theoretical understanding of the detection and research of water supply systems.

2.2.1 Water balance and District Metered Areas (DMAs)

The water balance and District Metered Areas method is a traditional and fundamental approach for leak detection in UWSSs. It depends on a calibrated hydraulic model of the network within a DMA (i.e., a small zone subdivided from a larger network system) to monitor inflow and outflow, and compares the model-predicted pressure or flow signals to actual measurement data (Farah & Shahrour, 2024; Puust et al., 2010; Zaman et al., 2020). This method has been widely adopted globally as it enables long-term and relatively independent monitoring of water supply and consumption within specific regions. By applying water balance, areas with high water loss rates can be promptly identified. Farley and Trow (2003) recommended DMA as a key tool for modern water loss management, while Mounce and Boxall (2010) integrated it with artificial neural networks (ANNs) to enhance the detection of unusual water flow. Huang et al. (2020) applied multistage optimal valve operations and smart demand metering for efficient leak localization in DMA.

Despite the advantages, the DMA method requires a significant initial investment in pipe network modifications and hardware installation, and its efficiency relies heavily on the accuracy of metering; inaccurate data measurement can significantly affect the method's reliability. Moreover, DMA can only identify the presence of leaks within a specific area; it cannot pinpoint the leak, so detailed localization generally relies on complementary approaches such as acoustic-based hardware (Farah & Shahrour, 2024).

2.2.2 Inverse hydraulic modeling methods

Inverse hydraulic modeling is a widely used model-based technique. Within a known water supply pipeline system, a steady-state hydraulic model is first established. By inverting and calibrating pipe parameters such as pipe diameter, roughness, and branches, the pipe condition can be assessed through the comparison of the modeled pressure or flow and measured data (Zukang Hu et al., 2021; Kapelan et al., 2003). By introducing and adjusting the virtual leak points and their parameters until the numerical model closely aligns with the observed data, leaks in the pipe can be effectively identified. This method is often applied in combination with DMA and water balance approaches to improve detection accuracy, as it can utilize the long-term water pressure or flow data (Farah & Shahrour, 2024). Nevertheless, similar to DMA, the inverse hydraulic modeling methods require an accurate hydraulic model and precise measurements for simulation and calibration, leading to high computational demand. In addition, it is less sensitive to small-scale water loss, especially when measurement points are limited or environmental noise is strong, hindering accurate leak localization (Zukang Hu et al., 2021; Zaman et al., 2020).

2.2.3 Hardware-based methods

Hardware-based methods, as discussed in the previous chapter, require direct contact with the pipeline and can be categorized into intrusive and non-intrusive methods. Intrusive methods, such as stethoscope , CCTV, and the tracer gas method, provide high detection accuracy of the pipeline and can directly locate the leaks.

However, these methods require the suspension of the regular water running or excavating the pipeline, disrupting the water supply, and involve significant manual labor (Li et al., 2015).

Non-intrusive methods, including acoustic-based methods and ground-penetrating radar (GPR), do not require direct contact with the pipeline. They utilize external media such as noise, electromagnetic waves, or imaging technology. While these methods have minimal impact on pipeline operations, they are typically more expensive, and the detection accuracy is strongly affected by the surrounding environment (Zukang Hu et al., 2021; Zhongyu Hu et al., 2021).

In general, the above-reviewed methods are widely applied for leak detection in UWSSs and have demonstrated success in practical applications and business. Nevertheless, their performance is often constrained by one or more factors, such as cost, method complexity, and sensitivity to the environment. Therefore, it is challenging to achieve good detection efficiency and accuracy over a wide range in a non-intrusive and cost-effective way at the same time. These limitations have motivated the development of transient-based methods. Characterized by high efficiency (from high wave speeds) and non-intrusiveness (due to remote operation), they offer a promising improvement or supplement to existing pipe detection methods.

2.3 Fundamentals of Transient Wave

This section presents the physical foundations of the transient wave propagation, including governing equations , key parameters, and numerical solutions.

2.3.1 Transient propagation and governing equations

2.3.1.1 Transient propagation and wave speed

In a pressurized pipeline, a transient wave is generated by sudden changes in system conditions, such as rapid valve opening/closure, pump operation, or sudden changes in water demand. These events create a pressure disturbance that propagates bidirectionally along the pipeline in the form of a pressure wave. The wave travels and undergoes reflection or transmission when encountered with pipe situations such as defects, branches, material transitions, or boundary conditions. The reflected transient wave contains information about the pipe structure and defects and can be utilized for pipe condition assessment and defect detection (Chaudhry, 2014; Che et al., 2021; Ghidaoui, 2004).

The transient wave speed (a) is defined by (Chaudhry, 2014; Wylie et al., 1993)

$$\frac{1}{a^2} = \frac{d\rho}{dP} + \frac{\rho}{A}\frac{dA}{dP} \tag{2.1}$$

where $P=\rho gH$ is the pressure, ρ is the fluid density, A is the pipe cross-sectional area. For a compressible fluid propagating in a pressurized pipe, the wave speed can be further expressed as

$$a = \sqrt{\frac{K/\rho}{1 + C\dfrac{KD}{Ee}}} \tag{2.2}$$

where K is the bulk modulus of fluid elasticity, C is the pipe constraint coefficient, E is the Young's modulus of pipe elasticity, and e is the pipe wall thickness. The above equations indicate the factors that influence the wave speed, including pipe wall elasticity, pipe diameter and thickness, fluid temperature, and fluid compressibility. Specifically, the fluid compressibility usually depends on factors such as temperature, pressure, and the presence of entrained air, while pipe wall elasticity is affected by the pipe properties and external constraints (e.g., soil compaction and surrounding structures). Therefore, the actual wave speed observed in practice may deviate from the theoretical value with standard parameters, introducing uncertainty into transient modeling and defect detection (Che et al., 2021).

Common water supply pipe materials can be broadly categorized into elastic and viscoelastic types. Elastic pipes, such as steel or copper pipes, have a high Young's modulus and support transient waves with relatively high wave speeds of larger than 1000 m/s. On the other hand, viscoelastic pipes, such as high-density polyethylene (HDPE) and polyvinyl chloride (PVC) pipes, are more compliant and deformable, leading to lower wave speeds in the range of 300 ~ 500 m/s (Ayati et al., 2019). Hence, a relatively accurate wave speed estimation considering pipe material and other factors is essential for transient simulation and reliable pipe condition assessment.

2.3.1.2 Governing equations for one-dimensional transient wave

The transient wave in a pressurized pipeline is commonly modeled by one-dimensional (1D) governing equations for its computational efficiency and physically representative framework for transient-based defect detection (Duan et al., 2020). In this model, the pressure is considered uniform across one pipe section, as illustrated in Figure 2.1. According to Chaudhry (2014), the assumptions for the 1D transient model include: (1) the fluid is slightly compressible; (2) the pipeline is axisymmetric and circular; (3) the effect of radial inertia and shear force is negligible; and (4) pipe wall elasticity and viscoelasticity are considered. Compared with higher-dimensional (2D/3D) models, these assumptions significantly reduce the computational cost while maintaining modeling accuracy, making the 1D model a practical choice for pipe system simulations, as validated in both numerical and experimental applications (Brunone et al., 2022).

The governing equations consist of the continuity and momentum equations. For the 1D simulation of the transient wave in an elastic pipeline, the governing equations are given by (Chaudhry, 2014; Wylie et al., 1993):

$$\frac{gA}{a^2}\frac{\partial H}{\partial t}+\frac{\partial Q}{\partial x}=0 \tag{2.3}$$

$$\frac{\partial Q}{\partial t}+gA\frac{\partial H}{\partial x}+\frac{\pi D}{\rho}\tau_w=0 \tag{2.4}$$

in which H is pipe pressure head, Q is pipe discharge, g is the gravitational acceleration, D is the pipe diameter, x and t are distance along the pipe and time, and τ_w is the pipe wall shear stress, which contributes to the frictional resistance between the fluid and the pipe wall and can be divided into quasi-steady and unsteady two components (Ghidaoui et al., 2005).

In the governing equations, the H and Q represent the instantaneous pressure head and discharge, both of which are functions of time and spatial location. These variables are used to characterize the transient behavior in the governing equations. They can be expressed as (Chaudhry, 2014):

$$H = H_0 + h \tag{2.5}$$

$$Q = Q_0 + q \tag{2.6}$$

in which H_0 = mean pressure head; h = pressure head perturbation; Q_0 = mean discharge; and q = discharge perturbation.

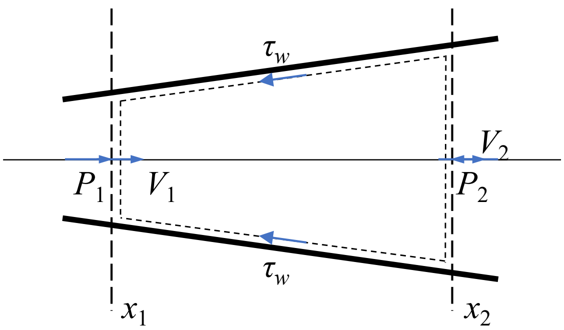

Figure 2.1 Schematic for control volume for 1D transient simulation

The 1D governing equations are commonly employed in the simulation of the evolution of pressure head and the discharge oscillations in the time domain during a transient event. For example, the Method of Characteristics (MOC) transforms the partial differential equations into ordinary differential equations along characteristic lines, allowing time-domain solutions for transient wave propagation (Lister, 1960). The equations are also applied in the frequency domain, where they are linearized, transformed, and solved using the transfer matrix method, which directly relates pressure head and discharge perturbations without spatial discretization (Chaudhry, 2014; Duan et al., 2011; Lee et al., 2005a). A more detailed description of these simulation methods is provided in the following sections.

2.3.1.3 Higher-dimensional transient model

Although the 1D transient model is widely adopted for its easy and efficient practical use, two- and three-dimensional (2D and 3D) models are developed based on the full Navier-Stokes equations for research purposes. These higher-dimensional models help with detailed simulation of the transient wave under conditions such as local turbulence/non-uniform flow, complex boundary conditions (Duan et al., 2009; Zhao & Ghidaoui, 2006; Zielke, 1968). For structural analysis and fluid-structure interaction modeling, computational fluid dynamics (CFD) is employed to capture the behavior (Bergant et al., 2008; Wylie et al., 1993). The CFD is also applied to benchmarking studies for the 1D transient simulation validation(Ghidaoui et al., 2005).

2.3.2 Effects for transient wave dissipation

One fundamental feature of the transient wave propagation in the pressurized pipeline is wave attenuation. The attenuation results from energy dissipation, mainly caused by two effects, pipe wall viscoelasticity and friction losses.

2.3.2.1 Elasticity and viscoelasticity

As mentioned earlier, the transient wave speed largely depends on the pipe wall material, specifically its elasticity or viscoelasticity. Elasticity is the property of a material that enables it to recover its original shape after deformation caused by external loading. In an ideal elastic material, the strain is directly proportional to the applied stress (Wineman & Rajagopal, 2000). Viscoelasticity, on the other hand, is the material property that shows both elastic and viscous behavior when subjected to mechanical loading. Such materials demonstrate time-dependent responses, including delayed deformation (creep) under constant stress, gradual stress relaxation under constant strain, and hysteresis during cyclic loading as a result of internal energy dissipation. The stress-strain curves of both elastic and viscoelastic materials are presented in Figure 2.2 (Ferry, 1980; Meyers & Chawla, 2008). The influence of pipe wall material on wave energy dissipation is a key indirect factor impacting wave speed. In particular, pipe-wall viscoelasticity introduces time-dependent deformation and internal energy dissipation during transient events, which is incorporated into the governing equations through the pressure-deformation relationship (Duan et al., 2020).

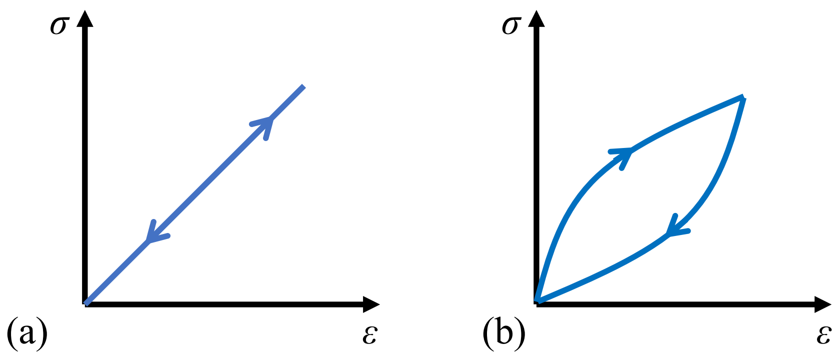

Figure 2.2 The stress-strain curves : (a) elastic material; (b) viscoelastic material

In elastic pipes, pipe deformation is instantaneously recovered after compression, allowing for negligible energy dissipation for the transient wave in an elastic pipe, and wave attenuation is governed primarily by frictional losses (Meyers & Chawla, 2008). In contrast, viscoelastic pipes exhibit significantly increased energy dissipation during transient events due to the time-dependent deformation of the pipe wall, with the mechanical response divided into an instantaneous elastic response and a viscoelastic/retarded response (Covas et al., 2005; Covas et al., 2004). The Kelvin-Voigt model (K-V model) is widely applied to simulate viscoelasticity. It consists of a linear spring and a dashpot arranged in parallel. This configuration enables the material to resist deformation elastically in the short term while gradually undergoing strain under sustained loading. By incorporating this viscoelastic behavior, the model introduces time-dependent storage and dissipation effects that influence wave propagation and pressure responses in the governing equations. The structure of the K-V model is shown in Figure 2.3, and its mathematical expression is given by (Che et al., 2021; Covas et al., 2005)

$$\sigma(t) = E\varepsilon(t) + \eta \frac{d\varepsilon(t)}{dt} \tag{2.7}$$

where σ is stress, ε is strain; E is Young's modulus, and η is the viscosity of the viscoelastic material.

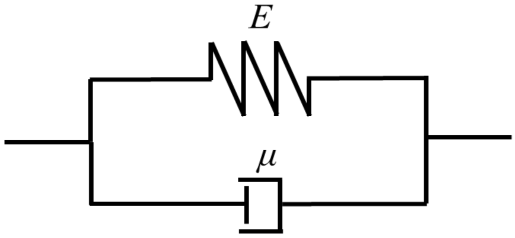

Figure 2.3 Structure of K-V model

In the case of a transient event, pressure waves in viscoelastic pipes gradually lose energy as they propagate, and the waves typically show a reduced peak amplitude and an increased rise time compared to those in elastic systems, which has been consistently observed in both experimental and numerical studies (Covas et al., 2004; Pan et al., 2022; Soares et al., 2011; Tjuatja et al., 2023; Urbanowicz et al., 2020). Accurate characterization and numerical representation of this dissipative behavior are essential for transient wave simulation and condition assessment in viscoelastic pipelines.

2.3.2.2 Steady friction and unsteady friction

During the transient wave propagation, the signal attenuation primarily comes from two main effects: viscoelasticity and friction. Friction arises from the energy dissipated by shear stress at the fluid-pipe wall interface. The pipe wall shear stress τ_w represents the frictional resistance between the fluid and the pipe wall. As described in Ghidaoui et al. (2005), it can be divided into quasi-steady and unsteady parts, given by

$$\tau_w = \tau_{ws} + \tau_{wu} \tag{2.8}$$

where τ_{ws} is the quasi-steady part, and τ_{wu} is the unsteady part.

In the 1D transient modeling, the 1D quasi-steady friction model is typically represented by the Darcy-Weisbach model for its explicit expression and computational efficiency (Chaudhry, 2014). In this model, the wall shear stress is expressed as:

$$\tau_w = \frac{f\rho|V|V}{8} \tag{2.9}$$

where f is the pipeline Darcy-Weisbach friction factor, and v is the flow rate. It is indicated from the equation that the steady friction is proportional to the square of the flow rate. This expression is efficient and straightforward, making it widely adopted in practical simulations. However, it can only describe the average energy loss along the pipe and therefore underestimates the damping of pressure oscillations, particularly in the case of long-term propagation and viscoelastic pipes, where the transient wave would distort the velocity profile and potentially lead to flow reversal near the pipe boundary (Duan et al., 2020).

Various unsteady-friction models have been established to describe the unsteadiness of the transient wave. Some of the commonly used 1D unsteady friction models are summarized below (Bergant et al., 2001; Norooz et al., 2015):

(1) Zielke model (Zielke, 1968): It is a weighting function-based model with a convolution integral formulation and is a classic for laminar unsteady friction. It is expressed as

$$\tau_{wu}(t) = -\int_0^t W(t-t')\frac{\partial Q(t')}{\partial t'}dt' \tag{2.10}$$

where t' is a dummy variable representing the instantaneous time in the time history, W (·) is the weighting function. The model was extended to turbulence by Vardy and Hwang (1991), and subsequently enhanced its computational efficiency by Vardy and Brown (1995, 2004) for practical engineering use.

(2) Brunone model (Brunone et al., 1991; Brunone et al., 1995) presents the unsteady friction as a linear combination of local and convective accelerations, avoiding the computational complexity associated with the convolution in the Zielke model series, making it more suitable for practical applications (Ghidaoui et al., 2005; Norooz et al., 2015). The expression is given by:

$$\tau_{wu} = k_1 \frac{\partial V}{\partial t} + k_2 \frac{\partial V}{\partial x} \tag{2.11}$$

where $\partial V / \partial t$ is the local acceleration term, $\partial V / \partial x$ is the convective acceleration term. k_1 and k_2 are the empirical coefficients that require experimental determination and collaboration, which introduce uncertainties and reduce the accuracy of the model.

Other researchers also proposed models to describe unsteady friction. For example, Trikha (1975) and Schohl (1993) replaced and improved the approximate weighting function of the Zielke model, while Vítkovský, Lambert, et al. (2000) reduced the computational cost of Zielke's convolution integral (Ghidaoui et al., 2005). The continuous development of both quasi-steady and unsteady friction contributes to the transient-based leak detection, as the collaborative parameters and wave attenuation characteristics can provide insights into the system feature, and thus support a better understanding of pipeline condition.

Building on the preceding discussion of pipe viscoelasticity and friction effects, the governing equations can be further expressed as

$$\frac{gA}{a^2} \frac{\partial H}{\partial t} + \frac{\partial Q}{\partial x} = 0 \tag{2.12}$$

$$\frac{\partial Q}{\partial t} + gA\frac{\partial H}{\partial x} + R_v(Q,t) + R_f(Q,t) = 0 \qquad (2.13)$$

in which R_v is the K-V term as given in Eq. (2.7), and R_f is the steady or unsteady friction term as given in Eqs. (2.9) - (2.11).

2.3.3 Numerical solution techniques for the transient wave

To simulate transient wave propagation in pressurized pipelines, various numerical solutions have been developed based on the governing equations and the physical principles introduced in the previous sections. This section reviews common numerical simulation techniques for transient waves based on the commonly used 1D transient model in both the time and frequency domains.

2.3.3.1 Time domain solution

Time domain solutions simulate the transient wave by solving the partial differential governing equations to obtain the instantaneous pressure and flow fluctuations, such as finite difference, finite volume, etc (Amein & Chu, 1975; Chaudhry & Hussaini, 1985; Suo & Wylie, 1989; Wylie et al., 1993). Among these approaches, the Method of Characteristics (MOC) is a classic time domain approach for solving the 1D transient governing equations.

Method of Characteristics (MOC)

The MOC has been widely adopted in transient-based pipe detection for its clear physical interpretation, numerical stability, effective boundary condition processing, and computational efficiency (Che et al., 2021; Ghidaoui et al., 2005; Lister, 1960). It allows for the reliable incorporation of friction and viscoelastic effects for different pipe materials. The 1D MOC transforms the partial differential equations (PDEs) into ordinary differential equations (ODEs) along the two characteristic lines. These characteristics are discretized with time step Δt and spatial step Δx where $\Delta x = a\Delta t$. Figure 2.4 indicates the positive characteristic line C^+ (C_p) extends from point A to P, while the negative characteristic line C^- (C_n) extends from point P to B. The head and discharge at point P are calculated from the known parameters at points A and B, and the mathematical expressions of the lines are (Chaudhry, 2014):

$$\begin{aligned} Q_P &= C_P - C_a H_P \\ Q_P &= C_n + C_a H_P \end{aligned} \tag{2.14}$$

where

$$\begin{aligned} C_p &= Q_A + \frac{gA}{a} H_A - R Q_A \left| Q_A \right| \Delta t \\ C_n &= Q_B - \frac{gA}{a} H_B - R Q_B \left| Q_B \right| \Delta t \end{aligned} \tag{2.15}$$

and

$$C_a = \frac{gA}{a} \tag{2.16}$$

The friction coefficient R is simplified as $R = f / 2DA$ under the steady friction assumption with the Darcy-Weisbach model, and it is commonly applied in MOC. The mathematical expression of R can be replaced or extended with unsteady friction models to capture the additional damping from unsteady friction. For the pipe viscoelasticity, this effect is incorporated with a convolution integral term in the governing equations, and it is implemented with recursive approximation for MOC simulation.

Although the solutions to Eqs. (2.15) and (2.16) can be expressed analytically for a given time step and known values of discrete points; the complete transient solution along the pipeline still requires stepwise computation across the pipeline. The analytical expression and approximation of MOC could ensure the accurate capture of transient behaviour, providing confidence in the validity of the numerical implementation.

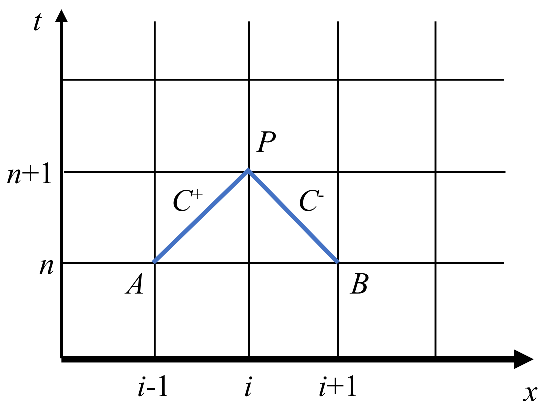

Figure 2.4 Schematic for 1D MOC

Other simulation approaches (FDM, FVM, FEM)

While the MOC remains the most commonly used numerical solution for 1D transient governing equations, other numerical models are applied under specific circumstances. For example, the Finite Difference Method (FDM) is simple and efficient for short and straightforward pipeline systems but challenging to apply for complex boundary conditions (Chaudhry, 2014; Vítkovský et al., 2006; Wylie et al., 1993). The Finite Volume Method (FVM) offers advantages for irregular meshes and complex domains and ensures the conservation law (Duan et al., 2020; Wylie et al., 1993). The Finite Element Method (FEM) performs well in dealing with irregular geometries and complex boundary conditions, but at the expense of higher computational cost (Chaudhry, 2014).

2.3.3.2 Frequency domain solution

The frequency domain simulation of the transient model primarily relies on the transfer matrix method of the frequency response function (FRF) framework. This approach enables the clear identification of the natural frequency and damping characteristics of the system, and provides a systematic means to analyze and extract the frequency response features of pipeline defects. To conduct the transfer matrix analysis, the governing equations are first transformed into the frequency domain by applying the Fourier transform. Under the harmonic wave assumption, the equations are analytically solved. Finally, the upstream and downstream head and discharge of an intact pipe section are expressed in a transfer matrix form (Che et al., 2021; Duan et al., 2011; Duan et al., 2012; Lee et al., 2005a):

$$\begin{pmatrix} \tilde{q} \\ \tilde{h} \end{pmatrix}^{m+1} = \begin{bmatrix} \cos(\mu L) & i\frac{1}{Y}\sin(\mu L) \\ iY\sin(\mu L) & \cos(\mu L) \end{bmatrix} \begin{pmatrix} \tilde{q} \\ \tilde{h} \end{pmatrix}^{m} \tag{2.17}$$

where $\tilde{q}$ and $\tilde{h}$ are the discharge and head perturbation in the frequency domain, subscript m and m+1 are the upstream and downstream of the pipe section, respectively. L is the length of the pipe section. $\mu = \frac{\omega}{a}\sqrt{1 - i\frac{gAR}{\omega}}$ is the propagation function, in which ω is the frequency, $i=\sqrt{-1}$. $Y=-\frac{a}{gA}\sqrt{1-i\frac{gAR}{\omega}}$ is the characteristic impedance. Here, the friction coefficient R can be denoted as $R=\frac{fQ_0}{gDA^2}$. The transfer matrix equation of this single pipe section can be combined with other matrices for both system configuration and defects to form an overall expression for the system's frequency domain description. To account for possible variations in the defects, the equation can be expanded to a 3×3 form (Chaudhry, 2014; Lee et al., 2005a):

$$\begin{Bmatrix} q \\ h \\ 1 \end{Bmatrix}^{D} = \begin{bmatrix} U_{11} & U_{12} & U_{13} \\ U_{21} & U_{22} & U_{23} \\ U_{31} & U_{32} & U_{33} \end{bmatrix} \begin{Bmatrix} q \\ h \\ 1 \end{Bmatrix}^{U} \tag{2.18}$$

in which U_{ij} is the system matrix element, 1 in the column matrix refers to the additional term that's not related to head or discharge (Duan et al., 2020).

The transfer matrix method is widely adopted for frequency domain function-based transient wave analysis. By assembling and multiplying the matrices representing each pipe element, and giving specified boundary conditions, such as upstream head or downstream valve closure, the equation is easily solved, and the frequency response curve can then be obtained. Nevertheless, it is worth noting that since the transfer matrix method is based on linearized assumptions (i.e., small perturbations and linear friction), it can be challenging to handle strongly nonlinear boundary conditions. Researchers have systematically researched the effect of linearization and the corresponding error, and found that with the transient perturbation much smaller than the initial steady state flow rate, the accuracy of

MOC simulation is valid within an acceptable range (Duan, 2018; Lee, 2013). For now, the transfer matrix equation has been widely applied for the transient-based pipe system simulation under more complex conditions like loop systems, branched systems, leaks, and blockages (Che, Wang, & Ghidaoui, 2022; Duan, 2017; Duan et al., 2011; Lee et al., 2005a; Pan et al., 2020; X. Wang & M. Ghidaoui, S, 2018).

2.4 Transient-based Leak Detection Methods

The transient-based methods have been applied in the water supply systems for the detection of various types of defects. Unlike other defects such as blockages or air pockets, leaks are open damages that directly lead to water loss and energy dissipation. The unique characteristic produces significant reflections and attenuation in transient signals, providing a reliable basis for leak identification. This section introduces some common transient signal processing techniques and provides an extensive review of transient-based leak detection methods.

2.4.1 Signal processing techniques

A critical step in transient-based leak detection is signal processing, which allows the extraction of key information from measured pressure signals. Techniques such as wavelet transforms and cross-correlation are commonly employed to highlight leak-induced features in the transient wave. By analyzing the signals in the time domain, frequency domain, or a combination of both, leaks can be accurately detected and localized.

2.4.1.1 Wavelet transform

The wavelet transform is a commonly applied time-frequency analysis method for leak detection. It can capture the short-term transient wave characteristics in both the time and frequency domains. By performing multi-resolution analysis to the signal, the signal is decomposed into different scales, enabling the identification of leak-induced features by separating them from the system-related features in the reflected transient wave, improving the accuracy of transient-based leak detection (Ferrante & Brunone, 2003b; Ferrante et al., 2007, 2009b). The wavelet transform of a signal is (Che et al., 2021)

$$h_{WT}(\tau, s) = \frac{1}{\sqrt{|s|}} \int_{-\infty}^{+\infty} H(t) \Psi\left(\frac{t-\tau}{s}\right) dt \tag{2.19}$$

in which Ψ is the mother wavelet, τ is the translation parameter, and s is the scale parameter.

2.4.1.2 Frequency response function

The Frequency response function describes the input and output relationship of a linear system in the frequency domain. It characterizes how the system responds to different frequency components by providing the ratio of output to input as a function of frequency (Chaudhry, 2014; Che et al., 2021). The FRF is obtained by applying the Fourier transform and identifying the defect-induced system frequency changes in resonant frequencies. The Fourier output of the system is

$$h(\omega) = Y(\omega)U(\omega) \tag{2.20}$$

where $h(\omega)$ is the output, $Y(\omega)$ is the input, and $U(\omega)$ is the Fourier transform. This method is widely applied in transient-based leak detections (Duan et al., 2018; Duan & Keramat, 2022; Keramat et al., 2022; Lee et al., 2005a; Pan et al., 2020; X. Wang & M. Ghidaoui, S, 2018). This method is robust and effective in capturing the impact of defects on the overall system dynamics. However, its performance is limited in strongly nonlinear flow conditions or when viscoelastic effects dominate the transient response (Covas et al., 2005; Ferrante & Brunone, 2003a; Lee et al., 2006).

2.4.1.3 Cross-correlation

The cross-correlation method is a time-domain method used to identify the signal arrival time between two pressure transducers. For the transient reflection-based analysis, it is referred to as the arrival time of the reflected transient wave(Beck et al., 2005). The mathematical expression of the cross-correlation ($C_r(n)$) between the input ($X(t)$) and output ($Y(t)$) signals is

$$C_r(n) = \frac{1}{T}\int_0^T X(t)Y(t+n)\,dt \tag{2.21}$$

In transient-based leak detection, the cross-correlation technique facilitates the extraction of wave time-lag and simplifies leak identification through straightforward implementation and clear visualization (Beck et al., 2005; Motazedi & Beck, 2018). However, the cross-correlation method is sensitive to noise, which can easily obscure the signal.

2.4.1.4 Hilbert-Huang transform

The Hilbert-Huang transform is an efficient time-frequency signal processing algorithm that shows superior performance in analyzing non-linear and non-stationary signals like transient waves (Sun et al., 2016). It contains two steps: first, the empirical decomposition method (EMD) decomposes the input signal into a set of intrinsic mode functions (IMFs); second, the Hilbert transform is applied to convert the IMFs to obtain a time-frequency domain representative for reconstruction and analysis. This method is particularly effective for analyzing transient signals under complex pipe conditions (Ghazali et al., 2012; Lei et al., 2013).

2.4.1.5 Optimization techniques

When estimating leak characteristics from observational data using the established forward model (i.e., inverse problem), researchers often employ optimization or search algorithms to identify parameter sets that minimize the discrepancy between model predictions and measured data (Ghidaoui et al., 2005). It is important to note that optimization is not, strictly speaking, a signal processing technique. Rather, it serves to enhance the efficiency and accuracy of transient-based leak detection. Various optimization techniques have been widely adopted, including but not limited to the Levenberg-Marquardt (LM) algorithm and genetic algorithms (GA). The LM algorithm is a gradient-based optimization with fast convergence speed. Liggett and Chen (1994) first applied the LM algorithm to the inverse transient analysis. GA, on the other hand, is widely applied to global optimization problems, offering a broader search space at the expense of relatively lower speed. Vítkovský, Simpson, et al. (2000) employed GA for leak detection, and Kapelan et al. (2003) combined both algorithms to exploit their advantages. Beyond these, other optimization techniques have also been investigated for transient-based leak detection, such as particle swarm optimization (PSO) (Zhang, Gong, et al., 2018), central force optimization (CFO) (Haghighi & Ramos, 2012), and so on, demonstrating the diversity of optimization methods in this field.

2.4.2 Different transient-based leak detection approaches

Current transient-based leak detection methods can be broadly categorized into two main groups according to the amount of transient signal information utilized (e.g., full or truncated) for leak detection: the local feature-based methods and the full-waveform inversion (FWI) methods. These two methods can be further distinguished by the feature domain in which they operate (i.e., time or frequency domain). The five primary transient-based leak detection methods, namely the frequency response function method, the transient wave reflection method, the transient wave damping method, the matched field processing method, and the inverse transient analysis method, are categorized and summarized in Table 2.1, and their underlying principle, applications, and recent advances are discussed in the following sections.

Table 2.1 Classification of the transient-based leak detection methods

Main type	Sub type	Method
Local feature-based method	Frequency domain	Frequency response function (FRF) based method
	Time domain	Transient wave reflection (TWR) based method Transient wave damping (TWD) based method
Full-waveform inversion method	Frequency domain	Matched field processing (MFP) method
	Time domain	Inverse transient analysis (ITA) method

2.4.2.1 Local feature-based method

Frequency response function (FRF)-based method

The FRF-based leak detection methods are formulated using the transfer matrix approach. As described in the previous section, the detection method relies on the assumption of linearization and determines the unknown head and discharge in the frequency domain by applying the specified boundary conditions and assembling and multiplying the matrices representing each pipe element. The FRF-based method utilizes the resonant frequencies instead of all frequencies for leak distribution. For an intact pipe, the frequency domain transient signal consists of uniformly distributed resonant peaks of similar amplitude. In the presence of a leak, the leak can be represented by a point matrix U_{Leak}:

$$U_{Leak} = \begin{bmatrix} 1 & -\dfrac{Q_{L0}}{2H_{L0}} \\ 0 & 1 \end{bmatrix} \tag{2.22}$$

in which Q_{L0} is the steady-state leak discharge, and H_{L0} is the head at the leak location. The output frequency signal for a leaky pipe shows sinusoidal fluctuations at the peaks, known as the leak-induced pattern (Che et al., 2021). Its analytical expression has been developed and widely applied to leak detection (Duan, 2017; Duan et al., 2011; Duan et al., 2012; Lee et al., 2006), and the form is:

$$\hat{h}(n) = \alpha \cos(2\pi n x_L^* - \theta) + \beta \tag{2.23}$$

where $\hat{h}(n)$ is the inverted head magnitude of the n-th peak, α and β are coefficients,

θ is the phase, and x_L^* is the dimensionless leak location.

The regular changes of the FRF peak pattern caused by leaks were first observed by Lee et al. (2005a) in the RPV system. In that research, a resonant peak-sequencing method is proposed, which laid the foundation of this method. In their subsequent studies, further discussion and validation on how this pattern can be used for leak detection were conducted both numerically and experimentally (Lee et al., 2006; Lee et al., 2005b). Duan et al. advanced this approach through a systematic derivation of the analytical leak-induced pattern, in which leak location and size were explicitly parameterized. Their work also provided extended solutions that can be applied to more complex pipeline configurations, such as branched and looped systems. (Duan, 2017; Duan et al., 2011; Duan et al., 2012). They also investigated the impact of viscoelastic pipe behavior on the FRF-based method and demonstrated that while viscoelasticity affects the amplitude and frequency of resonant peaks, it has only a minor influence on the leak-induced pattern, thereby confirming the effectiveness of the FRF-based approach for leak detection in viscoelastic pipes. (Che et al., 2021; Duan et al., 2012). Moreover, studies by Duan (2017) and Pan et al. (2021) indicated that leak localization is generally easier than size detection. This is primarily due to the effects of steady friction and leak linearization, as well as the neglect of uncertainties such as measurement errors and inaccuracies in inverse analysis. Gong et al. (2014) compared the odd and even harmonics of the leak-induced resonant peaks and confirmed the robustness of odd-harmonic-based leak detection. In a sensitivity analysis of the FRF-based method, Duan et al. (2018) found that the uncertainty of the pipe wave speed, diameter, and data measurement are the primary sources of detection errors, indicating the importance of a good understanding and accurate measurement of the system in FRF-based leak detection.

Transient wave reflection (TWR)-based method

The transient wave reflection-based method is one of the earliest and simplest approaches for exploiting transient signals in the time domain. As illustrated in Figure 2.5, a transient wave is injected into the system by valve operation, and when it encounters a leak, a reflected wave is induced, with its amplitude corresponding to the leak size. The measured signal is then compared with that of an intact pipe, and the leak location relative to the measurement point is estimated from the arrival time and propagation velocity of the reflected wave (i.e., wave speed).

$$x_L^* = \frac{a(t_2 - t_1)}{2L} \tag{2.24}$$

where t_1 and t_2 are the wave transmission times of the leak and the upstream end, respectively.

The leak size can be estimated through calculations involving pressure head and flow rate, typically using the orifice equation.

$$Q_L = C_d A_L \sqrt{2g\Delta H_L} \tag{2.25}$$

in which Q_L is the leak discharge, C_d is the leak size coefficient, A_L is the leak area, and ΔH_L is the pipe internal and external head difference at the leak.

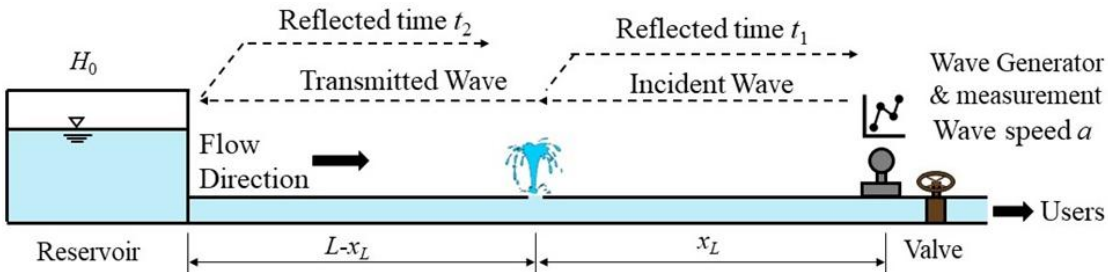

Figure 2.5 Sketch for the transient wave reflection-based method

The TWR-based method was first systematically brought up by Brunone (1999) for leak detection in sewage pipes, who suggested that a leak induces a negative pressure reflection that can be exploited for leak detection, and that the reflection time can be used for leak localization. The method was initially validated in the laboratory using a single viscoelastic pipe. Ferrante and Brunone (2003b) subsequently enhanced the identification of wave arrival times by applying the wavelet transform to detect local singularities in transient signals, an approach also validated in laboratory tests. Building on this, the team conducted a series of studies on the application of wavelet transforms in the TWR-based method (Ferrante et al., 2007, 2009a, 2009b). Different forms of wavelet transforms were compared, and the robustness of the technique against noise was confirmed through numerical and experimental studies (Ferrante et al., 2007). Further experiments were carried out to detect leaks in more complex systems, including branched configurations and field applications. The results demonstrated that, as system complexity increases, additional measurement points are required to ensure the reliability of detection results (Ferrante et al., 2009a). In addition to wavelet analysis, other numerical techniques have been proposed to enhance the TWR-based method. Beck et al. (2005) introduced an enhanced cross-correlation technique for leak detection in pipe networks with T-shaped junctions, while Taghvaei et al. (2006) applied cepstrum analysis for this purpose. Liou (1998) proposed the impulse response function (IRF) for the TWR-based method, characterizing the response of an intact pipeline and identifying the changes in the impulse response caused by leaks. Studies by Lee et al. (2005b) and Nguyen et al. (2018) further extended the IRF application.

The TWR-based method has also been extended to field applications. For example, Meniconi et al. (2015) tested the approach on part of the water supply network of Milan, Italy, employing a Lagrangian model of pressure wave propagation combined with GA and wavelet analysis to assist leak localization.. Shucksmith et al. (2012) reported a field test in the UK where cepstrum analysis was applied to interpret the measured transient signals. Other field studies include those by Covas and Ramos (2010), Gong et al. (2015), Lee et al. (2017), and so on.

The TWR-based method has been studied and applied for many different cases, yet it has its limitations. In viscoelastic pipes and under unsteady-state friction, the reflected signal attenuates, limiting the detection range (Taghvaei et al., 2006); wave reflection aliasing caused by complex networks could reduce the detection accuracy of the method (Beck et al., 2005). These limitations highlight the challenges of directly applying the TWR-based method and have motivated the exploration of other time domain leak detection techniques.

Transient wave damping (TWD)-based method

The transient wave damping-based method is another time-domain local feature-based approach, first introduced for pipeline leak detection by Wang et al. (2002). Derived from the one-dimensional transient model, this method utilizes the damping rate of the transient trace to identify defects. It does not rely on explicit boundary conditions and employs the different pressure signal measured by the leaky and intact pipe. The significant differences in transient damping between the two signals provide the basis for determining the characteristics of leaks. Through analytical analysis, Wang et al. (2002) found the damping ratio of the two harmonic components to be:

$$\frac{R_{n_1 L}}{R_{n_2 L}} = \frac{\sin^2\left(n_1 \pi x_L^*\right)}{\sin^2\left(n_2 \pi x_L^*\right)} \tag{2.26}$$

The leak size is

$$C_d A_L = \frac{R_{nL} A \sqrt{2 g H_{L0}}}{a \sin^2\left(n \pi x_L^*\right)} \tag{2.27}$$

in which R_{nL} is the leak-induced damping rate for the n-th mode, n_i is the mode number, with i = 1 or 2; n is any mode of n_i. The above equations enable direct estimation of leak parameters without the use of optimization techniques. The key assumptions of the TWD-based method include: linearization of the turbulent friction term, relatively small amplitude of transient event, relatively small leak size, and single pipeline configuration (Duan et al., 2020; Nixon et al., 2006). Nixon et al. (2006) discussed and verified these assumptions, further suggesting that the TWD-based method could be applied to more complex systems by isolating the pipes from the network. In reality, the transient damping arises mainly from frictional effects and viscoelasticity, with additional contributions from minor energy losses at junctions. Brunone et al. (2018) applied the TWD-based method for leak detection in HDPE pipes and compared the signal damping between leaky and intact cases.

They suggested that, in polymeric leaky pipes, pressure decay depends exponentially on leak size, leak location, and the pressure at the leak. Furthermore, for a given transient event, identical damping of pressure peaks may occur in different pipe systems. They also proposed a summary and diagnostic framework for the TWD-based method in Capponi et al. (2020).

2.4.2.2 Full-waveform inversion (FWI) method

Compared with local feature-based methods, which selectively use portions of the transient signal, the full-waveform inversion method utilizes the entire measured signal, thereby exploiting more comprehensive information. As a result, FWI methods are generally more robust and provide more accurate detection results (Che et al., 2021). A representative frequency-domain FWI approach is the matched-field processing method, while in the time domain, the inverse transient analysis (ITA) is commonly employed. These two approaches are reviewed in this section.

Matched-field processing (MFP) method

The matched-field processing method is a relatively recent development in frequency-domain analysis, which utilizes the full frequency spectrum of the signal for leak detection rather than relying solely on resonance peaks (X. Wang & M. Ghidaoui, S, 2018). Compared to the traditional FRF-based method, the leak-induced signal in the frequency domain can be expressed as

$$\Delta\tilde{\mathbf{h}} = s^L \tilde{\mathbf{G}}(x^L) + \tilde{\mathbf{n}} \tag{2.28}$$

where the s^L is the leak size, $\mathbf{G}(x^L)$ is the function of leak location, and $\mathbf{n}$ is the

Gaussian white noise, the tilde represents the frequency domain. Based on this factorized model, the frequency domain leak location and size are decoupled and can be estimated separately. The leak location is estimated by

$$\hat{x}^L = \arg\min_{x^L} \frac{\Delta\tilde{\mathbf{h}}^H \tilde{\mathbf{G}}(x^L)\tilde{\mathbf{G}}^H(x^L)\Delta\tilde{\mathbf{h}}}{\tilde{\mathbf{G}}^H(x^L)\tilde{\mathbf{G}}(x^L)} \tag{2.29}$$

where $\hat{x}^L$ is the optimal leak location. Consequently, the leak size is calculated by solving the maximum likelihood of Eq. (2.26).

The matched-field processing (MFP) method has demonstrated high accuracy and robustness as a full-waveform inversion (FWI) approach when applied under various noise levels. Its applicability was first tested in a single-pipe system, where it proved effective in handling noise (X. Wang & M. Ghidaoui, S, 2018). The method was subsequently extended to multiple leaks through the iterative beamforming approach, and validated with both numerical and experimental cases, where its capability for super-resolution of multiple leak locations was also confirmed (X. Wang & M. S. Ghidaoui, 2018; Wang & Ghidaoui, 2019; Wang, Ghidaoui, et al., 2019). Further developments included uncertainty analysis, in which prior information on modeling errors was incorporated to improve robustness (Wang, 2021; Wang, Lin, et al., 2019; Wang et al., 2020; Waqar et al., 2021). The method has also been extended to more complex pipe systems, including branched and looped configurations, as well as to different pipe materials such as viscoelastic pipes, with validation through both numerical and experimental studies (Che, Wang, & Ghidaoui, 2022; Che, Wang, Louati, et al., 2022; Che, Wang, Zhou, et al., 2022; Wang et al., 2021; Wang & Ghidaoui, 2021; Wang, Lin, et al., 2019).

The MFP method is an important development of the transient-based lead detection in the frequency domain. By decoupling leak parameters, MFP can simplify a multi-dimensional inverse problem into several sequential one-dimensional optimizations, thereby improving detection efficiency while maintaining robustness and accuracy. Nevertheless, the application of frequency-domain methods in practice faces challenges. To ensure a convergent frequency-domain representation, a sufficiently long and damped time-domain signal is usually required. Such stringent requirements are often difficult to satisfy in real-world scenarios, where severe wave damping and dispersion occur, particularly in large-scale and complex pipeline networks. As a result, the flexibility in utilizing measured signals becomes limited, restricting the applicability of the method in practice.

Inverse transient analysis (ITA) method

The Inverse transient analysis method is a classic time-domain full-waveform inversion method, first proposed by Liggett and Chen (1994). In the ITA, a transient model is employed to simulate system responses across all potential leak locations and within bounded leak sizes. The modeled signals are then compared with measured transients, and the discrepancy is minimized through nonlinear optimization (Kapelan et al., 2004). The initial ITA objective function is

$$\left[\hat{\mathbf{s}}_{\mathbf{A}}, \hat{\mathbf{x}}_{\mathbf{A}}, \hat{\mathbf{f}}\right] = \underset{\mathbf{s}_{\mathbf{A}}, \mathbf{x}_{\mathbf{A}}, \mathbf{f}}{argmin} \left\{ \sum_{i=1}^{M} \sum_{j=1}^{N} \left[H_{ij}^{m} - H_{ij}^{n}\left(\mathbf{s}_{\mathbf{A}}, \mathbf{x}_{\mathbf{A}}, \mathbf{f}\right) \right]^{2} \right\} \tag{2.30}$$

in which $\mathbf{s_A}$, $\mathbf{x_A}$ are the leak size and location vector, $\mathbf{f}$ is the unknown parameter vector, and the hat is the optimal solution. However, the ITA method can easily be trapped in local optima, and as system complexity increases, the coupled optimization of leak parameters requires numerous model evaluations, leading to high computational cost. To address this issue, researchers have studied improving ITA detection efficiency through enhanced optimization techniques and other methods.

The ITA was initially formulated using the LM algorithm for optimization (Liggett & Chen, 1994). As discussed in the previous section, this approach is easily trapped in local optima. To address this limitation, Vítkovský, Simpson, et al. (2000) applied GA to ITA, thereby improving its capability for global optimization, and later successfully applied the method in lab experimental tests for single and multiple leaks detection (Vítkovský et al., 2007). Kapelan et al. (2003, 2004) combined LM and GA, introducing prior information to reduce computational complexity while enhancing the reliability of detection results. Other optimizations, such as central force optimization (CFO) and sequential quadratic programming (SQP), have also been integrated with ITA to improve its global optimization performance for defect detection (Haghighi & Ramos, 2012; Shamloo & Haghighi, 2010).

Other than the improvement of optimization, different schemes were also introduced for numerical modeling. Kim (2016) proposed the impedance-based ITA for leak detection and demonstrated its applicability to pipe networks with diverse boundary conditions. The researcher further extended this study to address blockage and multiple leak detection (Kim, 2018, 2020). Recently, S. Kim (2022) combined it with PSO to improve robustness and then introduced a dimensionless impedance-based ITA, improving the efficiency and applicability of the method (S. H. Kim, 2022). Zhang, Gong, et al. (2018) proposed a pressure head-based MOC and ITA with a flexible computational grid, which accelerated the computational speed. The team also proposed a multi-stage parameter-constraining search framework for ITA, enhancing its reliability and robustness (Zhang, Zecchin, et al., 2018).

Experimental studies have also been conducted on ITA-based leak detection. In addition to the work of Vítkovský et al. (2007), which verified the applicability of ITA, Covas and Ramos (2010) and Soares et al. (2011) also applied the method. More recently, Capponi et al. (2017) combined ITA with the admittance matrix method and applied it to leak detection in branched systems. Despite the advancements made in this area, the application of ITA still involves extensive data invocation. Leading to significant computational demands, extending computational processing time, and impeding detection efficiency. Therefore, it is necessary to address the low efficiency issue of the time-domain full-waveform inversion method.

All five leak detection methods reviewed above are based on the physical interpretation of wave propagation in pipelines, where leaks introduce local discontinuities that generate additional reflections, increased damping, and waveform distortion. These methods mainly differ in how the leak-induced signals are treated, including direct or indirect reflection analysis, parameter estimation, and attenuation-based characteristics. The robustness of these approaches is generally constrained by modeling accuracy and prior knowledge of the system, both of which may be affected by practical uncertainties. These limitations have motivated the development of data-driven methods, which aim to identify leaks directly from measured data.

2.4.2.3 Data-driven methods

In addition to conventional transient-based leak detection methods, the integration of machine learning/artificial intelligence (AI) with transient signals has gained increasing attention in recent years. With the growing popularity of AI techniques and their increasing ease of implementation, the adoption of data-driven approaches for handling transient wave data has become more feasible and inevitable. These methods represent an emerging direction in transient-based leak detection.

For example, the study of Bohorquez et al. (2020) pointed out that artificial neural networks (ANNs) can efficiently learn the relationship between pipeline features and transient waves and achieve highly accurate leak detection without relying on detailed physical models. Asghari et al. (2023) introduced the CatBoost framework and ensembles trained on millions of transient records, achieving 97% accuracy. Ye et al. (2024) embedded the elastic water column model into a physics-informed neural network (PINN), enabling accurate reconstruction of transient states under sparse and noisy measurements, ensuring the robustness of the transient-based method. As indicated in Gong et al. (2024), despite the significant progress achieved, the challenges of complex uncertainties and small-defect detection in large-scale, real-world water supply networks remain unresolved. Addressing these challenges represents a key direction for future research and development in data-driven transient-based leak detection.

CHAPTER 3 TIME-DOMAIN FACTORIZED WAVE ANALYSIS METHOD

3.1Introduction

In this chapter, a factorized transient wave model for pressurized pipeline systems with both single and multiple leaks is analytically developed. Building upon this model, a transient-based time-domain leak detection method is proposed, which involves parameter separation for single leaks and a combination of iterative beamforming with parameter separation for multiple leaks.

3.2 Single Leak Detection

3.2.1 The factorized wave model for a single leak

The frictionless water hammer model with a leak is (Chaudhry, 2014)

$$\frac{1}{a^2}\frac{\partial H}{\partial t}+\frac{1}{gA}\frac{\partial Q}{\partial x}=-sign(Q)\frac{1}{gA}\gamma^L\sqrt{H}\;\delta(x-x^L) \tag{3.1}$$

$$\frac{1}{gA}\frac{\partial Q}{\partial t}+\frac{\partial H}{\partial x}=0 \tag{3.2}$$

where $\gamma^L = C_d A_L(2g)^{0.5}$ = leak size coefficient; $\delta(\cdot)$ = Dirac delta function; and sign($\cdot$) = sign function.

Note that friction is omitted in the methodology section to simplify the derivation of the factorized wave model, as its impact on leak localization is negligible (Waqar et al., 2023). However, friction is kept in the model for numerical and laboratory experiments involving leak size estimation in the following sections.

As mentioned in the last chapter, in transient waves, the variables H and Q can be expressed as

$$H = H_0 + h \tag{3.3}$$

$$Q = Q_0 + q \tag{3.4}$$

where H_0 = mean pressure head; h = pressure head perturbation; Q_0 = mean discharge; and q = discharge perturbation.

Note that the mean quantities of discharge and pressure head are time independent; thus, the terms related to $\partial Q_0/\partial t$ and $\partial H_0/\partial t$ are all zero. Therefore,

$$\frac{\partial Q}{\partial t} = \frac{\partial q}{\partial t} \tag{3.5}$$

$$\frac{\partial Q}{\partial x} = \frac{\partial Q_0}{\partial x} + \frac{\partial q}{\partial x}, \frac{\partial Q_0}{\partial x} = -sign(Q_0)\gamma^L \sqrt{H_0}\ \delta(x - x^L) \tag{3.6}$$

$$\frac{\partial H}{\partial t} = \frac{\partial h}{\partial t} \tag{3.7}$$

$$\frac{\partial H}{\partial x} = \frac{\partial H_0}{\partial x} + \frac{\partial h}{\partial x}, \frac{\partial H_0}{\partial x} = 0 \tag{3.8}$$

Substituting Eqs. (3.3) through (3.8) into Eqs. (3.1) and (3.2) gives

$$\begin{aligned} &\frac{1}{a^2}\frac{\partial h}{\partial t} + \frac{1}{gA}\frac{\partial q}{\partial x} - sign(Q_0)\frac{1}{gA}\gamma^L\sqrt{H_0}\delta(x - x^L) \\ &= -sign(Q_0 + q)\frac{1}{gA}\gamma^L\sqrt{H_0 + h}\delta(x - x^L) \end{aligned} \tag{3.9}$$

$$\frac{1}{gA}\frac{\partial q}{\partial t}+\frac{\partial h}{\partial x}=0 \tag{3.10}$$

Assumption 1: the perturbation is small; thus, $|q| << |Q_0|$, $|h| << |H_0|$, and $\mathrm{sign}(Q) = \mathrm{sign}(Q_0)$.

$$\sqrt{H_0+h}\approx\sqrt{H_0}\left(1+\frac{1}{2}\frac{h}{H_0}\right) \tag{3.11}$$

Substituting Eq. (3.11) into Eq. (3.9) gives

$$\frac{1}{a^2}\frac{\partial h}{\partial t}+\frac{1}{gA}\frac{\partial q}{\partial x}=-\frac{\gamma^L\sqrt{H_0}}{2gA}\frac{h}{H_0}\delta(x-x^L) \tag{3.12}$$

$$\frac{1}{gA}\frac{\partial q}{\partial t}+\frac{\partial h}{\partial x}=0 \tag{3.13}$$

Applying Fourier transform to Eqs. (12) and (13) gives

$$\frac{i\omega\tilde{h}}{a^2}+\frac{1}{gA}\frac{\partial\tilde{q}}{\partial x}=-\frac{\gamma^L\sqrt{H_0}}{2gA}\frac{\tilde{h}}{H_0}\delta(x-x^L) \tag{3.14}$$

$$i\omega\frac{1}{gA}\tilde{q}+\frac{\partial\tilde{h}}{\partial x}=0 \tag{3.15}$$

where $\tilde{h}$ and $\tilde{q}$ = pressure head perturbation and discharge perturbation in the frequency domain.

Eq. (3.15) gives $\tilde{q}=-\frac{gA}{i\omega}\frac{\partial\tilde{h}}{\partial x}$ and substitutes into Eq. (3.14),

$$\underbrace{\left(\frac{\partial^2}{\partial x^2}+k^2\right)}_{\mathcal{L}}\tilde{h}=\underbrace{i\omega\frac{\gamma^L\sqrt{H_0}}{2gA}\frac{\tilde{h}}{H_0}\delta(x-x^L)}_{\mathcal{F}} \tag{3.16}$$

where $k=\omega/a$ is the wave number.

Eq. (3.16) can be written in the following compact form

$$\mathcal{L}\tilde{h}=\mathcal{F} \tag{3.17}$$

where $\mathcal{L}$ is the differential operator, and $\mathcal{F}$ is the external forcing due to the leak. The scatter-free $\tilde{h}_{NL}(\omega, x)$ can be obtained by solving the homogeneous equation (i.e., $\mathcal{F}=0$)

$$\mathcal{L}\tilde{h}_{NL}(\omega,x)=0 \tag{3.18}$$

The Green's function $\tilde{G}(\omega,x\,|\,x^S)$ can be obtained by solving

$$\mathcal{L}\tilde{G}(\omega,x\,|\,x^S)=\delta(x-x^S) \tag{3.19}$$

where x^S is the wave source location.

Therefore, the solution for Eq. (3.17) can be written as (Zettili, 2009)

$$\begin{aligned}\tilde{h}(\omega,x)&=\tilde{h}_{NL}(\omega,x)+\int_0^L\tilde{G}(\omega,x\,|\,x^S)\mathcal{F}(x^S)dx^S\\&=\tilde{h}_{NL}(\omega,x)+\frac{\gamma^L\sqrt{H_0^L}}{2H_0^L}\frac{i\omega}{gA}\tilde{G}(\omega,x\,|\,x^L)\tilde{h}(x^L)\end{aligned} \tag{3.20}$$

where H_0^L means the pressure head at the leak; and $\tilde{h}(x^L)$ is the transient pressure at the leak. The specific form of the Green's function $\tilde{G}(\omega, x \mid x^S)$, which depends on the boundary conditions, is not explicitly provided here. More details are reported by (Zettili, 2009).

Assumption 2: in a bounded pipe system, leaks usually interact strongly with incident waves at resonant frequencies. However, within bandwidth without resonant frequencies, the transient pressure at the small leak can be approximated as $\tilde{h}(x^L) \approx \tilde{h}_{NL}(x^L)$, which is known as the first Born approximation in scattering theory (Born, 1926; Zettili, 2009).

Therefore, Eq. (3.20) becomes

$$\tilde{h}(\omega, x) \approx \underbrace{\tilde{h}_{NL}(\omega, x)}_{\substack{\text{leak}\\ \text{independent}}} + \underbrace{\frac{\gamma^L \sqrt{H_0^L}}{2H_0^L}}_{\substack{\text{leak}\\ \text{size term}}} \underbrace{\frac{i\omega}{gA} \tilde{G}(\omega, x \mid x^L) \tilde{h}_{NL}(x^L)}_{\text{leak location term}} \tag{3.21}$$

Eq. (3.21) can be written in the following compact form

$$\tilde{h}(\omega, x) = \tilde{h}_{NL}(\omega, x) + \tilde{s}^L \mathcal{G}(x^L) \tag{3.22}$$

where $\tilde{s}^L = \dfrac{\gamma^L \sqrt{H_0^L}}{2H_0^L} = \dfrac{Q_0^L}{2H_0^L}$, in which Q_0^L is the steady state discharge of the leak; and $\mathcal{G}(x^L) = \dfrac{i\omega}{gA} \bar{\tilde{G}}(\omega, x \mid x^L) \tilde{h}_{NL}(x^L)$.

This indicates that the pressure response at any location can be factorized into a leak-independent term and a leak-dependent term, where the leak size and location are separated (i.e., leak size term times leak location term). The inverse Fourier transform of Eq.(3.22) gives

$$h(t,x) = h_{NL}(t,x) + s^L \mathcal{G}(x^L) \tag{3.23}$$

Eq. (3.23) illustrates the separability of the two unknown leak parameters within the time-domain wave model. Based on this theoretical foundation, an efficient two-stage algorithm is proposed in this study to enhance the efficiency of leak detection. However, the function $\mathcal{G}(\cdot)$ is numerically computed using the classical wave model, instead of applying the inverse Fourier transform to Eq. (3.22) for leak localization.

3.2.2 Single leak detection algorithm

Let h^{obs} represent the measured transient signal from the pipe system that contains system noise n following Gaussian distribution $\mathcal{N}(0,\sigma^2 I_J)$ to simulate the multi-sources environmental noise that occurs during real pipe operation (Lin et al., 2021). Similarly, let $h^{model}(x^L, s^L)$ represent the corresponding theoretical transient signal simulated by the model. Let J denote the number of data collection points. With given system parameters and sampling time, mathematically, the measured transient signal can be expressed in vector form:

$$\mathbf{h}^{obs}(x^L, s^L) = \mathbf{h}^{model}(x^L, s^L) + \mathbf{n} \tag{3.24}$$

where the collected sensor data are shown by $\mathbf{h}^{obs} = (h_1^{obs}, h_2^{obs}, ..., h_J^{obs})^T$ and the simulated data are generated by the water hammer model and exhibited as $\mathbf{h}^{model} = (h_1^{model}, h_2^{model}, ..., h_J^{model})^T$. The noise is treated as a Gaussian random function that independently contaminates all data points, i.e., $\mathbf{n} = (n_1, n_2, ..., n_J)^T$.

The two-dimensional optimization for single leak estimation can be written as

$$\left\{\hat{x}^L, \hat{s}^L\right\} = \arg\min_{x^L, s^L} \left\|\mathbf{h}^{obs} - \mathbf{h}^{model}(x^L, s^L)\right\|_2^2 \tag{3.25}$$

in which x^L and s^L represent the potential leak location and size, and $\hat{x}^L$ and $\hat{s}^L$ represent their estimated values. By substituting Eq. (3.23) with Eq. (3.25) for $\mathbf{h}^{model}$, the original two-dimensional optimization turns into

$$\begin{aligned}\left\{x^L, s^L\right\} &= \arg\min_{x^L, s^L} \left\|\mathbf{h}^{obs} - \mathbf{h}^{NL} - s^L \boldsymbol{\mathcal{G}}(x^L)\right\|_2^2 \\ &= \arg\min_{x^L, s^L} \left\|\Delta\mathbf{h} - s^L \boldsymbol{\mathcal{G}}(x^L)\right\|_2^2\end{aligned} \tag{3.26}$$

in which $\Delta\mathbf{h} = (\Delta h_1, \Delta h_2, ..., \Delta h_J)^T$ is the leak-induced pressure difference containing noise $\mathbf{n}$. To localize the leak, a library of $\boldsymbol{\mathcal{G}}(x^L) = \Delta\bar{\mathbf{h}} / s^L$ is numerically constructed for each potential leak location x^L using the classical wave model, and $\Delta\bar{\mathbf{h}}$ is the leak-induced pressure difference without noise interference.

The maximum likelihood estimation for leak size s^L is the least square solution of Eq. (3.26), given by:

$$\hat{s}^L = \frac{\mathcal{G}(x^L)^T \Delta\mathbf{h}}{\mathcal{G}(x^L)^T \mathcal{G}(x^L)} \tag{3.27}$$

Substituting Eq. (3.27) back to Eq. (3.26), the final expression of the objective function in terms of leak location is given as

$$\left\{\hat{x}^L\right\} = \arg\max_{x^L}\left(\Delta\mathbf{h}^T \mathcal{G}(x^L)\frac{\mathcal{G}(x^L)^T \Delta\mathbf{h}}{\mathcal{G}(x^L)^T \mathcal{G}(x^L)}\right) = \arg\max_{x^L}(B^2) \tag{3.28}$$

where B is the objective function in terms of the leak location. Detailed procedures for deriving the estimation of leak size and location in Eq. (3.27) and Eq. (3.28) are provided in Appendix A.

Based on the aforementioned method, we propose the leak detection procedure outlined as follows:

Step 1: Collect the measured transient wave signal $\mathbf{h}^{\text{obs}}$;

Step 2: Compute the modeled transient signal and intact pipe signal ($\mathbf{h}^{\text{model}}$ & $\mathbf{h}^{\text{NL}}$) by nominating the computational Method of Characteristics (MOC) discrete points as the leak; then Compute the modeled leak traces relative to the intact case with $\Delta\mathbf{h}=\mathbf{h}^{\text{model}} - \mathbf{h}^{\text{NL}}$;

Step 3: Compute $\mathcal{G}(x^L)$, plot B^2 in Eq. (3.28) against x^L to find the global maximum that corresponds to leak location estimate $\hat{x}^L$;

Step 4: Solve Eq. (3.27) with $x^L = \hat{x}^L$ to estimate the leak size $\hat{s}^L$;

Step 5: Output (return $\hat{x}^L$ and $\hat{s}^L$).

This method effectively detects single leaks in pipe networks of any complexity by utilizing time-domain transient signals. It employs a time domain transient model and conducts corresponding optimizations within the time domain. This method simplifies the two-dimensional optimization of the leak location and size estimation into a one-dimensional estimation problem that is simply achieved via searching the domain of potential leak location. In comparison to the full enumeration of the leak location and size domain, the proposed approach significantly reduces the number of transient model invocations and enhances the computational efficiency. Furthermore, it allows for visual observation of the leak location and a formalized calculation of leak size, avoiding the issue of being trapped in local extrema by searching size and location parameters simultaneously in the domain.

3.3Multiple Leaks Detection

Following the detection algorithm for a single leak in the pipeline system, efficient and accurate localization of multiple leaks using the time-domain FWI method remains a challenging issue due to two critical problems:

1. The $2N$ leak parameters are coupled and interdependent in the classical wave model, resulting in a high-dimensional ($2N$) non-convex optimization problem.

2. Equation 3.25 requires 10^{2N}-100^{2N} simulations of the classical wave model, which become computationally prohibitive for large N. Moreover, its non-convexity

makes solutions highly sensitive to initial values and easily trapped in local optima.

To resolve the two problems, a factorized wave model is analytically derived, where the original 2*N* coupled leak parameters are separated (resolving Problem 1). Based on the factorized model, the complex 2*N*-dimensional optimization problem is decomposed into 2*N* sequential one-dimensional sub-problems by an iterative beamforming algorithm (resolving Problem 2).

3.3.1 Derivation of factorized wave model

Similar to the single leak derivation procedure, the frictionless transient wave model with two leaks is

$$\frac{1}{a^2}\frac{\partial H}{\partial t}+\frac{1}{gA}\frac{\partial Q}{\partial x}=-sign(Q)\frac{1}{gA}\gamma^{L_1}\sqrt{H}\;\delta(x-x^{L_1})-sign(Q)\frac{1}{gA}\gamma^{L_2}\sqrt{H}\;\delta(x-x^{L_2}) \quad (3.29)$$

$$\frac{1}{gA}\frac{\partial Q}{\partial t}+\frac{\partial H}{\partial x}=0 \quad (3.30)$$

in which $\gamma^{L_n}=C_d^n A_L^n\sqrt{2g}$ is the size coefficient of the *n*-th leak, where C_d^n and A_L^n are the discharge coefficient and opening area of the *n*-th leak, respectively; and x^{L_n} is the location of the *n*-th leak.

Since the mean quantities of discharge Q_0 and pressure head H_0 are time-independent, following the derivation flow of Eqs. (3.3) through (3.8), where $\frac{\partial Q_0}{\partial x}=-\mathrm{sign}(Q_0)\gamma^{L_1}\sqrt{H_0}\delta(x-x^{L_1})-\mathrm{sign}(Q_0)\gamma^{L_2}\sqrt{H_0}\delta(x-x^{L_2})$, and substituting the equations into Eqs. (3.28) and (3.29),

$$\begin{aligned}&\frac{1}{a^2}\frac{\partial h}{\partial t}+\frac{1}{gA}\frac{\partial q}{\partial x}-sign(Q_0)\frac{\gamma^{L_1}}{gA}\sqrt{H_0}\delta(x-x^{L_1})-sign(Q_0)\frac{\gamma^{L_2}}{gA}\sqrt{H_0}\delta(x-x^{L_2})\\&=-sign(Q_0+q)\frac{\gamma^{L_1}}{gA}\sqrt{H_0+h}\delta(x-x^{L_1})-sign(Q_0+q)\frac{\gamma^{L_2}}{gA}\sqrt{H_0+h}\delta(x-x^{L_2})\end{aligned} \tag{3.31}$$

$$\frac{1}{gA}\frac{\partial q}{\partial t}+\frac{\partial h}{\partial x}=0 \tag{3.32}$$

Following Assumption 1, substituting Eq. (3.11) into Eq. (3.30) and applying the Fourier transform, gives

$$\frac{i\omega\tilde{h}}{a^2}+\frac{1}{gA}\frac{\partial\tilde{q}}{\partial x}=-\frac{\gamma^{L_1}\sqrt{H_0}}{2gA}\frac{\tilde{h}}{H_0}\delta(x-x^{L_1})--\frac{\gamma^{L_2}\sqrt{H_0}}{2gA}\frac{\tilde{h}}{H_0}\delta(x-x^{L_2}) \tag{3.33}$$

$$i\omega\frac{1}{gA}\tilde{q}+\frac{\partial\tilde{h}}{\partial x}=0 \tag{3.34}$$

Substituting $\tilde{q}=-\frac{gA}{i\omega}\frac{\partial\tilde{h}}{\partial x}$ from Eq. (3.33) back to Eq. (3.32),

$$\underbrace{\left(\frac{\partial^2}{\partial x^2}+k^2\right)}_{\mathcal{L}}\tilde{h}=\underbrace{i\omega\frac{\gamma^{L_1}\sqrt{H_0}}{2gA}\frac{\tilde{h}}{H_0}\delta(x-x^{L_1})}_{\mathcal{F}_1}+\underbrace{i\omega\frac{\gamma^{L_2}\sqrt{H_0}}{2gA}\frac{\tilde{h}}{H_0}\delta(x-x^{L_2})}_{\mathcal{F}_2} \tag{3.35}$$

Eq. (3.34) can be written in the compact form as

$$\mathcal{L}\tilde{h}=\mathcal{F}_1+\mathcal{F}_2 \tag{3.36}$$

where $\mathcal{F}_n$ is the external forcing due to the n-th leak.

Likewise, the scatter-free $\tilde{h}_{NL}(\omega,x)$ can be obtained by solving the homogeneous equation in which $\mathcal{F}_1 = \mathcal{F}_2 = 0$, leading to $\mathcal{L}\tilde{h}_{NL}(\omega,x)=0$ as in Eq. (3.18). The Green's function can also be obtained with Eq. (3.19). Therefore, the solution for Eq. (3.35) can be expressed as (Zettili, 2009)

$$\begin{aligned}\tilde{h}(\omega,x) &= \tilde{h}_{NL}(\omega,x)+\int_0^L \tilde{G}(\omega,x\,|\,x^S)\left[\mathcal{F}_1(x^S)+\mathcal{F}_2(x^S)\right]dx^S \\ &= \tilde{h}_{NL}(\omega,x)+\frac{\gamma^L\sqrt{H_0^L}}{2H_0^L}\frac{i\omega}{gA}\tilde{G}(\omega,x\,|\,x^{L_1})\tilde{h}(x^{L_1})+\frac{\gamma^L\sqrt{H_0^L}}{2H_0^L}\frac{i\omega}{gA}\tilde{G}(\omega,x\,|\,x^{L_2})\tilde{h}(x^{L_2})\end{aligned} \tag{3.37}$$

where $H_0^{L_n}$ is the mean pressure head at the n-th leak, and $\tilde{h}(x^{L_n})$ is the transient pressure at the n-th leak.

With the description of Assumption 2, similar to single leak, the transient pressure at the n-th small leak can be approximated as $\tilde{h}(x^{L_n})\approx\tilde{h}_{NL}(x^{L_n})$ (Born, 1926), Eq. (3.36) becomes

$$\begin{aligned}\tilde{h}(\omega,x) &\approx \underbrace{\tilde{h}_{NL}(\omega,x)}_{\substack{\text{leak}\\\text{independent}}}+\underbrace{\frac{\gamma^{L_1}\sqrt{H_0^{L_1}}}{2H_0^{L_1}}}_{\substack{1^{\text{st}}\ \text{leak}\\\text{size term}}}\underbrace{\frac{i\omega}{gA}\tilde{G}(\omega,x\,|\,x^{L_1})\tilde{h}_{NL}(x^{L_1})}_{1^{\text{st}}\ \text{leak location term}} \\ &\quad+\underbrace{\frac{\gamma^{L_2}\sqrt{H_0^{L_2}}}{2H_0^{L_2}}}_{\substack{2^{\text{nd}}\ \text{leak}\\\text{size term}}}\underbrace{\frac{i\omega}{gA}\tilde{G}(\omega,x\,|\,x^{L_2})\tilde{h}_{NL}(x^{L_2})}_{2^{\text{nd}}\ \text{leak location term}}\end{aligned} \tag{3.38}$$

Note that $\tilde{h}(x^{L_n})\approx\tilde{h}_{NL}(x^{L_n})$ of Assumption 2 implicitly ignores the interaction between two small leaks; thus, Eq. (3.37) does not have high-order scattering terms.

Eq. (3.37) can be written in the compact form

$$\tilde{h}(\omega, x) = \tilde{h}_{NL}(\omega, x) + \tilde{s}^{L_1}\mathcal{G}(x^{L_1}) + \tilde{s}^{L_2}\mathcal{G}(x^{L_2}) \tag{3.39}$$

where $\tilde{s}^{L_n} = \dfrac{\gamma^{L_n}\sqrt{H_0^{L_n}}}{2H_0^{L_n}} = \dfrac{Q_0^{L_n}}{2H_0^{L_n}}$, in which $Q_0^{L_n}$ is the steady state discharge of the n-th leak; and $\mathcal{G}(x^{L_n}) = \dfrac{i\omega}{gA}\tilde{G}(\omega, x \mid x^{L_n})\tilde{h}_{NL}(x^{L_n})$.

Eq. (3.38) can be easily extended to multiple leaks

$$\tilde{h}(\omega, x) = \tilde{h}_{NL}(\omega, x) + \sum_{n=1}^{N}\tilde{s}^{L_n}\mathcal{G}(x^{L_n}) \tag{3.40}$$

where N is the total number of multiple leaks.

The inverse Fourier transform of Eq. (3.39) gives

$$h(t, x) = h_{NL}(t, x) + \sum_{n=1}^{N} s^{L_n}\mathcal{G}(x^{L_n}) \tag{3.41}$$

Eq. (3.40) proves the separability of the $2N$ unknown leak parameters within the time-domain wave model.

For a pipeline system with multiple leaks, the observed transient signal can be expressed as

$$\begin{aligned} \mathbf{h}^{obs}(x^L, s^L) &= \mathbf{h}^{model}(\mathbf{x}^L, \mathbf{s}^L) + \mathbf{n} \\ &= \mathbf{h}^{NL} + \sum_{n=1}^{N} s^{L_n}\boldsymbol{\mathcal{G}}(x^{L_n}) + \mathbf{n} \end{aligned} \tag{3.42}$$

where $\mathbf{x}^L = (x^{L_1}, x^{L_2}, ..., x^{L_n})^T$ and $\mathbf{s}^L = (s^{L_1}, s^{L_2}, ..., s^{L_n})^T$ are the leak locations and sizes, respectively.

Eq. (3.42) can be further written as

$$\Delta\mathbf{h} = \sum_{n=1}^{N} s^{L_n} \mathcal{G}(x^{L_n}) + \mathbf{n} = \sum_{n=1}^{N} \Delta\bar{\mathbf{h}}^{L_n} + \mathbf{n} \tag{3.43}$$

where $\Delta\mathbf{h} = \mathbf{h}^{obs} - \mathbf{h}^{NL}$ is the total pressure difference induced by N leaks; and $\Delta\bar{\mathbf{h}}^{L_n} = s^{L_n}\mathcal{G}(x^{L_n})$ is the pressure difference induced by the n-th leak, in which the overhead bar means a clean signal without noise. $\mathcal{G}(x^L) = \Delta\bar{\mathbf{h}} / s^L$ is still applied here for each potential leak location under the assumption that there is only one leak in the pipe.

Eq. (3.43) indicates that the total pressure difference $\Delta\mathbf{h}$ induced by N leaks is a linear superposition of pressure differences induced by N individual leaks. Furthermore, the size s^{L_n} and location x^{L_n} of each leak are also decoupled from the product $s^{L_n}\mathcal{G}(x^{L_n})$. Therefore, the original $2N$ coupled leak parameters are separated in Eq. (3.43), which means the aforementioned Problem 1 is successfully resolved.

3.3.2 Iterative Beamforming for Decomposing Composite Wave Signals and Localizing Multiple Leaks

To resolve the aforesaid Problem 2, based on the factorized model derived in Section 3.2.1, this section proposes an iterative beamforming algorithm that decomposes the complex 2N-dimensional optimization problem into 2N sequential one-dimensional sub-problems.

3.3.2.1 Latent Composite Wave Signal Decomposition

This sub-section shows that the decomposition of a composite wave signal into latent components, each corresponding to a distinct leak, enables independent localization of each leak.

The composite wave signal $\Delta\mathbf{h}$ in Eq. (3.43) arises from the superposition of N individual leak contributions. Theoretically, it can be expressed as

$$\Delta\mathbf{h} = \sum_{n=1}^{N} \Delta\mathbf{h}^{L_n} = \sum_{n=1}^{N} \left[s^{L_n} \mathcal{G}(x^{L_n}) + \mathbf{n}_n \right] \tag{3.44}$$

where $\Delta\mathbf{h}^{L_n} = s^{L_n} \mathcal{G}(x^{L_n}) + \mathbf{n}_n$ underlies unobserved signal contribution from the n-th leak, in which the noise component $\mathbf{n}_n$ is obtained by arbitrarily decomposing the measurement noise $\mathbf{n}$ into N components, such that $\mathbf{n} = \sum_{n=1}^{N} \mathbf{n}_n$. Note that $\mathbf{n}_n$ also follows a zero-mean Gaussian distribution $\mathcal{N}(\mathbf{0}, \frac{1}{N}\sigma^2\mathbf{I})$ (Wang & Ghidaoui, 2019).

The vector of the latent decomposed wave signals $\Delta\mathbf{h}^{L} = (\Delta\mathbf{h}^{L_1}, ..., \Delta\mathbf{h}^{L_N})^T$ follows a Gaussian distribution; thus, its log-likelihood function can be written as

$$\ell(\mathbf{x}^L, \mathbf{s}^L \mid \Delta\mathbf{h}^L) = -\sum_{n=1}^{N} \left\| \Delta\mathbf{h}^{L_n} - s^{L_n} \boldsymbol{\mathcal{G}}(x^{L_n}) \right\|_2^2 \tag{3.45}$$

where $\ell(\cdot)$ is the log-likelihood function.

Each term within the summation symbol of Eq. (3.45) represents the contribution from the n-th leak to the log-likelihood function, which is independent of other $N-1$ leaks. Therefore, once the composite wave signal $\Delta\mathbf{h}$ is decomposed into N individual components $\Delta\mathbf{h}^{Ln}$, each corresponding to a distinct leak, multiple leaks can be localized one by one as

$$\{\hat{x}^{L_n}, \hat{s}^{L_n}\} = \underset{x^{L_n}, s^{L_n}}{\arg\min} \left\| \Delta\mathbf{h}^{L_n} - s^{L_n} \boldsymbol{\mathcal{G}}(x^{L_n}) \right\|_2^2 \tag{3.46}$$

where $\hat{x}^{L_n}$ and $\hat{s}^{L_n}$ are the optimal estimations of x^{L_n} and s^{L_n}, respectively.

However, the latent decomposed wave signals $\Delta\mathbf{h}^L$, which depend on unknown leak parameters, cannot be directly observed. Therefore, an indirect but efficient method is proposed to decompose the composite wave signal.

3.3.2.2 Iterative Beamforming for Localizing Multiple Leaks

This sub-section presents an iterative beamforming algorithm adapted for the time domain. The algorithm's core principle, sequentially decomposing a composite leak signal to localize individual sources, is adopted from its frequency-domain applications (Wang & Ghidaoui, 2019). By integrating this principle with the single-leak detection algorithm introduced in Section 3.2.2, an efficient approach for multiple leak localization in the time domain is developed.

Let $\mathbf{\Phi} = \{\mathbf{x}^L, \mathbf{s}^L\}$ be the unknown leak parameter vector. Its log-likelihood function is

$$\ell(\mathbf{\Phi}) = \ln \mathcal{P}(\Delta\mathbf{h} \mid \mathbf{\Phi}) = \ln \sum_{\Delta\mathbf{h}^L} \mathcal{P}(\Delta\mathbf{h} \mid \Delta\mathbf{h}^L, \mathbf{\Phi}) \mathcal{P}(\Delta\mathbf{h}^L \mid \mathbf{\Phi}) \tag{3.47}$$

where $\mathcal{P}(\cdot)$ is the probability.

Iterative beamforming maximizes $\ell(\mathbf{\Phi})$ by iterative procedures. Assume $\mathbf{\Phi}_{j-1}$ is the estimation of $\mathbf{\Phi}$ after $j-1$ iterations. The objective of a new iteration is to update $\mathbf{\Phi}$ by increasing the log-likelihood function $\ell(\mathbf{\Phi})$. It is derived in Appendix B and shown in the following equation that $\ell(\mathbf{\Phi})$ is the upper bound of $\mathcal{Q}(\mathbf{\Phi} \mid \mathbf{\Phi}_{j-1})$.

$$\ell(\mathbf{\Phi}) \geq \underbrace{\ell(\mathbf{\Phi}_{j-1}) + \sum_{\Delta\mathbf{h}^L} \mathcal{P}(\Delta\mathbf{h}^L \mid \Delta\mathbf{h}, \mathbf{\Phi}_{j-1}) \ln \frac{\mathcal{P}(\Delta\mathbf{h} \mid \Delta\mathbf{h}^L, \mathbf{\Phi}) \mathcal{P}(\Delta\mathbf{h}^L \mid \mathbf{\Phi})}{\mathcal{P}(\Delta\mathbf{h}^L \mid \Delta\mathbf{h}, \mathbf{\Phi}_{j-1}) \mathcal{P}(\Delta\mathbf{h} \mid \mathbf{\Phi}_{j-1})}}_{\mathcal{Q}(\Phi \mid \Phi_{j-1})} \tag{3.48}$$

As proved by Eq. (B4) in Appendix B, it is interesting, perhaps even remarkable, that the function $\ell(\mathbf{\Phi})$ coincides with the function $\mathcal{Q}(\mathbf{\Phi} \mid \mathbf{\Phi}_{j-1})$ at $\mathbf{\Phi}$ = $\mathbf{\Phi}_{j-1}$. Formally, this is expressed as

$$\mathcal{Q}(\mathbf{\Phi}_{j-1} \mid \mathbf{\Phi}_{j-1}) = \ell(\mathbf{\Phi}_{j-1}) \tag{3.49}$$

The relationship between the two functions $\ell(\mathbf{\Phi})$ and $\mathcal{Q}(\mathbf{\Phi} \mid \mathbf{\Phi}_{j-1})$ governed by Eqs. (3.48) and (3.49) is qualitatively illustrated in Figure 3.1. The aim is to estimate the unknown $\mathbf{\Phi}$ by maximizing $\ell(\mathbf{\Phi})$ whose explicit form is unavailable. Fortunately, Figure 3.1 shows that $\ell(\mathbf{\Phi})$ is the upper bound of $\mathcal{Q}(\mathbf{\Phi} \mid \mathbf{\Phi}_{j-1})$ and that two functions $\ell(\mathbf{\Phi})$ and $\mathcal{Q}(\mathbf{\Phi}\,|\,\mathbf{\Phi}_{j-1})$ are equal at $\mathbf{\Phi} = \mathbf{\Phi}_{j-1}$. Therefore, any adjustment to $\mathbf{\Phi}$ that improves $\mathcal{Q}(\mathbf{\Phi}\,|\,\mathbf{\Phi}_{j-1})$ must improve $\ell(\mathbf{\Phi})$. To achieve the largest increase in $\ell(\mathbf{\Phi})$, iterative beamforming selects the $\mathbf{\Phi}$ that maximizes $\mathcal{Q}(\mathbf{\Phi}\,|\,\mathbf{\Phi}_{j-1})$. The updated unknown parameter vector is denoted as $\mathbf{\Phi}_j$, which is expressed by Eq. (B5) in Appendix B as

$$\mathbf{\Phi}_j = \arg\max_{\mathbf{\Phi}}\{\mathcal{Q}(\mathbf{\Phi}\,|\,\mathbf{\Phi}_{j-1})\} = \underbrace{\arg\max_{\mathbf{\Phi}} \underbrace{\left\{\mathbb{E}\left[\ell(\mathbf{\Phi}\,|\,\Delta\mathbf{h}^L)\,|\,\Delta\mathbf{h},\mathbf{\Phi}_{j-1}\right]\right\}}_{\text{Step 1: expectation}}}_{\text{Step 2: maximization}} \quad (3.50)$$

where argmax is the argument of the maximum, and $\mathbb{E}(\cdot)$ is expectation.

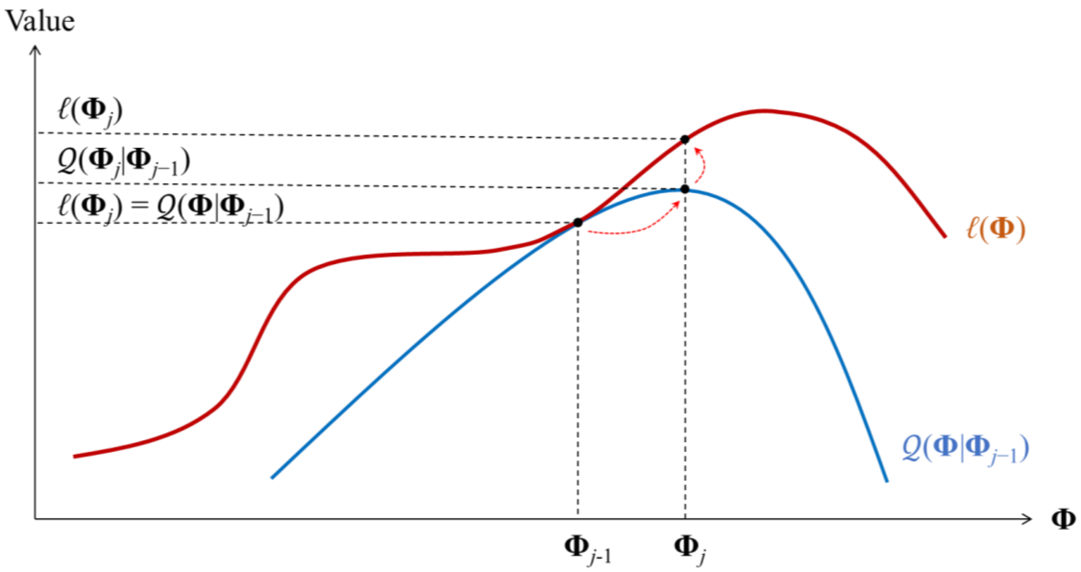

Figure 3.1 Graphical illustration of a single iteration of the iterative beamforming algorithm

Given an initial parameter $\mathbf{\Phi}_0 = \{\mathbf{x}_0^L, \mathbf{s}_0^L\}$, the localization of multiple leaks is realized by iteratively alternating between the expectation and maximization steps of Eq. (3.50) until convergence is achieved:

Step 1: expectation (E-step)

For localizing multiple leaks, the E-step estimates the optimal decomposed wave signals $\Delta\mathbf{h}_j^{L_n}$ after the j-th iteration. The specific form of the conditional expectation is Eq. (C6) in Appendix C and is expressed as

$$\mathbb{E}\left[\ell(\mathbf{\Phi} \mid \Delta\mathbf{h}^{L}) \mid \Delta\mathbf{h}, \mathbf{\Phi}_{j-1}\right] = -\sum_{n=1}^{N} \left\| \Delta\mathbf{h}_j^{L_n} - s^{L_n}\mathcal{G}(x^{L_n}) \right\|_2^2 + c \tag{3.51}$$

where c is constant.

Step 2: maximization (M-step)

Given the optimal decomposed wave signals $\Delta\mathbf{h}_j^{L_n}$, the M-step updates x^{L_n} and s^{L_n} by maximizing the conditional expectation in Eq. (3.51) with respect to $\mathbf{\Phi}$, which decomposes the original N leak localization problem into the following N single leak localization problems

$$\{\hat{x}_j^{L_n}, \hat{s}_j^{L_n}\} = \arg\min_{x^{L_n}, s^{L_n}} \left\| \Delta\mathbf{h}_j^{L_n} - s^{L_n}\mathcal{G}(x^{L_n}) \right\|_2^2, n = 1, 2, ..., N \tag{3.52}$$

where $\hat{x}_j^{L_n}$ and $\hat{s}_j^{L_n}$ are the optimal estimation of x^{L_n} and s^{L_n} after the j-th iteration, respectively. The N two-dimensional minimization problems in Eq. (3.52) can be further decomposed into $2N$ one-dimensional search problems.

For any estimated leak location $x_j^{L_n}$, its corresponding leak size is

$$\hat{s}_j^{L_n} = \arg\min_{s^{L_n}} \left\| \Delta\mathbf{h}_j^{L_n} - s^{L_n}\boldsymbol{\mathcal{G}}(x_j^{L_n}) \right\|_2^2 = \frac{\boldsymbol{\mathcal{G}}^T(x_j^{L_n})\Delta\mathbf{h}_j^{L_n}}{\boldsymbol{\mathcal{G}}^T(x_j^{L_n})\boldsymbol{\mathcal{G}}(x_j^{L_n})} \tag{3.53}$$

Substituting Eq. (3.53) into Eq. (3.52) gives the leak location estimation

$$\begin{aligned} \hat{x}_j^{L_n} &= \arg\min_{x^{L_n}} \left\| \Delta\mathbf{h}_j^{L_n} - \frac{\boldsymbol{\mathcal{G}}(x_j^{L_n})\boldsymbol{\mathcal{G}}^T(x_j^{L_n})}{\boldsymbol{\mathcal{G}}^T(x_j^{L_n})\boldsymbol{\mathcal{G}}(x_j^{L_n})}\Delta\mathbf{h}_j^{L_n} \right\|_2^2 \\ &= \arg\min_{x^{L_n}} \underbrace{(\Delta\mathbf{h}_j^{L_n})^T \frac{\boldsymbol{\mathcal{G}}(x_j^{L_n})\boldsymbol{\mathcal{G}}^T(x_j^{L_n})}{\boldsymbol{\mathcal{G}}^T(x_j^{L_n})\boldsymbol{\mathcal{G}}(x_j^{L_n})}\Delta\mathbf{h}_j^{L_n}}_{B^2} \end{aligned} \tag{3.54}$$

Therefore, the iterative beamforming algorithm decomposes the complex 2N-dimensional optimization problem into 2N sequential one-dimensional sub-problems, which successfully resolves the aforementioned Problem 2.

CHAPTER 4 LEAK DETECTION IN RPV SYSTEM

4.1 Introduction

Building on the parameter separation approach combined with the iterative beamforming method developed in Chapter 3, this chapter focuses on the numerical and experimental validation of the proposed leak detection framework in a reservoir-pipe-valve (RPV) system. The validation begins with an experimental single leak case to illustrate the basic working mechanism of the method, followed by two leak cases for a more comprehensive evaluation through both numerical simulations and experimental tests.

4.2 Single Leak Detection in RPV System

4.2.1 Numerical application and experimental validation in the RPV system

In this section, a simple RPV system is first studied through both experimental and numerical applications to understand how the method works and to verify its validity and accuracy. In principle, as outlined in Algorithm 1, the proposed time-domain parameter separation method is applicable to different types of pipeline systems (e.g., varying pipe materials and configurations), provided that the numerical model for pipe network simulation and the measured signal data are sufficiently accurate. Therefore, a viscoelastic pipe system in the laboratory was selected for experimental validation. The numerical model developed by Pan et al. (2022) is adopted for implementation. At the same time, a numerical simulation of the same system is conducted to generate synthetic transient signals, which are then used as input for leak detection. The results obtained using simulated signals are compared with those from experimental measurements in order to evaluate the impact of data accuracy on the performance of the proposed method.

The configuration of the RPV system with a viscoelastic pipe is presented in Figure 4.1, consisting of an upstream reservoir/tank, an HDPE pipeline, and a downstream valve. Key system parameters are also listed in Figure 4.1. The available head of the upstream tank (H_0) in the system is maintained at 16.19m, and the initial steady-state flow rate (Q_0) is set to 4.5×10^{-3} m^3/s. For testing, the leak is located at 129.53 m from the upstream tank (i.e., dimensionless location x^{L*}=0.779), with the orifice opening C_dA_L being $1.2\times10^{-4}\,\text{m}^2$, equivalent to the leak flowrate Q_0^L = 2.1×10^{-3} m^3/s. The transient wave is initiated by a non-linear valve closure at the downstream, with a closure time t_v = 0.083s. The generated transient wave propagates along the pipe with a wave speed (a) of 377.15 m/s with a sampling frequency (f_s) of 2048Hz (Pan et al., 2022). The pressure transducer is installed just upstream of the valve for signal data collection. The numerical simulation is conducted using the Method of Characteristics (MOC), in which the whole pipeline is evenly distributed into 903 nodes based on the wave speed and data collection time step ($1/f_s$) to match the experimental data resolution. To ensure consistency between the numerical and experimental systems, the calibrated parameters in Figure 4.1 and Pan et al. (2022) are applied for this system, placing the leak accordingly at the 704th discrete point.

Following the detection procedure outlined in Chapter 3, the measured transient signal corresponding to approximately the first two wave periods, which is about 3.5 seconds long, is first simulated. This time interval ensures that the pressure wave sufficiently propagates throughout the entire system. The transient responses obtained from both the numerical simulation and the experimental measurement are presented in Figure 4.2.

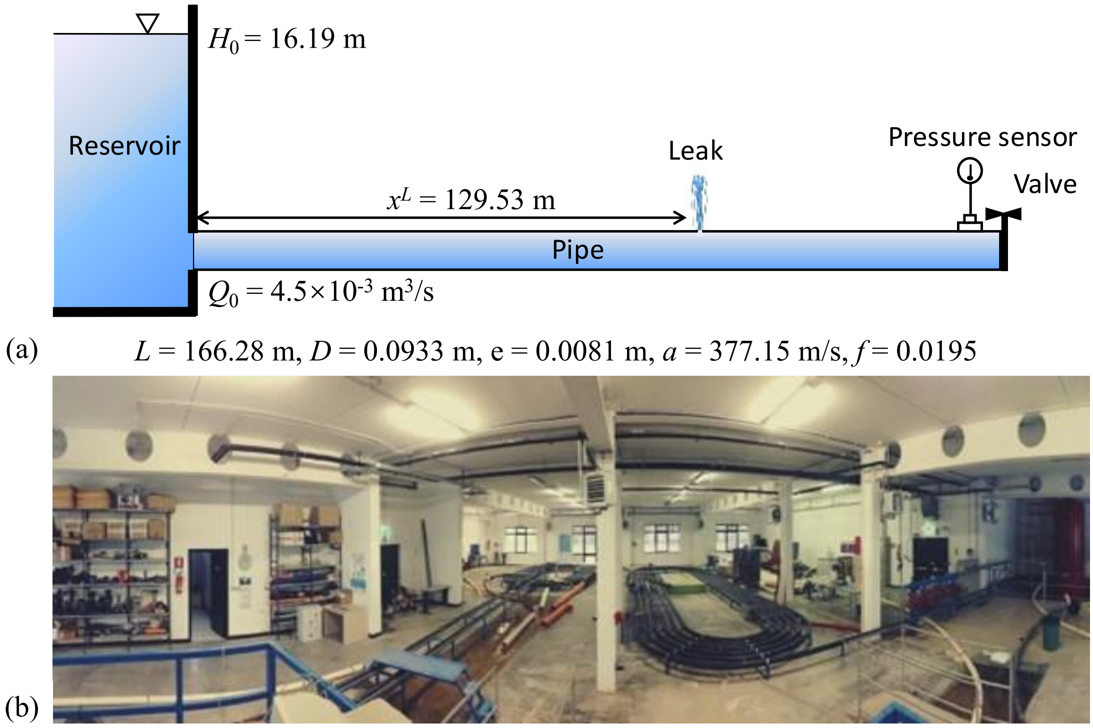

Figure 4.1 Simplified system setup for experimental RPV system with a single leak: (a) system configuration; (b) experimental test system setup

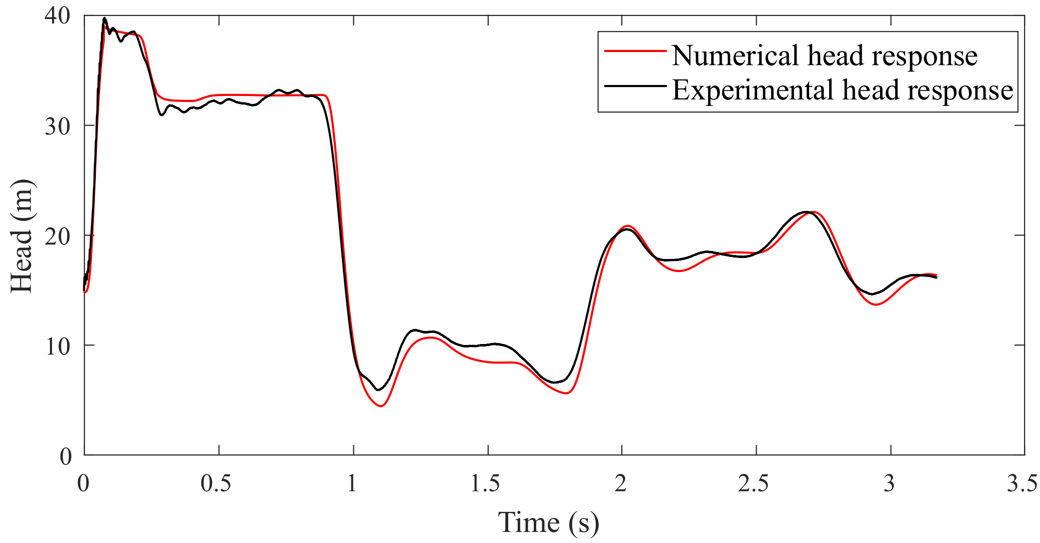

Figure 4.2 Numerical and experimental transient head response in the experimental RPV system with a single leak

Following Algorithm 1 and facilitating further investigation of the leak-related signal features, the simulated initial pipe transient signal $\mathbf{h}^{NL}$ (i.e., the non-leak case) is subtracted from both numerical and experimental transient signals. The resulting objective function values for leak localization, calculated according to

$$\left\{\hat{x}^L\right\} = \arg\max_{x^L}\left(\Delta\mathbf{h}^T\mathcal{G}(x^L)\frac{\mathcal{G}(x^L)^T\Delta\mathbf{h}}{\mathcal{G}(x^L)^T\mathcal{G}(x^L)}\right) = \arg\max_{x^L}(B^2) \tag{4.1}$$

are plotted in Figure 4.3. In this figure, the vertical dashed lines indicate the actual leak location (shown in blue) and the two global maxima of the objective functions for both numerical and experimental cases. The numerical estimate along the red dashed line has a relative error of approximately 0.13% (i.e., =0.780), while the experimental estimate along the black dashed line shows an error of about 0.77% (i.e., =0.785). Notably, the numerical result slightly outperforms the experimental one. This is expected, as the numerical simulation is free from measurement noise and modeling uncertainty, even though it still relies on simplified assumptions about the physical system. Despite these potential limitations, both results present detection localization errors below 1%, demonstrating the high accuracy and robustness of the proposed method in identifying leak positions under both ideal and realistic conditions.

Accordingly, the follow-up application of the method based on

$$\hat{s}^L = \frac{\mathcal{G}(x^L)^T\Delta\mathbf{h}}{\mathcal{G}(x^L)^T\mathcal{G}(x^L)} \tag{4.2}$$

provides leak size (C_dA_L) estimates for both the numerical and experimental cases, and in both applications, the predicted leak sizes are $1.1\times10^{-4}\,\mathrm{m}^2$, exhibit an error of 8.33%, which falls within the acceptable ranges of transient-based methods (Duan et al., 2020).

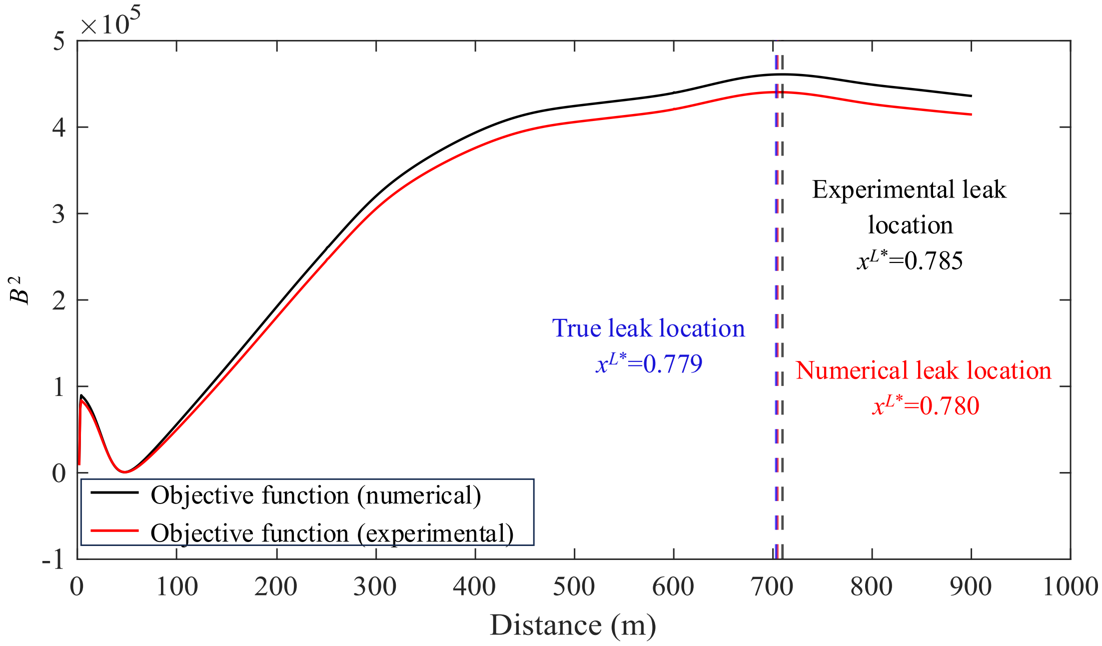

Figure 4.3 Objective functions of leak location in numerical and experimental cases

The results obtained from this RPV system application demonstrate that the proposed two-stage time-domain leak detection method is accurate and applicable for both leak location and size detection for a single leak, with overall errors within 10%. Particularly, the method achieves remarkable localization accuracy, with an error below 1%. Additionally, the results indicate that even when applied to numerically simulated data with limited modeling fidelity, the method maintains strong predictive accuracy. It is significant when applied to experimental data-based applications where complex factors (e.g., pipe materials, valve operations) cannot be fully captured by existing numerical models, as shown in Figure 4.2. The results from both numerical and experimental tests present accurate leak localization, thereby highlighting the applicability and effectiveness of the proposed method when dealing with measurement data with different levels of accuracy.

4.3 Multiple Leak Detection in RPV System

Following the experimental validation of single leak detection using the proposed parameter separation method, this section extends the analysis to multiple leak detection in the RPV system. The discussion begins with a numerical example to provide an intuitive understanding of the factorized wave model for multiple leaks. This is followed by the application of iterative beamforming to decompose composite wave signals, and subsequent leak localization through both numerical simulations and experimental validation.

4.3.1 Numerical illustration of the factorized wave model

This section presents a simple noise-free numerical example to illustrate the factorized transient wave model for multiple leaks. The RPV system configuration and key parameters are shown in Figure 4.4. In this setup, the upstream reservoir maintains a constant head (H_0) of 80 m, and a pressure sensor is installed near the downstream valve to record wave signals. The pipe has a length (L) of 200 and a diameter (D) of 0.5 m. The steady-state friction factor (f) is 0.02, and the transient wave runs with a speed (a) of 1000 m/s. With the valve fully open, the initial steady downstream discharge (Q_0) is 0.1 m^3/s. A pulse-shaped transient wave is generated by a fast valve perturbation, in which the downstream valve opening changes from 100% to 80% and then back to 100% within 20 ms.

Three numerical tests are conducted: (1) with only Leak 1, (2) with only Leak 2, and (3) with both leaks present simultaneously. Leak 1 is located at $x^{L1} = 50$ m with size $s^{L1} = 5.6\times10^{-5}$ m^2/s ($Q_0^{L1} \approx 9\% Q_0$), while Leak 2 is at $x^{L2} = 160$ m with $s^{L2} = 8.75\times10^{-5}$ m^2/s ($Q_0^{L2} \approx 14\% Q_0$), respectively. The wave signals are measured by the pressure sensor at a sampling frequency of 1 kHz, from which the leak-induced pressure differences are computed and plotted in Figure 4.5.

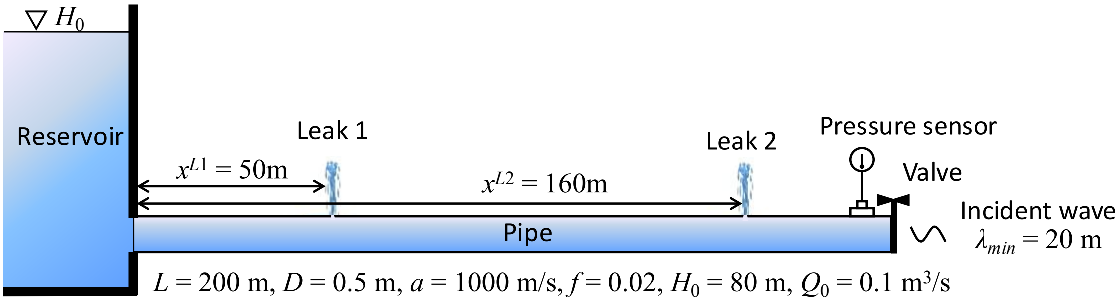

Figure 4.4 Numerical case setup for RPV system with multiple leaks

Figure 4.5 (a) and 4.5(b) show the leak-induced pressure difference $\Delta\mathbf{h}^{L1}$ and $\Delta\mathbf{h}^{L2}$ for Leak 1 and Leak 2, respectively. Each signal contains reflected waves originating from both the leak location and the upstream reservoir, observed within the first two wave periods ($8\ L/a = 1.6$ s). Figure 4.5(c) shows the linear superposition of $\Delta\mathbf{h}^{L1}$ and $\Delta\mathbf{h}^{L2}$ in pink and the pressure difference $\Delta\mathbf{h}$ induced by the co-existence of Leaks 1 and 2 in black. It can be observed that $\Delta\mathbf{h}$ matches closely with $\Delta\mathbf{h}^{L1} + \Delta\mathbf{h}^{L2}$, with only minor discrepancies in the enlarged view caused by higher-order interactions between the two leaks. These differences are negligibly minor, thereby providing a clear graphical illustration of the physical interpretation of the factorized wave model described in Eq. (3.43), which is

$$\Delta\mathbf{h} = \sum_{n=1}^{N} s^{L_n} \mathcal{G}(x^{L_n}) + \mathbf{n} = \sum_{n=1}^{N} \Delta\bar{\mathbf{h}}^{L_n} + \mathbf{n} \tag{4.3}$$

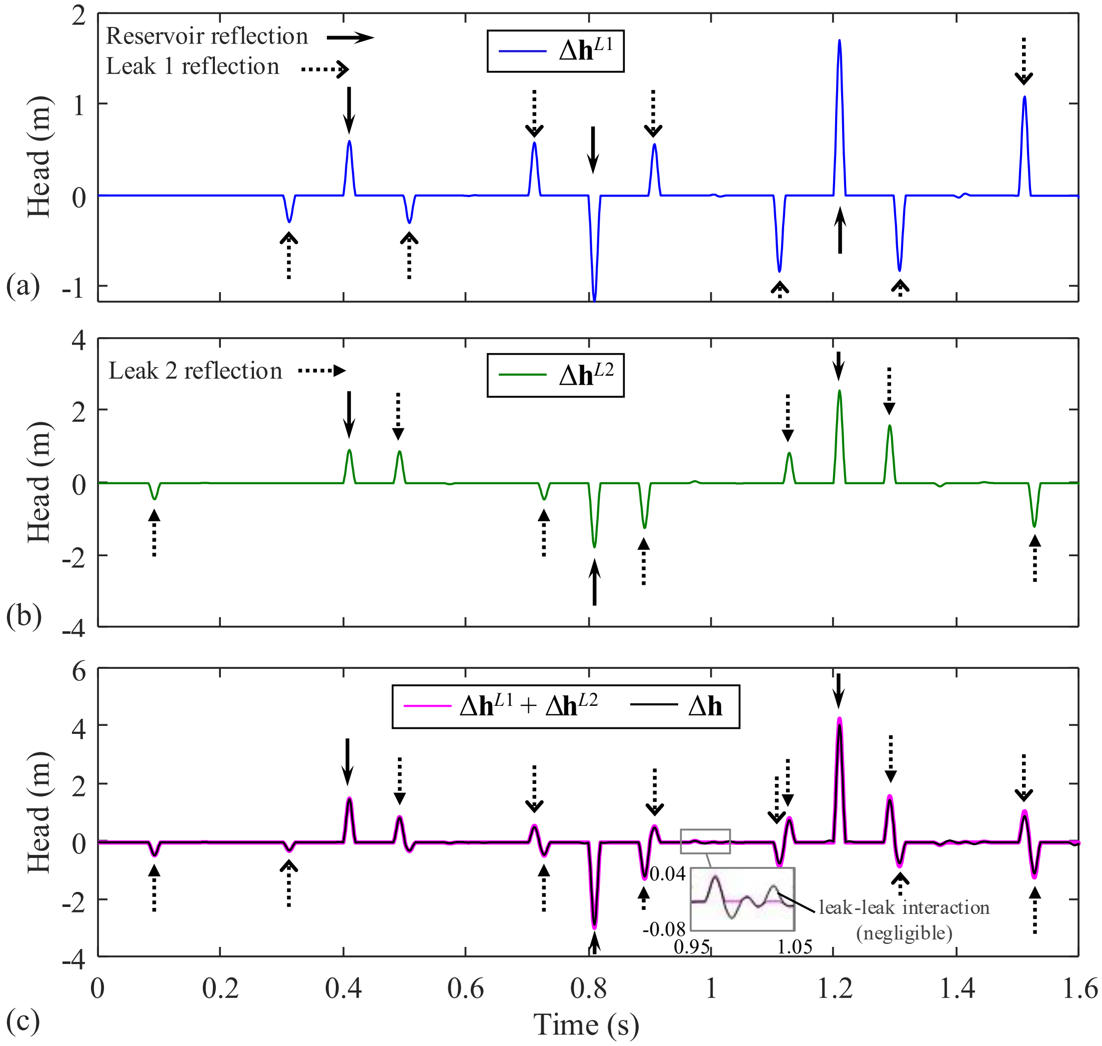

Figure 4.5 Leak-induced pressure differences for three tests: (1) pressure difference $\Delta\mathbf{h}^{L1}$ of Leak 1, (2) pressure difference $\Delta\mathbf{h}^{L2}$ of Leak 2, and (3) linear superposition of $\Delta\mathbf{h}^{L1}$ and $\Delta\mathbf{h}^{L2}$ and the total pressure difference of Leaks 1 and 2

4.3.2 Composite wave signal decomposition and multiple leak localization

Concerning the RPV system described above, featuring identical leak location and size, the capability of the proposed approach for composite wave signal decomposition and the localization of multiple leaks is evaluated. The transient wave signal is measured and plotted in Figure 4.6(a) with zero-mean Gaussian white noise added to $\Delta\mathbf{h}$. The signal-to-noise ratio (SNR) of the noise is 0 dB, defined by

$$\mathrm{SNR} = 20\log_{10}\left(\frac{\overline{|\mathrm{E}(\Delta \mathrm{h})|}}{\sigma}\right) \tag{4.4}$$

where $\overline{|\mathbb{E}(\Delta \mathrm{h})|}$ is the average of the leak-induced pressure difference. The noise level at SNR = 0 dB means $\sigma = \overline{|\mathbb{E}(\Delta \mathrm{h})|}$.

Iterative beamforming is applied to decompose the composite wave signal $\Delta\mathbf{h}$ and to localize multiple leaks. Upon convergence, the final decomposed transient waves and leak localization results are shown in Figures 4.6(b) and 4.6(c). As illustrated in Figure 4.6(b), $\Delta\mathbf{h}$ is successfully separated into two distinct components, $\Delta\mathbf{h}^{L1}$ and $\Delta\mathbf{h}^{L2}$, corresponding to Leak 1 and Leak 2, respectively. This decomposition effectively transforms the original two-leak localization problem into two single-leak localization problems. In Figure 4.6(c), the vertical dashed lines denote the actual leak locations, while the objective functions B^2 reach their global maxima at these locations, confirming that both leaks are successfully identified.

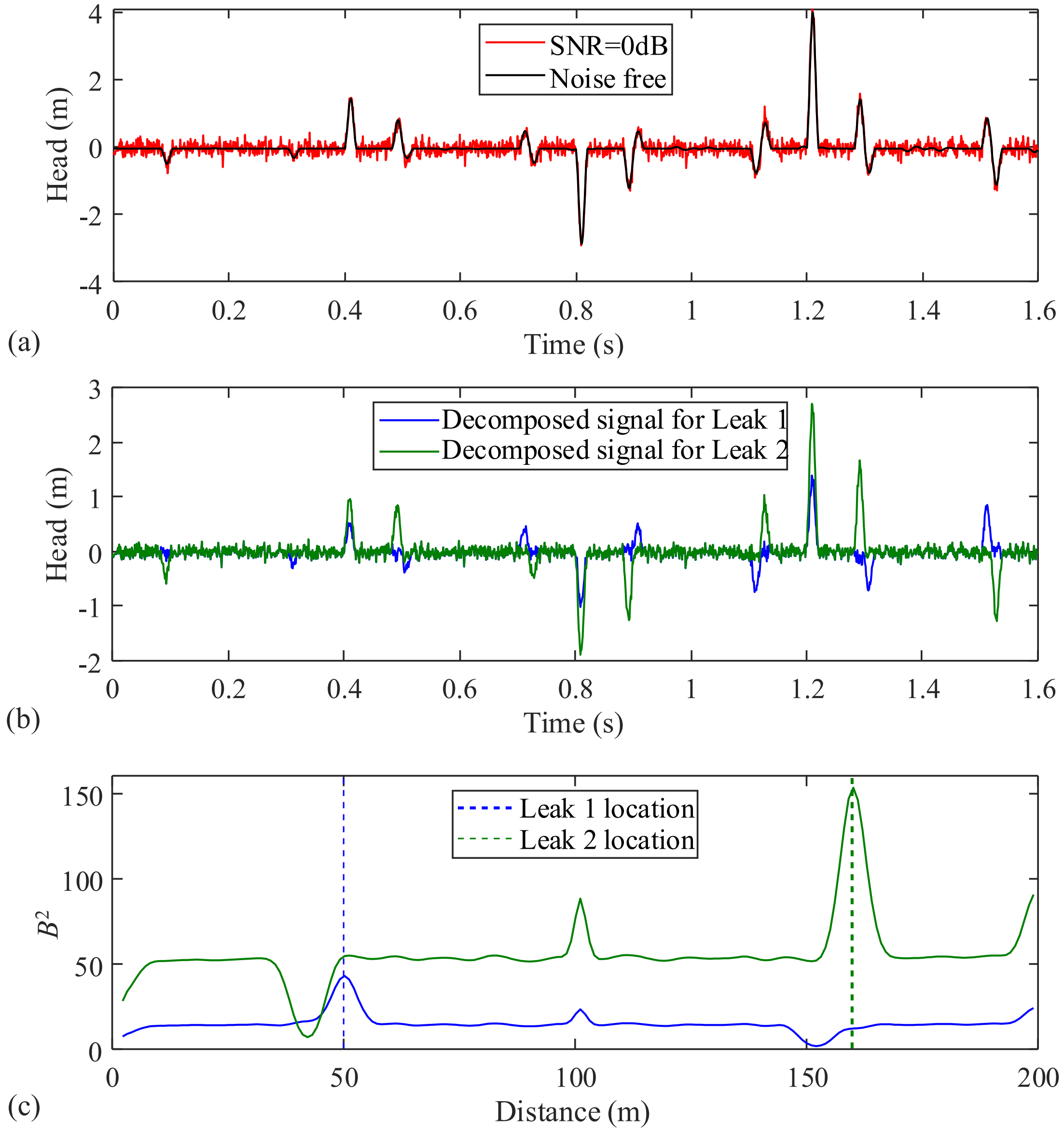

Figure 4.6 Composite wave signal decomposition and multiple leak localization: (a) composite wave signals; (b) decomposed wave signals; (c) leak localization based on the decomposed wave signals

4.3.3 Different noise levels

In practice, urban water supply systems operate under complex noise conditions, including traffic noise and turbulence-induced fluctuations. This sub-section compares the accuracy and efficiency of the proposed approach with the conventional time-domain FWI method for localizing multiple leaks at different noise levels. Gaussian white noise at different levels is superimposed on each leak-induced transient signal, with signal-to-noise ratios (SNRs) ranging from 10 dB to -10 dB.

In this test, the two leaks are located at $x^{L1} = 50$ m and $x^{L2} = 160$ m with the leak sizes of $s^{L1} = 6.25\times10^{-5}$ m^2/s ($Q_0^{L1} \approx 10\% Q_0$) and $s^{L2} = 7.5\times10^{-5}$ m^2/s ($Q_0^{L2} \approx 12\% Q_0$), respectively. Three representative transient wave signals with SNR = 10, 0, and -10 dB are shown in Figure 4.7, illustrating the progressive increase in noise level as SNR decreases. More specifically, Specifically, at SNR = 0 dB (Figure 4.7(b)), the amplitude of the first reflections from both leaks is comparable to that of the noise (i.e., $\sigma = \overline{|\mathbb{E}(\Delta \mathrm{h})|}$). At SNR = -10 dB (Figure 4.7(c)), the noise amplitude is approximately three times that of the first reflections (i.e., $\sigma \approx 3\overline{|\mathbb{E}(\Delta \mathrm{h})|}$), which makes it challenging for leak localization. As indicated in Eq. 3.25, unlike the proposed approach, the conventional FWI method localizes leaks based on the raw measured signals $\mathbf{h}^{obs}$ with noise, instead of the leak-induced pressure difference $\Delta\mathbf{h}$.

Particle swarm optimization (PSO) is adopted as the optimization algorithm in the conventional FWI method (Jung & Karney, 2008). The numbers of particles and iterations are set as 300 and 20, respectively. For each SNR, the procedures from numerical simulation to leak localization of both approaches are repeated 25 times on a personal computer with 3.8 GHz Ultra 7-155H CPU and 16 GB RAM. The average execution time for each test of the conventional FWI method and the proposed approach is 71s and 0.68s, respectively. The efficiency gain of the proposed approach enables real-time leak localization, which can be attributed to the decomposition of the complex 4-dimensional optimization problem into 4 sequential one-dimensional sub-problems. The average localization errors of Leaks 1 and 2 and their standard deviations are plotted in Figure 4.8. Results show that that both approaches can accurately localize both leaks for SNR ranging from -5 to 10 dB, with the proposed approach outperforming the conventional FWI method. Even under the highly challenging condition of SNR = -10 dB in Figure 4.8(c), the proposed approach can still accurately localize Leak 2 (i.e., the larger leak). For Leak 1 (i.e., the small leak), the mean localization error is 2.2 m, which remains acceptable as it is below the theoretical diffraction limit, defined as half of the minimum probing wavelength $\lambda_{min}/2 = a \cdot t_v/2 = 10$ m. However, the conventional FWI method fails to localize both leaks, as their average localization errors are larger than $\lambda_{min}/2$.

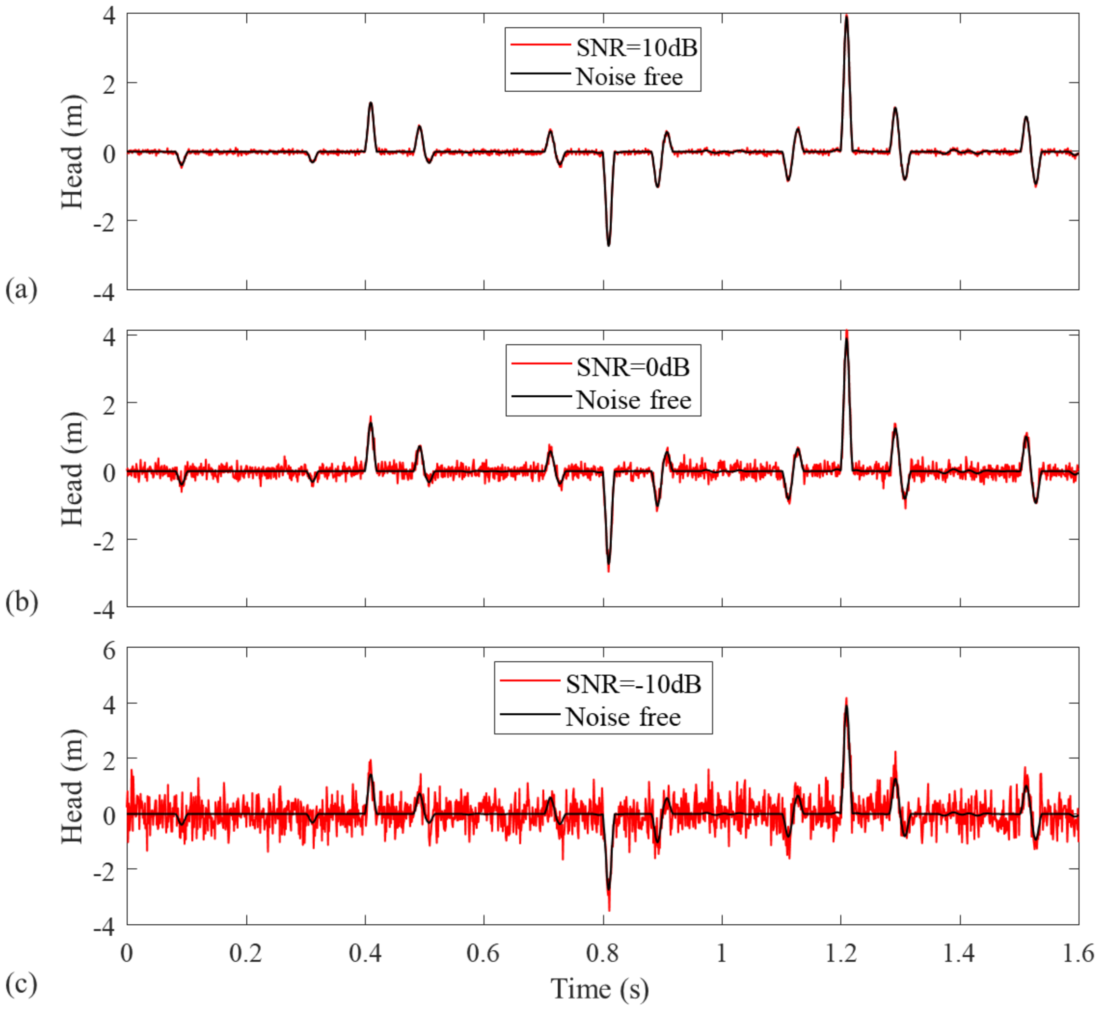

Figure 4.7Composite wave signals at different noise levels: (a) SNR = 10 dB; (b) SNR = 0 dB; (c) SNR = -10 dB

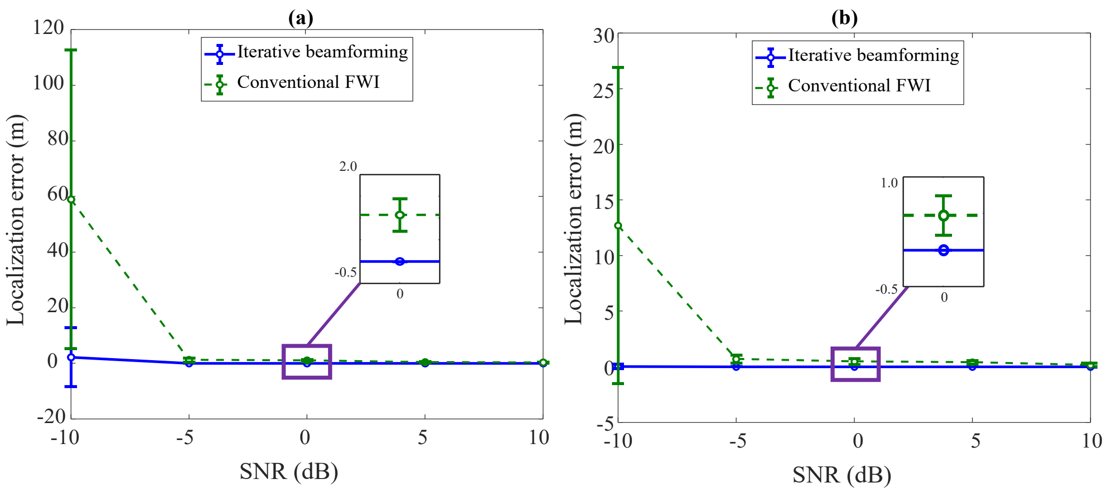

Figure 4.8 Leak localization errors and standard deviations at different noise levels: (a) Leak 1; (b) Leak 2

4.3.4 Super-resolution of adjacent leaks

Besides noise robustness, the method's spatial resolution is also evaluated. The leak localization accuracy is defined as the difference between the actual and estimated leak positions. Due to the diffraction limit, two adjacent leaks cannot be reliably distinguished if their separation distance is less than half of the minimum probing wavelength $\lambda_{min}/2$. In this section, the super-resolution capability of the proposed method is evaluated by testing its performance in closely spaced leak cases.

In the same RPV system, Leak 1 is located at x^{L1} = 50 m, while Leak 2 is placed at three different locations: x^{L2} = 65 m, 60 m, and 57 m, corresponding to separation distances Δx^L of 15 m ($0.75\lambda_{min}$), 10 m ($0.5\lambda_{min}$), and 7 m ($0.35\lambda_{min}$), respectively. Both leaks have the same sizes, $s^{L1} = s^{L2} = 6.25\times10^{-5}$ m^2/s ($Q_0^{L1} = Q_0^{L2}$ $\approx 10\% Q_0$). Gaussian white noise of SNR = 0 dB is added to all the systems. The composite transient wave signals and the localization results are plotted in Figure 4.9.

As illustrated in Figures 4.9 (a) and 4.9(b), for $\Delta x^L = 0.75\lambda_{min}$, both first and second reflections from the transient response of Leaks 1 and 2 are clearly distinguishable, allowing straightforward identification of both leaks.. When Δx^L = $0.5\lambda_{min}$, both reflections remain distinguishable but show partial overlap (Figure 4.9(c)), nevertheless, the two leaks can still be resolved, as shown in Figure 4.9(d). For $\Delta x^L = 0.35\lambda_{min}$, the reflections from the two leaks are heavily overlapped and difficult to distinguish, particularly under noise interference (Figure 4.9(e)). Remarkably, the proposed method still achieves super-resolution of two leaks under such challenging conditions (Figure 4.9(f)), where the distance between the two leaks is less than the theoretical diffraction limit.

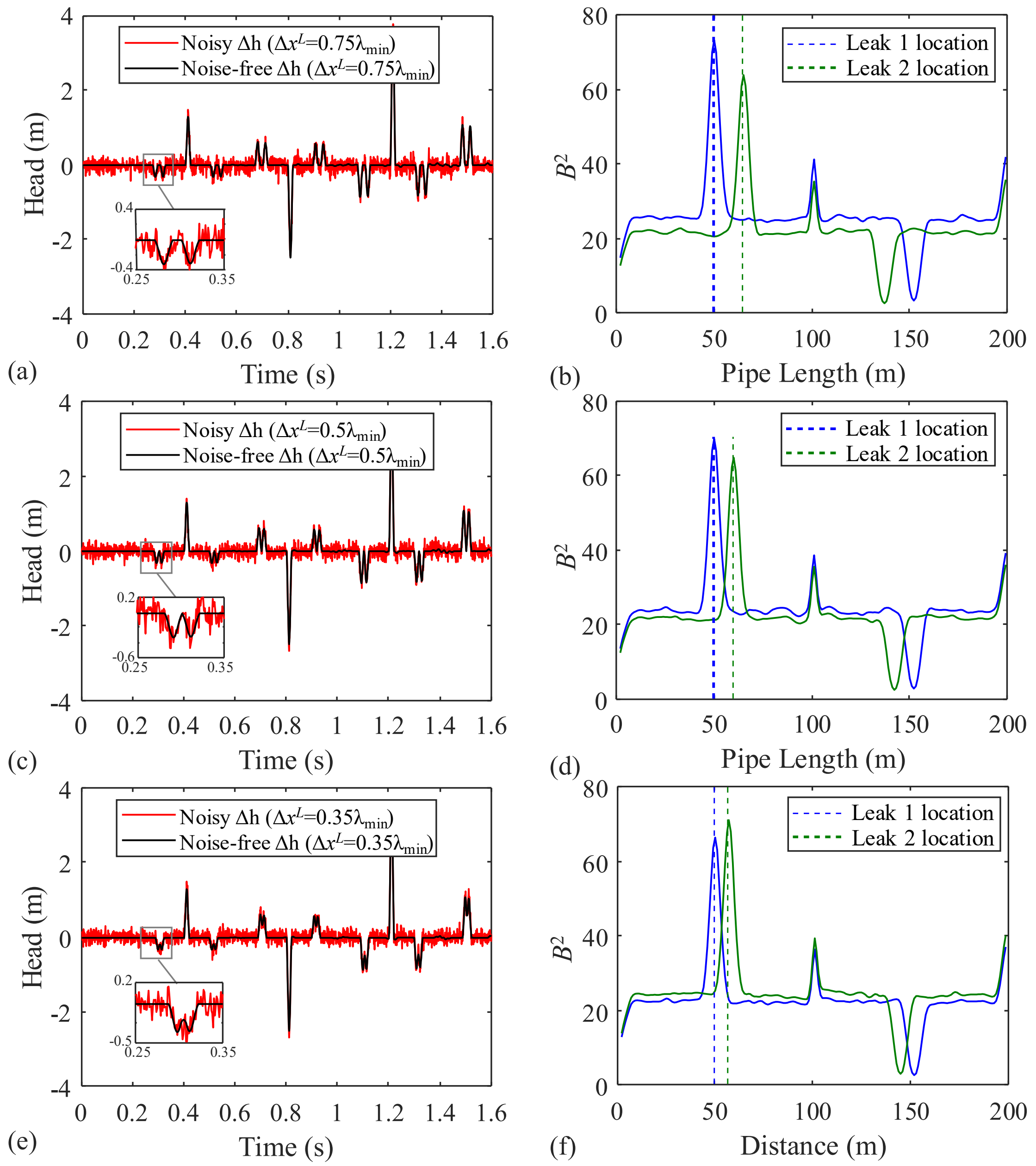

Figure 4.9 Super-resolving two adjacent leaks: (a) composite wave signals for $\Delta x^L = 0.75\lambda_{\min}$; (b) leak localization results for $\Delta x^L = 0.75\lambda_{\min}$; (c) composite wave signals for $\Delta x^L = 0.5\lambda_{\min}$; (d) leak localization results for $\Delta x^L = 0.5\lambda_{\min}$; (e) composite wave signals for $\Delta x^L = 0.35\lambda_{\min}$; (f) leak localization results for $\Delta x^L = 0.35\lambda_{\min}$

4.3.5 Unknown leak number

In the previous sections, multiple leaks are identified assuming that leak number N is a known parameter, which is difficult to determine in practice. Therefore, the capacity of the proposed method is assessed when the number of leaks is unknown.

Two leaks, located at x^{L1} = 50 m and x^{L2} = 160 m and sizes of $s^{L1} = 6.25\times10^{-5}$ m^2/s ($Q_0^{L1} \approx 10\% Q_0$) and $s^{L2} = 7.5\times10^{-5}$ m^2/s ($Q_0^{L2} \approx 12\% Q_0$), are tested respectively. The noise level is fixed at SNR = 0 dB. Four different assumed leak numbers, N_a = 1,2,3, and 4, are applied for leak localization. The leak number, location, and size estimation results are summarized in Table 4.1.

Table 4.1 Leak number, location, and size estimation results

N_a	$\hat{x}^{L1}$	$\hat{Q}_0^{L1}/Q_0$	$\hat{x}^{L2}$	$\hat{Q}_0^{L2}/Q_0$	$\hat{x}^{L2}$	$\hat{Q}_0^{L3}/Q_0$	$\hat{x}^{L4}$	$\hat{Q}_0^{L4}/Q_0$
1	160	18%	-	-	-	-	-	-
2	**50**	**9.20%**	**160**	**11%**	-	-	-	-
3	**50**	**9.50%**	**160**	**10%**	159	1%	-	-
4	**50**	**8%**	**160**	**10%**	20	1.40%	180	1.20%

As shown in Table 4.1, under the single-leak assumption, only the large leak (Leak 2) is detected. When the assumed leak number matches the actual number (N_a = N = 2), the two leaks are accurately localized. If the assumed leak number exceeds the real number (N_a = 3 or 4), additional "potential" leak locations are identified; however, the false positives are easily distinguished by their negligible flow rates compared to real leaks (i.e., ≈ 1% Q_0). Consequently, the two dominant locations at 50 m and 160 m with relatively large flow rates are confirmed as true leaks.

4.3.6 Laboratory experimental test

Further validation of the proposed method is performed for localizing multiple leaks through laboratory experiments in a viscoelastic system.

The laboratory experiments were conducted by Rahmanshahi et al. (2024). The simplified system setup and some key equipment are shown in Figure 4.10. The system includes an upstream reservoir, a downstream valve, and a pipe made of HDPE, shown in Figure 4.10(b). The upstream reservoir has a constant pressure head (H_0) of 43.26 m, and the initial steady-state flow rate (Q_0) is 2.17 L/s. The pipe length (L) and internal diameter (D) are 158 m and 50.5 mm, respectively. Two leaks are placed at x^{L1} = 56.3 m and x^{L2} = 125 m with sizes of $s^{L1} = 1.52\times10^{-5}$ m^2/s ($Q_0^{L1} \approx$ 20.41%Q_0) and $s^{L2} = 8.16\times10^{-6}$ m^2/s ($Q_0^{L2} \approx$ 10.96%Q_0). A transient wave with a propagation speed of a = 401.75 m/s is generated by a sudden and complete closure of the valve (Figure 4.10(c)) within t_v = 72 ms. The resulting system response is measured by the pressure sensor (Figure 4.10(c)) with a sampling frequency of 1 kHz.

Figure 4.11 shows the experimental transient wave signal, as shown in the figure, the wave signal attenuates rapidly due to the pipe wall viscoelasticity. Two leaks induce evident reflections within the first wave period (i.e., t = 0-1.68 s), whereas these leak features diminish thereafter due to the damping effect. Thus, only the wave signal within the first wave period is used for leak localization.

The transient response of the corresponding leak-free system is computed numerically by MOC, incorporating viscoelastic pipe wall behavior via the Kelvin-Voigt model (Covas et al., 2005), where the creep-compliance and retardation time coefficients are $\mathbf{J} = [0.891,\ 1.321,\ 1.31]\times10^{-10}$ Pa^{-1} and $\boldsymbol{\tau}$ = [0.057, 0.4, 8] s, respectively. To reduce the phase shift between the measured and simulated transient head responses, the transient flow rate during valve closure was inversely estimated from the pressure measurement and set as the valve boundary condition for the simulation. Then, the total leak-induced pressure difference $\Delta\mathbf{h}$ is computed and plotted in Figure 4.12. For comparison, the linear superposition of $s^{L1}\mathcal{G}(x^{L1})$ and $s^{L2}\mathcal{G}(x^{L2})$ is also plotted in the same figure. Despite significant uncertainties, particularly from boundary reflections and wave attenuation, the overall pattern of the experimental $\Delta\mathbf{h}$ agrees well with the numerical simulation $s^{L1}\mathcal{G}(x^{L1}) + s^{L2}\mathcal{G}(x^{L2})$.

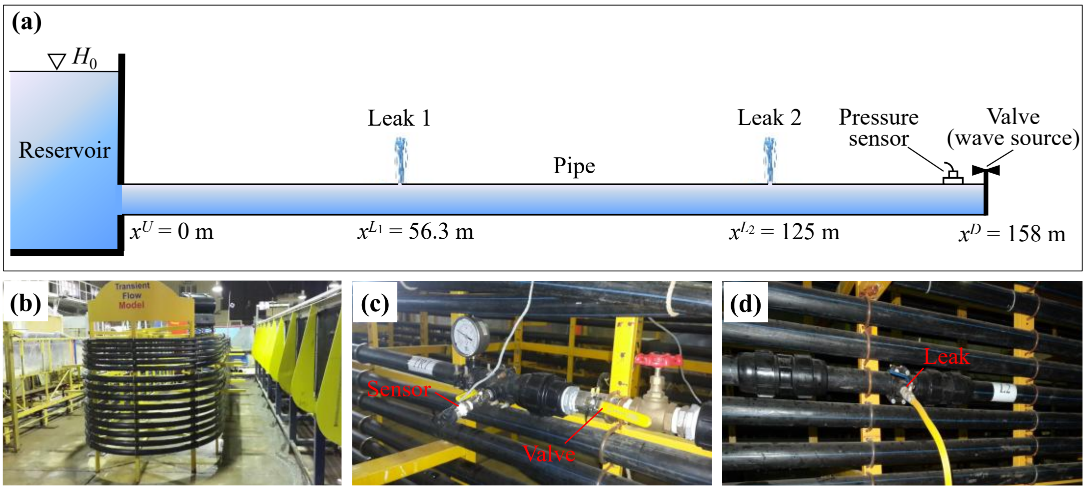

Figure 4.10 Simplified laboratory system setup and some key equipment for experimental RPV system with two leaks: (a) simplified system setup; (b) pipe; (c) pressure sensor and valve; (d) leak

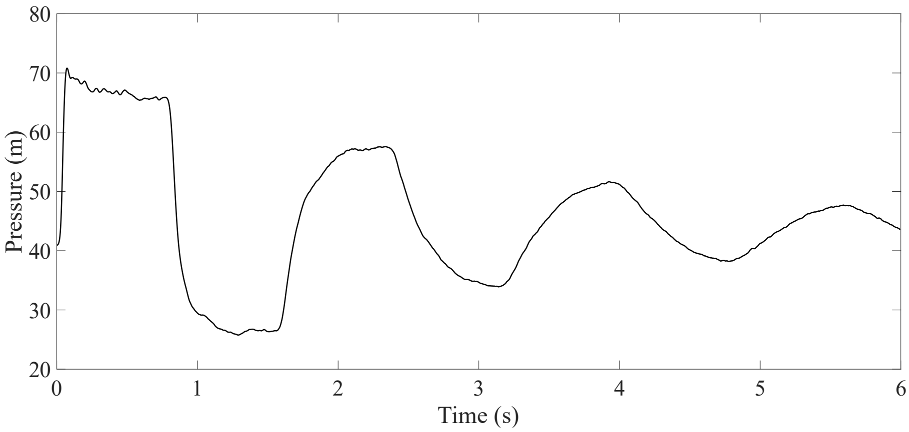

Figure 4.11 Measured wave signal by the pressure sensor

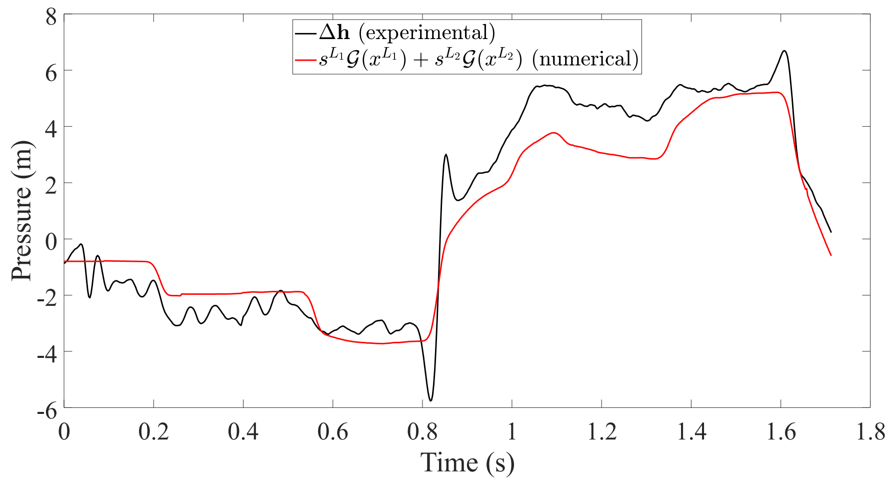

Figure 4.12 The total pressure difference $\Delta\mathbf{h}$ induced by the co-existence of Leaks 1 and 2 (experimental, black curve) and the linear superposition of $s^{L1}\mathcal{G}(x^{L1})$ and $s^{L2}\mathcal{G}(x^{L2})$ (numerical, red curve)

By applying the proposed iterative beamforming, the decomposed signals and the corresponding leak localization results are plotted in Figures 4.13 and 4.14, respectively. The estimated leak locations are $\hat{x}^{L1}$ = 58 m and $\hat{x}^{L2}$ = 137 m, with errors of 1.7 and 12 m, respectively, and fall within the theoretical diffraction limit of $\lambda_{\min}/2$ = 14.46m, making them acceptable results.

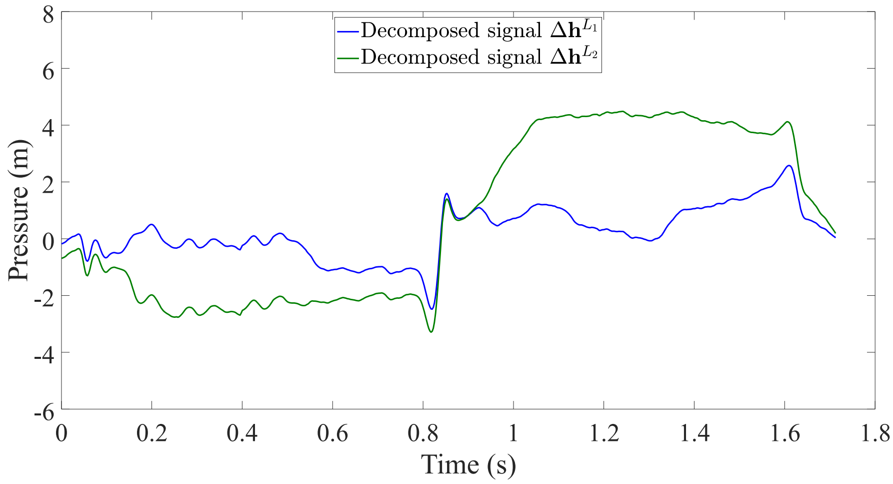

Figure 4.13 Decomposition results of the total leak-induced pressure $\Delta\mathbf{h}$

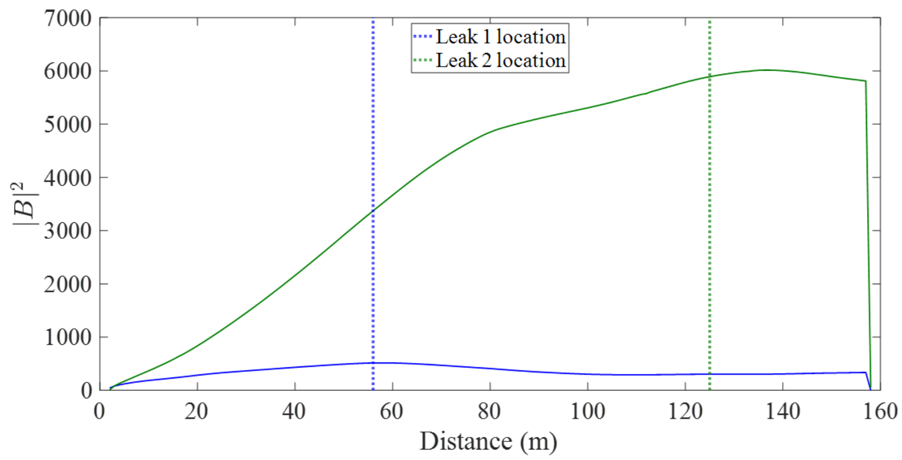

Figure 4.14 Leak localization result of the experimental multiple-leak case

4.4 Summary and Conclusion

In this chapter, numerical and experimental case studies in reservoir-pipe-valve systems are presented to validate the proposed method. The tests are conducted under a wide range of conditions, including different noise levels (SNR from -10 to 10), super-resolution scenarios where the distance between two leaks approaches or falls below the theoretical resolution limit, unknown numbers of leaks in numerical simulations, and viscoelastic pipe materials in laboratory experiments. A total of ten numerical scenarios and two experimental cases are evaluated. In addition, the detection efficiency of the proposed method is compared with that of the conventional time-domain FWI approach.

The numerical results demonstrate that the proposed method is accurate, efficient, super-resolving, and robust in localizing both single and multiple leaks. For SNR $\geqslant$ -5, the estimated leak locations show good agreement with the true leak locations, and the two leaks separated by as little as 0.35 λ min (7 m) are successfully resolved, exceeding the theoretical resolution limit. The proposed approach achieves computational speed approximately a hundred times faster than the traditional method, with typical runtimes of 0.68s compared to 71s. Furthermore, the method is capable of estimating the unknown number of leaks without requiring prior information. Laboratory experiments further confirm that the proposed approach can successfully localize one and two leaks in a viscoelastic pipe system with localization errors within 12m, demonstrating its applicability to realistic pipe materials under controlled experimental conditions.

CHAPTER 5 LEAK DETECTION IN PIPE NETWORK SYSTEM

5.1 Introduction

Building on the numerical and experimental validation of the RPV system presented in Chapter 4, this chapter extends the numerically based implementation of the proposed method to more complex pipe network systems.

Water supply pipe networks are usually divided into different District Metered Areas (DMAs), with each monitored relatively independently. As shown in Figure 5.1, a DMA consists of multiple pipe sections. For system diagnosis, such as leak detection, each pipe section within a DMA can be either intact or leaky, each exhibiting distinct transient wave features and responses. The wave response for each monitor area can be collected, enabling an initial separation of transient wave signals into intact and leaky categories. However, leak diagnosis in these systems is inherently more complex than in single-pipe systems due to factors such as branches, various pipe properties, etc.

Compared to the proposed time-domain leak detection method, similar detection methods in the frequency domain have been adapted for multi-pipe systems with relatively simple setups (e.g., with few branches) (Che, Wang, & Ghidaoui, 2022; Wang et al., 2021). These studies have demonstrated that the transient reflection caused by multi-pipe configurations can be concentrated in the intact-system matrix according to the pipe connection topology, while the leak-induced transient signal presents localized behavior that is consistently reflected by the product of s^L and x^L-related matrix as the arrivals of a transient wave from the leak, regardless of the pipeline in which the leak is situated. Furthermore, it illustrates that the leak-induced perturbation shows a distinct dependence on leak parameters, with the leak size primarily affecting the signal amplitude while the leak location determines the specific frequencies most influenced, enabling the separation of leak size and location for efficient detection.

However, many previous applications (Che, Wang, & Ghidaoui, 2022; Wang et al., 2021) have also indicated that this derived result becomes difficult or even impossible when applied to highly complex pipe networks (e.g., with loops) and/or very complicated flow conditions (e.g., high Reynolds flow). In such cases, the limitations primarily arise from the complexities of transient signal processing, including wave reflections and superposition, the inaccuracy/error of transient flow linearization, and signal truncation for frequency domain analysis based on practical measurements (e.g., using only part of the time series or linearized friction effects). A potential workaround to address these challenges is to extend and map the derived parameter-separation method in the time domain, thereby incorporating time-domain full waveform signals from measurements and/or simulations. From this perspective, the derived results and findings in the frequency domain of previous studies could serve as a theoretical basis for the proposed time-domain method development in this study, and the numerical-based application is considered.

In this chapter, the proposed leak detection method is applied to a numerical pipe network system for single leak detection. A numerical validation of leak location and size separation within the network system is also provided to demonstrate their separability numerically.

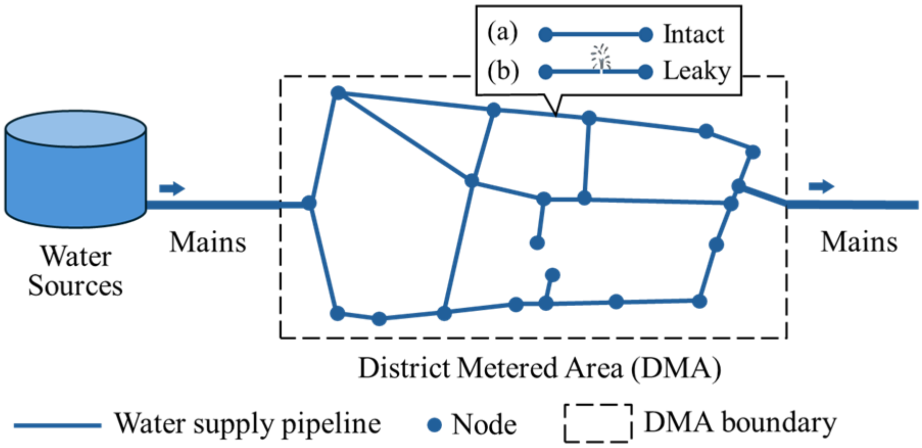

Figure 5.1 Water supply pipe network and two states of the pipe section: (a) intact state, (b) leaky state

5.2 Numerical case setup

In this section, a 5-loop pipe network is used to evaluate the applicability, accuracy, and robustness of the proposed method in the multi-pipe system. The network is adapted from the classical pipe network of Liggett and Chen (1994) and generalized through parameter variations to enable a broader solution. The schematic and basic settings of this network are shown in Figure 5.2, and the detailed pipe parameters, length (L) and diameter (D) of each pipe section, are listed in Table 5.1. Three numerical cases are designed for comprehensive testing under noise-free conditions. The first two cases, namely Case N1 and Case N2, are designed to evaluate this method's performance under different measurement distances (i.e., the distance between the leak location and the pressure sensor). The third case, Case N3, examines the method's performance under varying steady-state flow rates. After obtaining the detection results in the noise-free cases, different levels of Gaussian white noise are added to simulate transient signals under realistic operational environments. The results for the noisy cases are then analyzed and discussed accordingly.

The pipe network is simulated using the MOC, with each pipe section discretized at 1 m intervals, following the sampling frequency of 1 kHz. In Case N1 and Case N2, the leaks are located at x^{L1} = Pipe 7 - Node 10 and x^{L2} = Pipe 3 - Node 10, respectively. In both pipes, the pipe flow rates Q_{P0} are around 52% of the network flow rate Q_0, and the leak sizes are set to 30% of respective flow rate (i.e., Q_{P0}^{L1} = 30% Q_{P0}, Q_{P0}^{L2} = 30% Q_{P0}) to examine the influence of the leak-sensor distance on the proposed method's performance. To explore the impact of pipe flow rate and leak size on the applicability of the proposed method, Case N3 is implemented. In this case, the leak location is x^{L3} = Pipe 9 - Node 22, with the pipe flow rate accounting for around 10% of the total flow rate, and the leak size Q_{P0}^{L3} = 25% Q_{P0}. The transient event is initiated by a rapid closure of the downstream valve, and the sampling duration is set to be 1 s (about 1 wave period) to ensure the wave propagation from all network components is captured.

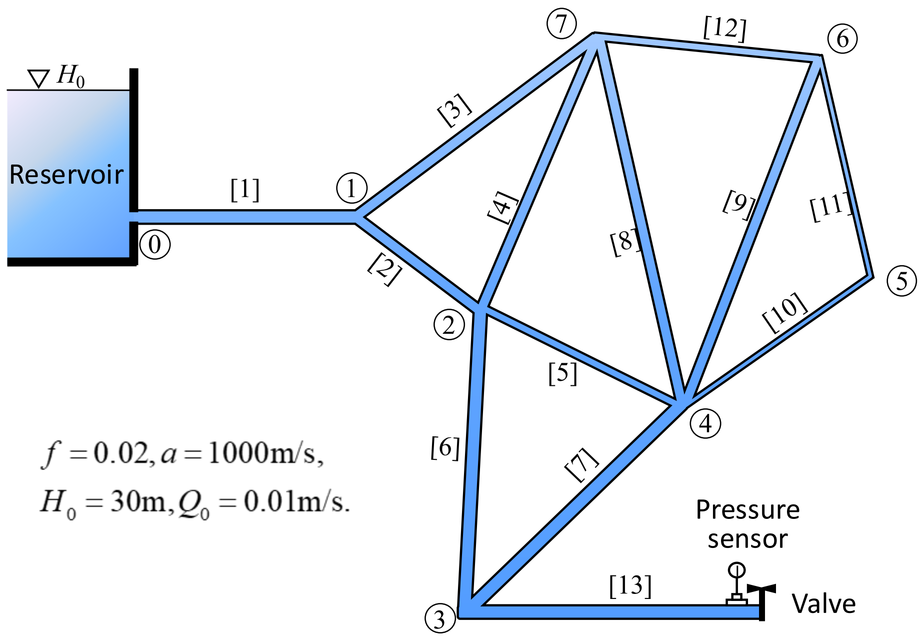

Figure 5.2 Schematic and basic settings for the pipe network

Table 5.1 Length and diameter for each pipe section

Pipe No.	1	2	3	4	5	6	7	8	9	10	11	12	13
L (m)	30	20	40	40	30	40	40	50	50	30	30	30	40
D (m)	0.25	0.20	0.20	0.20	0.15	0.25	0.25	0.20	0.20	0.10	0.10	0.15	0.25

Table 5.2 Leak parameter settings for the three cases

Case No.	H_0 (m)	Q_0 (m/s)	f	a (m/s)	x^L (pipe)	x^L (node)	Q^L_{P0}/Q_{P0} (%)
N1	30	0.01	0.02	1000	7	10	30
N2					3	10	30
N3					9	22	25

5.3 Detection results

In Case N1, the leak is located close to the transient wave source (i.e., on Pipe no. 7). The transient head responses for both intact and leaky pipe networks are plotted in Figure 5.3, and their difference refers to the leak-induced transient wave $\Delta\mathbf{h}$. Applying the proposed single-leak detection method, the objective function B^2 is obtained and plotted in Figure 5.4(a) for leak localization. The global maximum of B^2 coincides with the actual leak location (red dashed line), indicating successful leak localization. With this estimated leak location, the leak size is further evaluated. The result is 29.14% of Q_{P0}, corresponding to an error of 2.9% from the real leak size. This accuracy falls within an acceptable range for a transient-based detection method, confirming the effectiveness of the proposed approach in this case.

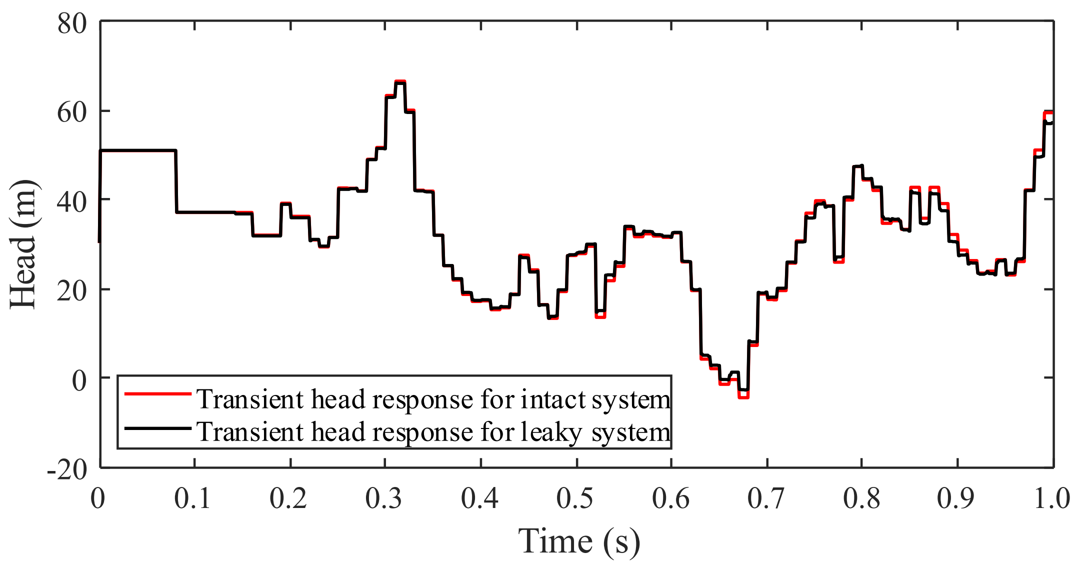

Figure 5.3 Transient head response for intact and leaky pipe networks (Case N1)

The leak in Case N2 is placed on Pipe no. 3. Similarly, the obtained B^2 is plotted in Figure 5.4(b), where its global maximum coincides with the actual leak location in a yellow dashed line. The estimated leak size is 29.33% of Pipe 3's flow rate, with an error of 2.2% from the actual leak size. Comparing the results of Case N1 and Case N2, it can be observed that the proposed method achieves accurate localization regardless of the distance between the leak and the pressure sensor. The influence of measurement distance on size estimation is minimal, confirming the method's applicability across the entire pipe network.

In Case N3, the B^2 is plotted in Figure 5.4(c). Here, the leak is accurately localized, and its size is determined to be 24.89% of the pipe flow rate, deviating by 0.44% from the real size. These results further demonstrate the robustness and accuracy of the proposed method under different network flow rate conditions.

The application results of the three case studies demonstrate clearly the effectiveness and precision of the proposed two-stage method for leak localization in pipe networks under different scenarios in the time domain. Additionally, the method achieved high accuracy in estimating leak sizes, with errors below 1%, highlighting its exceptional capability in leak detection.

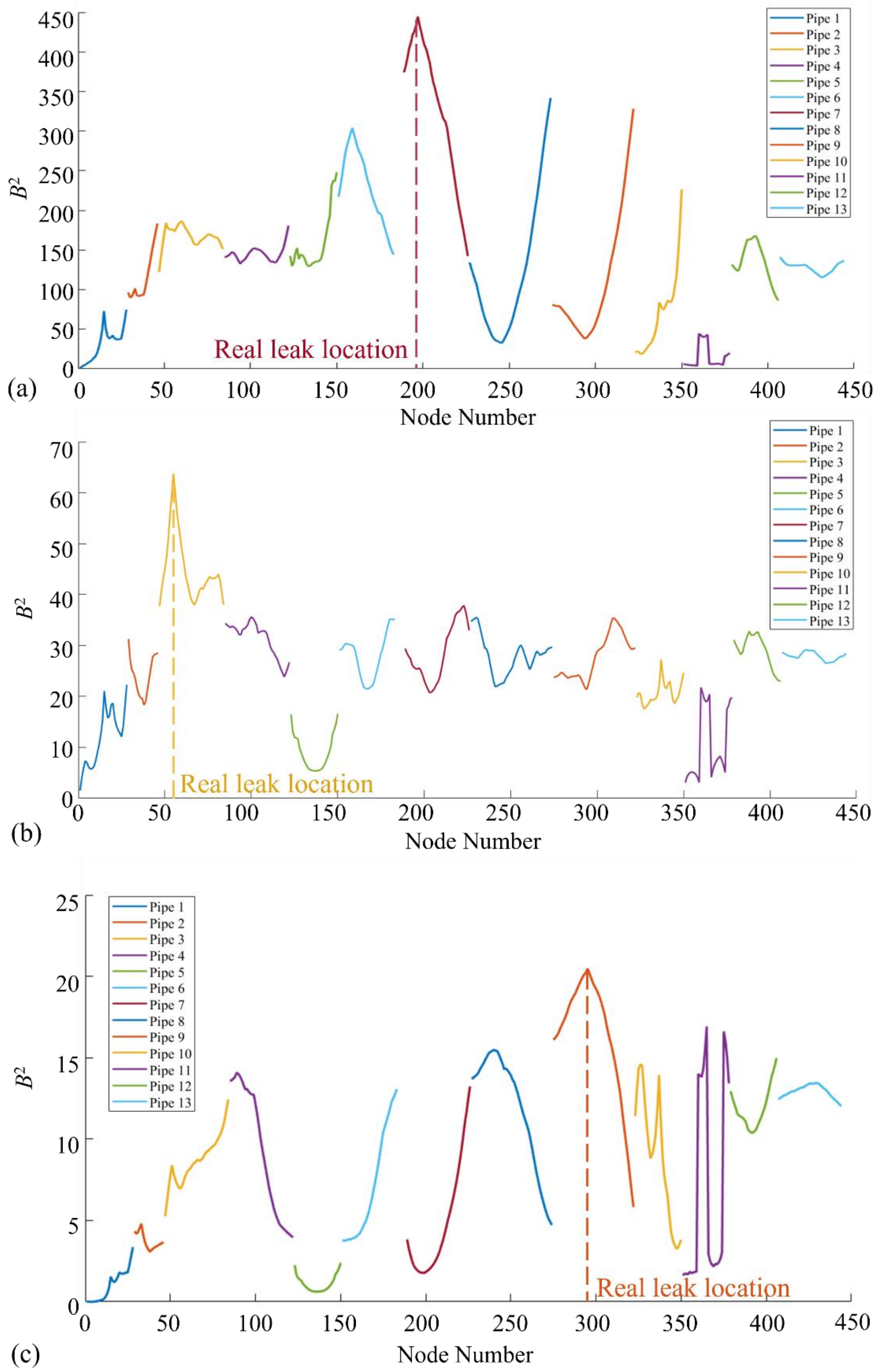

Figure 5.4 Objective function for leak location estimation of: (a) Case N1; (b) Case N2; (c) Case N3

5.4 Leak detection under different noise levels

To assess the robustness of the proposed method, Gaussian white noises are introduced to the transient heads of the above cases for leak detection. Seven different zero-mean Gaussian white noises are added to each leak-induced transient signal $\Delta\mathbf{h}$, and the signal-to-noise ratios (SNRs) of noise relative to $\Delta\mathbf{h}$ range from 20 dB to -10 dB. As illustrated in Figure 5.5, representative noisy signals at three different SNRs (10 dB, 0 dB, and -10 dB) are presented using the $\Delta\mathbf{h}$ from Case N1 as a demonstration. To ensure the reliability of the results, the process of noise addition and leak detection was repeated 200 times for each noise. This rigorous repetition helps to account for any potential variations and provides a more robust evaluation of the method's performance under different noise conditions.

Following the procedures of the developed two-stage method, the average localization errors with respect to different SNRs in the three cases are plotted in Figure 5.6, and the corresponding average leak size estimation errors are listed in Table 5.3. It is evident from Figure 5.6 that the new two-stage detection method performed with excellent accuracy on leak localization with errors not exceeding 0.5 m. Notably, in cases where the SNRs are higher than 0dB, the estimation results precisely match the real leak location, exhibiting a high level of accuracy. Furthermore, under challenging noise disturbance (i.e., SNR = -10dB and -5dB), the standard deviations remain within 1 m, demonstrating strong robustness and applicability of the proposed method. By comparing the localization errors in Figure

5.6, it is evident that the localization accuracy is sensitive to the amplitude difference between the main lobe and side lobes (shown in the sub-plots in Figure 5.4), instead of the absolute amplitude. The larger the difference between the true main lobe and side lobes, the easier it is to localize the true leak under noise. Note that some of the leak localization errors in Figure 5.6 are recorded as 0 because the leaks are assumed to be precisely at preset discrete points identified as potential leak locations during the MOC simulation. However, in practical applications, due to complex pipe connections, modeling errors, and environmental noises, achieving perfect alignment of leaks with the discrete points is highly unlikely. As a result, the 0 error values in Figure 5.6 cannot accurately reflect the true accuracy of leak detection in real-world cases. The leak size estimation results in Table 5.3 show consistency of low errors in all three cases, regardless of the noise level. It is worth mentioning that these results demonstrate strong resemblance to the noise-free cases in the 5-loop network, highlighting the stability of leak size calculation results, once again proving the proposed method's robustness. Overall, the three case studies indicate that, under controlled conditions, the method can reliably extract leak information even when signals are partially corrupted. In practical applications, measurement noise is typically lower than the extreme scenarios tested here and can be further reduced through signal processing. These findings suggest that the method's observed noise resilience supports its potential applicability in real-world pipeline monitoring. Furthermore, monitoring noise levels in operational systems can help determine when the method is likely to provide reliable leak localization, guiding both measurement and preprocessing strategies.

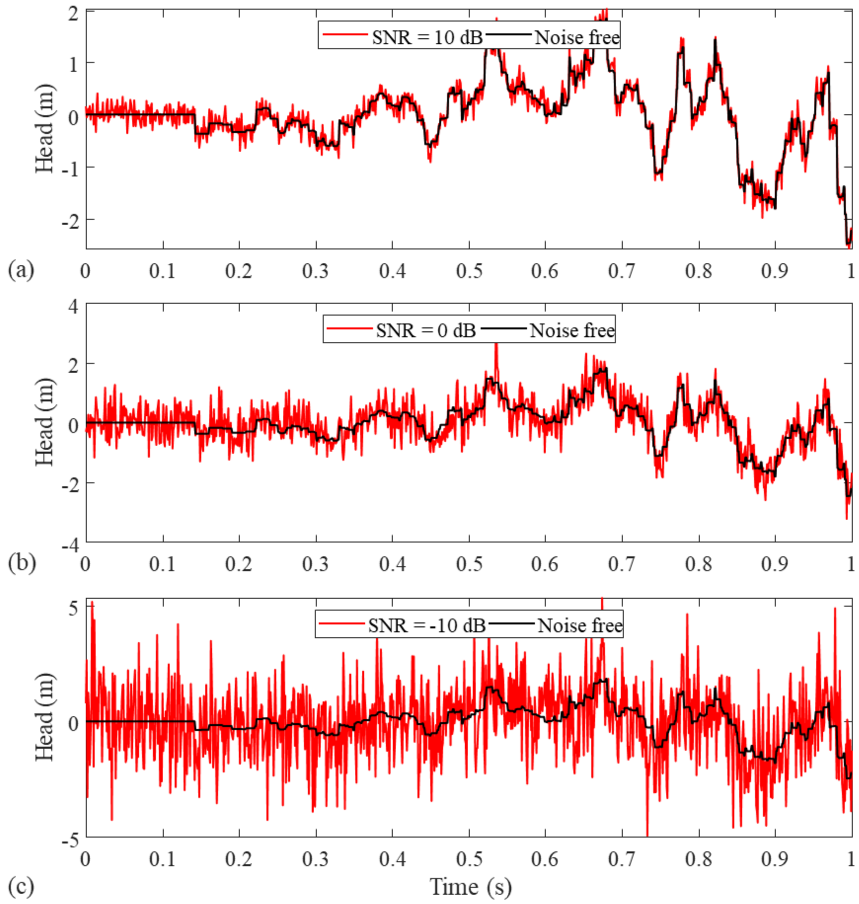

Figure 5.5 Leak-induced transient wave signals for Case N1 with different SNRs: (a) 10 dB; (b) 0 dB; and (c) -10 dB

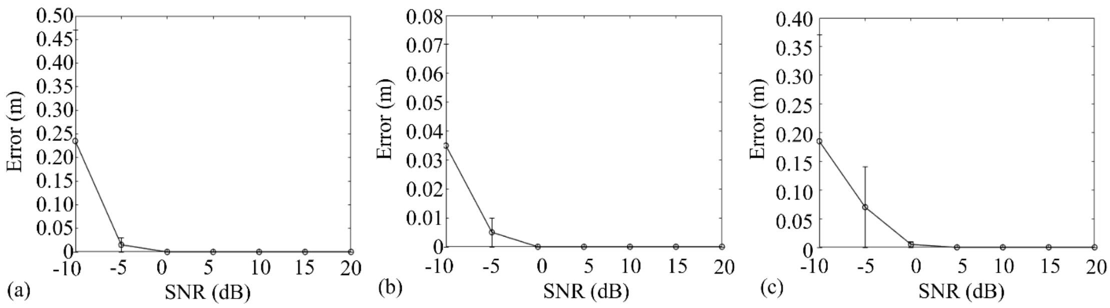

Figure 5.6 Leak localization error with different SNRs in: (a). Case N1; (b). Case N2; (c). Case N3

Table 5.3 Leak size estimation error with different SNRs in three cases

SNR (dB)	-10	-5	0	5	10	15	20
Case N1	1.17%	0.36%	0.04%	0.19%	0.18%	0.12%	0.11%
Case N2	0.36%	0.13%	0.20%	0.05%	0.05%	0.07%	0.07%
Case N3	0.68%	0.58%	0.41%	0.36%	0.20%	0.23%	0.28%

5.5 Sensitivity analysis for leak size estimation

To evaluate the robustness of the objective function's derivative with respect to leak size in the water supply pipe network, a sensitivity analysis of the derived function G(xL) is carried out for Cases N1 and N2. In both cases, four initial guesses for leak sizes, Q_{P0}^{L} = 5%, 10%, 20%, and 30% Q_{P0}, with specified leak locations, were applied to MOC to compute G(xL), with the leak locations held constant. The resulting functions, namely F1 to F4, for both cases, are plotted in Figure 5.7. It can be observed that the four G(xL) curves demonstrate minimal divergence in both sub-figures, indicating a high degree of overlap. For Case N1 (Figure 5.7(a)), the mean square errors (MSEs) of F1, F2, and F3 to F4 (derived from the real leak location and measured data) are 0.056, 0.034, and 0.008, respectively. Similarly, for Case N2 (Figure 5.7(b)), the MSEs of the first three functions to F4 range between 0.001 and 0.008. The results indicate strong consistency of the G(xL)s with different leak size initial guesses in both cases. It clarifies that the derivative of the objective function with respect to leak size aligns well with measured data, thereby illustrating its robustness for both leak location and size estimation, regardless of the initial guess of leak size.

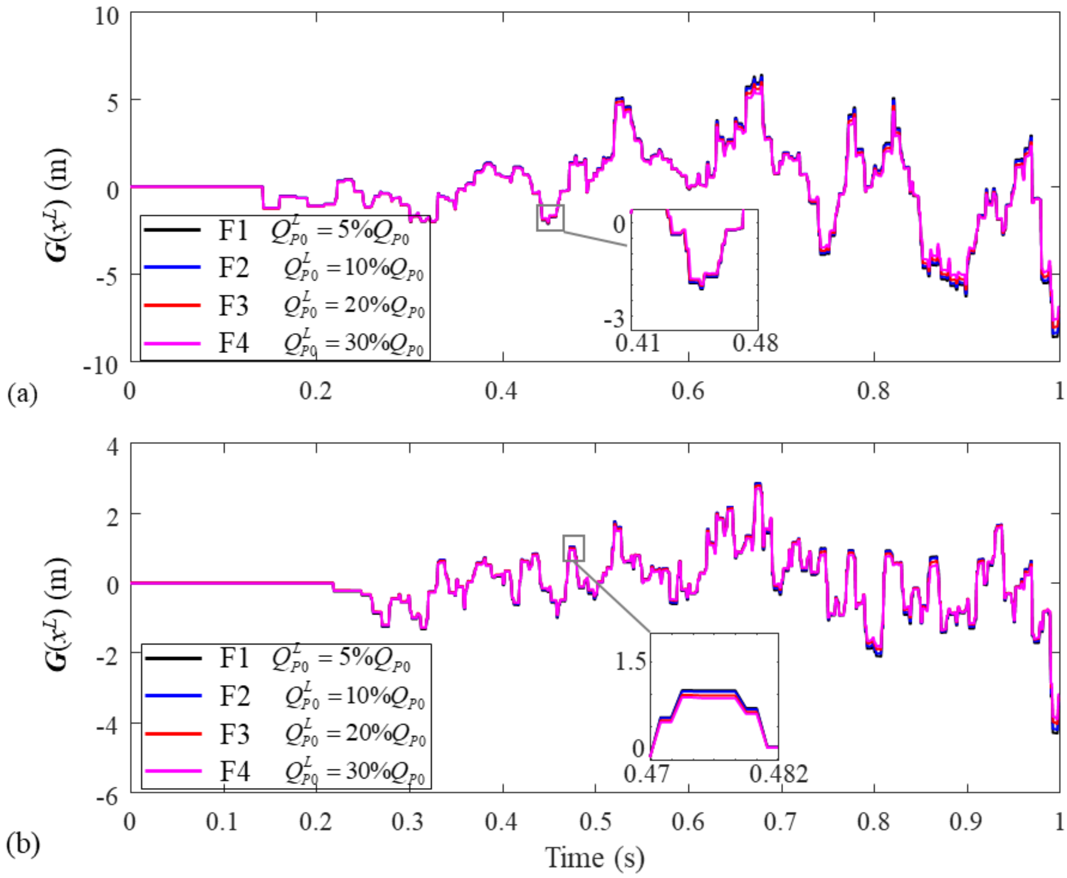

Figure 5.7 Sensitivity analysis of $\boldsymbol{G}(x^L)$ function regarding different leak size guesses: (a) Case N1; (b) Case N2

5.6 Practical implementation and discussion

Based on the above numerical and experimental applications, the proposed time domain leak detection method in this study has achieved a high accuracy for leak detection in multiple-pipe systems. This method significantly improves the detection efficiency of current time-domain full-waveform inversion transient methods, since it simplifies the original two-dimensional optimization problem into a two-stage one-dimensional process, thereby reducing the computational costs. Specifically, taking Case N1 from the above applications of pipe networks as an example, the leak location and size estimation is performed by a two-dimensional enumeration and the proposed method on MATLAB and on the same computer device for fair comparison. As a result, both methods could find the leak parameters (location and size) with good/acceptable accuracy. However, for this simple test case, the conventional two-dimensional approach takes about 48.98 seconds to complete detection, while the new method takes around 2.98 s only. That is, the proposed two-stage leak detection method in this study is approximately 15 times faster than the conventional one, demonstrating its superiority and efficiency improvement for leak detection in complex pipe networks. Further inspection of the detailed detection processes implies that the efficiency improvement of the new method will be dramatically increased with the complexity of the pipe network configurations (e.g., pipe numbers and scales), contributing to extending the existing methods to more realistic and complex pipe systems. For instance, for a large-scale water distribution system composed of hundreds of pipes (e.g., the total number of pipelines in the system is denoted by M), the computational cost of the conventional two-dimensional method in time domain is in an order of $M \times M$, which is very time-consuming, while that of the new method is about $1 \times M$ only, leading to dramatic reduction of computation time. Therefore, the efficiency advantage of this proposed approach becomes more prominent as the pipe network complexity is increased.

Furthermore, the results show that the proposed method maintains high robustness in leak detection and holds substantial superiority in handling noise issues when processing the measured transient signal. Moreover, the proposed method offers notable superiority in its high adaptability of measured transient data when considering the practical application in real network systems compared with frequency domain methods. Specifically, the accurate leak detection in this research is accomplished by the measured transient data from a single pressure transducer at the downstream end of the network system, with insufficiently long and damped signals compared to frequency domain methods. The new approach is capable of providing a flexible and straightforward data collection process, improving the feasibility of the method in pipe networks with different configurations. Additionally, the proposed method demonstrates the adaptability in dealing with inaccessible boundaries, highlighting its applicability in diverse pipe systems. In general, as long as the numerical simulation of the intact pipe network system is sufficiently accurate, the new two-stage leak detection method exhibits exceptional feasibility to pipeline complexity and other complex real-life pipe network situations, indicating its potential in practical implementation. It is also important to note that there are still some restrictions during real applications in a real pipeline system. Due to the presence of noise (aleatoric uncertainty), the transient response caused by minor defects (e.g., with an assumed small leak size) could be easily covered and overlooked in the collected signal data, resulting in inaccurate/invalid detection. On the other hand, epistemic uncertainty (i.e., modeling error) existing in real-life pipe systems is often neglected in numerical models. It includes factors such as unknown pipe branches or elbows, internal blockages or roughness, inaccurate boundary conditions, and pipe material properties. Such uncertainty can lead to inaccuracies in wave speed and viscoelastic parameters, causing detection errors. However, it is challenging to adequately explain or model epistemic uncertainty with one-dimensional transient equations, nor can it be precisely estimated. Nevertheless, it can be evaluated by regular monitoring of the pipe system before the leak happens (Wang et al., 2020). This information can then be incorporated with the transient method to achieve more promising leak detection results.

5.7 Summary and Conclusion

This chapter presents the numerical application of single-leak detection in pipe network systems using an alternative two-stage time-domain algorithm. In this approach, the leak-induced transient response is linearized with respect to the leak size, thereby reducing the traditional two-dimensional optimization problem to a one-dimensional parameter estimation problem. This formulation significantly simplifies the inversion process and improves computational efficiency.

The proposed method is evaluated through numerical case studies and sensitivity analyses on pipe network systems of increasing complexity. The results show that, provided the numerical model adequately represents the physical pipe network, the method can accurately localize single leaks, with mean localization errors remaining below 0.25m across all tested scenarios. The sensitivity analysis further indicates that the estimation accuracy is stable under moderate modeling uncertainties and measurement noise. In comparison with the conventional inverse transient analysis (ITA) method, the proposed approach achieves substantially higher computational efficiency. For the tested network configurations, the average computation time showed a speed-up of approximately 15 times. Moreover, the efficiency gain increases with network size and topological complexity, highlighting the scalability of the proposed method for large pipe networks.

The robustness of the method is further demonstrated through successful leak detection under varying noise levels and parameter perturbations. Overall, the numerical results confirm the applicability, accuracy, efficiency, and robustness of the proposed two-stage algorithm for single-leak detection in complex pipe network systems.

CHAPTER 6 SENSITIVITY ANALYSIS FOR PARAMETER SEPARATION LEAK LOCALIZATION

6.1 Introduction

In a pressurized pipe system, transient waves are easily triggered by sudden changes in boundary conditions and valve operations. Careful analysis and utilization of these transient waves are essential for protecting pipeline safety and the system's normal operation. During the development of the transient wave model and/or a new failure detection method for water supply pipeline systems, various parameters showed up in the governing equation development, such as pipe internal diameter, friction, wave speed, and boundary conditions, which are generally considered deterministic and assumed to remain consistent. However, in real-world situations, the variation and uncertainties of these parameters could come from natural factors such as aging infrastructure, pipe corrosion, and environmental changes, as well as human activities, such as valve operations and measurement errors. These changes affect transient wave signal capture and analysis, introducing uncertainties and risk to accurate pipe detection.

While detecting experimental or real-world pipe systems, the gap between the numerical model prediction and the field measurement can be narrowed by integrating the newly developed model that targets key parameters including geometric parameters (e.g., pipe wall thickness and internal diameter), pipe material parameters (e.g., viscoelasticity and friction), boundary, and wave speed. However, the uncertainty associated with these parameters also contributes to the modeling inaccuracy. For instance, uncertainty of friction may lead to rapid/slow damping in the pressure head and energy of the transient wave during its propagation. The uncertainty of wave speed relates to the propagation time and period. Human activity uncertainties, such as the discrepancy between the valve operation curve and the designed curve may result in variations in the pressure peak. Therefore, it is essential to understand the extent of these uncertainties while dealing with practical applications and developing a robust transient model and analysis framework.

Currently, the performance of the newly developed parameter separation method and the incorporation of the iterative beamforming method from the previous chapters have been tested under various conditions, including different levels of noise (Chapters 4 and 5), super-resolution of adjacent leaks (Chapter 4), complex pipe network configurations (Chapter 5), and practical applications on lab-scale RPV system (Chapters 4). Through all these tests, the new approach has demonstrated high robustness and efficiency in numerical and experimental studies, while assuming deterministic system parameters. To enhance the in-depth understanding of this method and help further improve the method's application in real-world piping systems, a sensitivity analysis and reliability evaluation of the new method with explicit consideration of various uncertainties across different leak scenarios are crucial for its future development.

This study first discussed the potential effect of uncertainties on transient wave propagation and leak detection, followed by the performance evaluation of the new method for leak localization concerning four key uncertainties in single-leak and two-leak scenarios, respectively. The Monte Carlo Simulation (MCS) is adopted in this study as a robust tool for probabilistic modeling of uncertainties. The leak localization results and detection errors for each leaking case are analyzed, and the conclusions are drawn.

6.2 Uncertainty Effect on Transient Wave and Leak Detection

Various properties of uncertainties have been studied to determine the influence of uncertainties on transient wave propagation along the pipeline system. The impacts focus on transient properties such as wave speed, damping, and transmission. The wave speed of a transient is largely dependent on pipe viscoelasticity and pipe wall thickness. The uncertainty of wave speed can be triggered by these uncertainty features, thereby affecting the propagation process and periods of the transient wave. The transient damping is primarily influenced by the friction and pipe wall thickness, which can affect the damping effect, enhancing or weakening it, thereby affecting the attenuation rate of the wave, and causing the discrepancy between transient application and model prediction. Furthermore, for complex pipe network systems, unknown branches and valve operations could lead to extra reflection and transmission of the transient wave, giving uncertainties for wave interpretation and analysis. Previous studies have shown how uncertainties could affect the transient response characteristics and, therefore, the transient-based detection.

By taking uncertainties into consideration during the transient study, the detection challenges of an unknown pipeline system can be more effectively confronted based on the captured transient signal, giving more flexibility while analyzing the signal and understanding the system. Moreover, for a new detection approach, considering uncertainties and applying performance evaluation can provide valuable information about the new approach for an existing pipe system, enhancing the understanding of the method.

In this chapter, different system parameters are considered uncertainties and are applied for leak detection in various cases, from common to extreme. The performance of the parameter separation method, incorporating iterative beamforming, is evaluated, and its stability and robustness are examined. To study the impact of individual uncertainties on detection effectiveness more precisely, the leak number N is assumed to be a known parameter in the testing system.

6.3 Methodology

6.3.1 Parameter separation method and iterative beamforming

6.3.1.1 Time domain parameter separation method for single leak detection

The time domain parameter separation method is used for single leak detection. It employs a factorized time domain transient model and separates the coupled leak size and location, decomposing the two-dimensional optimization problem into two one-dimensional estimation issues. The leak localization is first estimated with Eq. (6.1). For any estimated leak location $\hat{x}^L$, its corresponding leak size is calculated with Eq. (6.2):

$$\left\{\hat{x}^L\right\} = \arg\max_{x^L}\left(\Delta\mathbf{h}^T\mathcal{G}(x^L)\frac{\mathcal{G}(x^L)^T\Delta\mathbf{h}}{\mathcal{G}(x^L)^T\mathcal{G}(x^L)}\right) = \arg\max_{x^L}(B^2) \tag{6.1}$$

$$\hat{s}^L = \frac{\mathcal{G}(x^L)^T \Delta\mathbf{h}}{\mathcal{G}(x^L)^T \mathcal{G}(x^L)} \tag{6.2}$$

6.3.1.2 Iterative beamforming for multiple leak detection

For multiple leak detection, iterative beamforming incorporating the parameter separation method breaks down the optimization problem for N leaks into $2N$ sequential one-dimensional sub-problems, thereby resolving the computationally cumbersome and non-convex issue. In each iteration, given the leak number N and the optimal decomposed wave signal $\Delta\hat{\mathbf{h}}_j^{L_n}$ after the j-th iteration, the conditional expectation is derived in Eq. (6.3).

$$\mathbb{E}\left[\ell(\mathbf{\Phi} \mid \Delta\mathbf{h}^L) \mid \Delta\mathbf{h}, \mathbf{\Phi}_{j-1}\right] = -\sum_{n=1}^{N} \left\| \Delta\mathbf{h}_j^{L_n} - s^{L_n} \mathcal{G}(x^{L_n}) \right\|_2^2 + c \tag{6.3}$$

To maximize the conditional expectation, Eqs. (6.1) and (6.2) are applied to each decomposed single leak-related transient wave signal, and the locations and sizes of each leak are estimated.

6.3.2 MCS-Based Uncertainty Analysis

The Monte Carlo Simulation (MCS) is a type of simulation that relies on repeated random sampling and statistical analysis to compute the results (Raychaudhuri, 2008). It is widely used for uncertainty and reliability analysis in hydraulic and hydrological engineering. In this study, the MCS method is implemented to generate random samples within the specified value range and distribution of the key uncertainties. A total of 10,000 samples are produced and input into the detection procedure for each uncertainty, followed by the output of leak detection results for the numerical reservoir-pipe-valve (RPV) system. The flowchart of MCS and leak detection is shown in Figure 6.1.

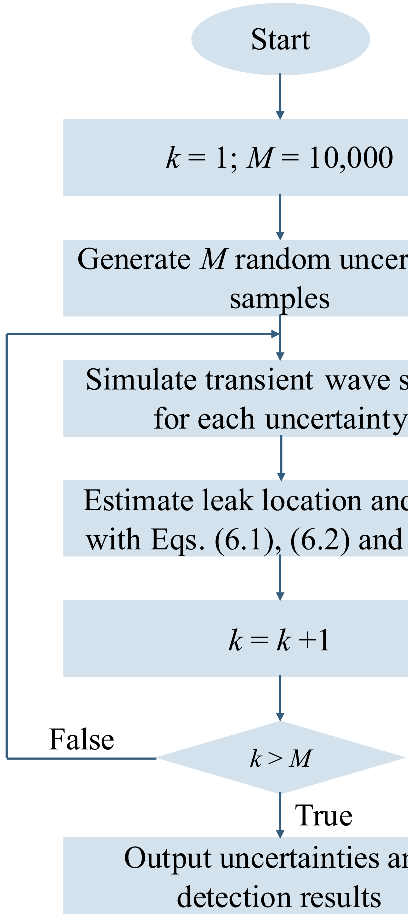

Figure 6.1. Flowchart of MCS-based Uncertainty Analysis

6.4 Numerical Test System and Uncertainties Setup

In this part, the numerical reservoir-pipe-valve (RPV) system designed for uncertainty investigation is given. The RPV system includes an upstream reservoir with a fixed water head (H_0 = 80 m), a pipe, and a downstream valve that generates transient wave perturbations. A pressure sensor is placed near the valve to capture the wave signals. Two types of leak cases are tested: (1) single leak cases with leak location x^L and size s^L, and (2) double-leak cases with two independent leaks placed at x^{L1} and x^{L2} with size s^{L1} and s^{L2}, respectively. The configuration and basic parameters of the numerical RPV system are shown in Figure 6.2, where the pipe flow rate Q_0 = 0.1 m^3/s, pipe length L = 200m, pipe internal diameter D = 0.5m, transient wave speed a = 1000m/s, and steady friction f = 0.02. Pulse-shaped transient waves are triggered by rapid valve perturbation in 20 ms, with the valve opening degree changing from 100% to 80% and back to 100%. The four key parameters, a, f, L, and D, are subjected to uncertainty analysis through Monte Carlo sampling for 10,000 numbers each to ensure static robustness. Their variations and distributions are outlined in Table 6.1 below.

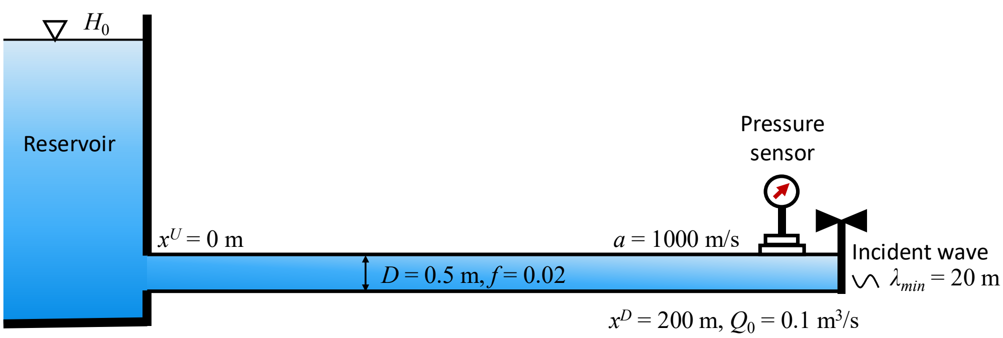

Figure 6.2. Configuration and parameter setting of the numerical test system

Table 6.1. Variations and distributions of the four uncertainties

Uncertainty	μ_U	σ_U	Range	Distribution
a (m/s)	982.07	49.26	[800, 1200]	Lognormal
f	0.0366	00094	[0.01, 0.05]	Triangular
D (m)	0.5	0.0289	[0.9D, 1.1D]	Uniform
L (m)	200	11.55	[0.9L, 1.1L]	Uniform

In Table 6.1, μ_U and σ_U denote the mean value and standard deviation of the uncertainties, respectively. The subscript U for uncertainty can be replaced by specific parameters. The four uncertainties follow lognormal, triangular, and uniform distributions as shown in the table. For parameters D and L, their mean values, μ_L and μ_D, are equal to their expected values.

The leak detection accuracy of the proposed method is evaluated for the four uncertainties, and sensitivity analysis is conducted through uncertainty-error joint distribution investigation and correlation coefficients to quantify the influence of parameters on the transient response. This numerical test setup provides a robust framework for performance evaluation of the parameter separation leak detection method under realistic operational uncertainties.

6.5 Single Leak localization

6.5.1 Single leak cases setup

Five single leak cases, listed in Table 6.2, are designed to examine the proposed method's performance under uncertainties for both general and extreme situations. Cases S1 and S2 mimic the normal leaking cases that could occur during pipe operation, while Case S3 simulates a small leak situation. The remaining two cases imitate the instances where the leaks are close to the upstream and downstream boundaries. Notably, the leak is located at 175m from upstream in Case S5 to coordinate the distribution range of L uncertainty.

Table 6.2. Single leak cases setup

Case No.	x^L (m)	s^L (% of Q_0)
S1	50	10
S2	160	15
S3	50	2
S4	8	10
S5	188 or 175 (for L cases)	10

6.5.2 Leak localization results

Following the MCS uncertainty analysis flowchart in Figure 6.1, the single leak localization was conducted for the four uncertainties mentioned in the above cases. The uncertainties of successful detection results are listed in Table 6.3, which includes the overall leak localization mean value μ, standard deviation σ, and the distribution of uncertainties for the successful cases, with μ_{Us} and σ_{Us} representing their mean and standard deviation. As noted, subscript U can be replaced by specific uncertainties. It can be observed from the table that under different uncertainties, the performance of the new approach varies.

For the wave speed uncertainty, the detection results are plotted in Figure 6.3. It can be observed that the detection results exhibit a similar V-shaped trend across the five sub-figures, with most results occurring within the first 50m of the pipe, regardless of the targeted/actual leak locations. This situation can be attributed to the relationship between wave speed and transient propagation, as it directly determines the temporal periodicity of transient waves (i.e., $T = 4L/a$). When a is treated as a source of uncertainty, the detected leak location depends on the signal period rather than the true leak locations. Accurate detection results occur when the assumed value closely matches μ_a, which is also the model's designed value. As demonstrated in Table 6.3, the overall successful detection results for wave speed uncertainty are notably low, with less than 500 out of 10,000 tests, resulting in a success rate of under 5%. The fixed detection results from the wave speed setting are excluded from the analysis to prevent misleading statistical outcomes. Among the five cases, case S2 performs the best due to its largest leak size, which improves the detectability of the leak. In contrast, Case S3 performs the worst. Although Case S4 demonstrates a high success rate in Figure 6.3(d) as its location is in the upstream of the pipe system, which aligns well with the fixed localization result, its actual performance is comparable to Case S3, as indicated in Table 6.3.

The leak detection results for steady friction uncertainty demonstrate 100% accuracy for all four cases, except for Case S3, where 66.93% of the tests achieved accurate leak localization, due to the precision of the steady friction modeling. The failure performance is concentrated on both sides of the f range (see Figure 6.4(c)), where the overestimation of f leads to transient signal amplitude overprediction and, consequently, detection failure, while overestimated f values result in over-damping of the transient signal and the small leak signature being obscured. The successful detection for Case S3 shows a left-skewed friction distribution with μ_{fs} = 0.0356 and σ_{fs} = 0.0062, as given in Table 6.3. This indicates that the proposed method is more reliable with lower friction coefficients when dealing with small leak sizes.

The detection results for diameter uncertainty are shown in Figure 6.5. It is evident that, despite the number of successful tests, the corresponding D values of successful detections are symmetrically distributed with μ_D (= 0.5) at the center. The statistical results in Table 6.3 also support this observation, indicating the method's balanced performance across different pipe diameters. Nevertheless, it can be observed that Cases S2 and S3 display the highest and lowest success rates, respectively (i.e., 33.87% and 4.95%), while the other cases show similar success rates, ranging from 22% to 25%. The results demonstrate consistent robustness of the method regarding diameter and other uncertainties. Case S3's low success rate reveals the challenges of the proposed method in detecting small leaks when involving various uncertain parameters.

The detection results of length uncertainty in Figure 6.6 show a V-shaped distribution, similar to that of the wave speed uncertainty. This similarity arises from the direct influence of L on the temporal periodicity of transient waves, leading to a relatively consistent set of outcomes with a step-like transition. Analysis for Table 6.3 indicates that all cases present 250 successful tests, with L concentrated around 200.5m. Nevertheless, Case S4 deviates from this trend in Figure 6.6(d), due to the overlap between fixed localization results and real leak location.

To quantitatively analyze the statistical results of successful tests presented in Table 6.3 and to demonstrate the reliability and resilience of the method against the four uncertainties, the success-uncertainty ratio S is introduced here with the following definition:

$$S(\%) = \frac{\delta_{Us}}{\delta_U} \times 100 \tag{6.4}$$

in which δ is the coefficient of variation (COV) that is used to evaluate the variability range of each parameter, and

$$\delta = \frac{\sigma}{\mu} \tag{6.5}$$

The calculated results by Eqs. (6.4) and (6.5) are listed in Table 6.4, which further supports the observations regarding different uncertainties in detection accuracy. The results also demonstrate that (1) the proposed method has the highest robustness against changes in steady friction, followed by those in diameter. The inaccuracy in length and wavespeed modeling has significant effects on the method's robustness. (2) The success rates for length and wavespeed cases are similar, with results for L demonstrating high stability, whereas the results for a are influenced by the locations and sizes of leaks. (3) Both leak location and size influence the detection success rate, with size having a greater impact; the detection of small leaks tends to be more vulnerable to uncertainties.

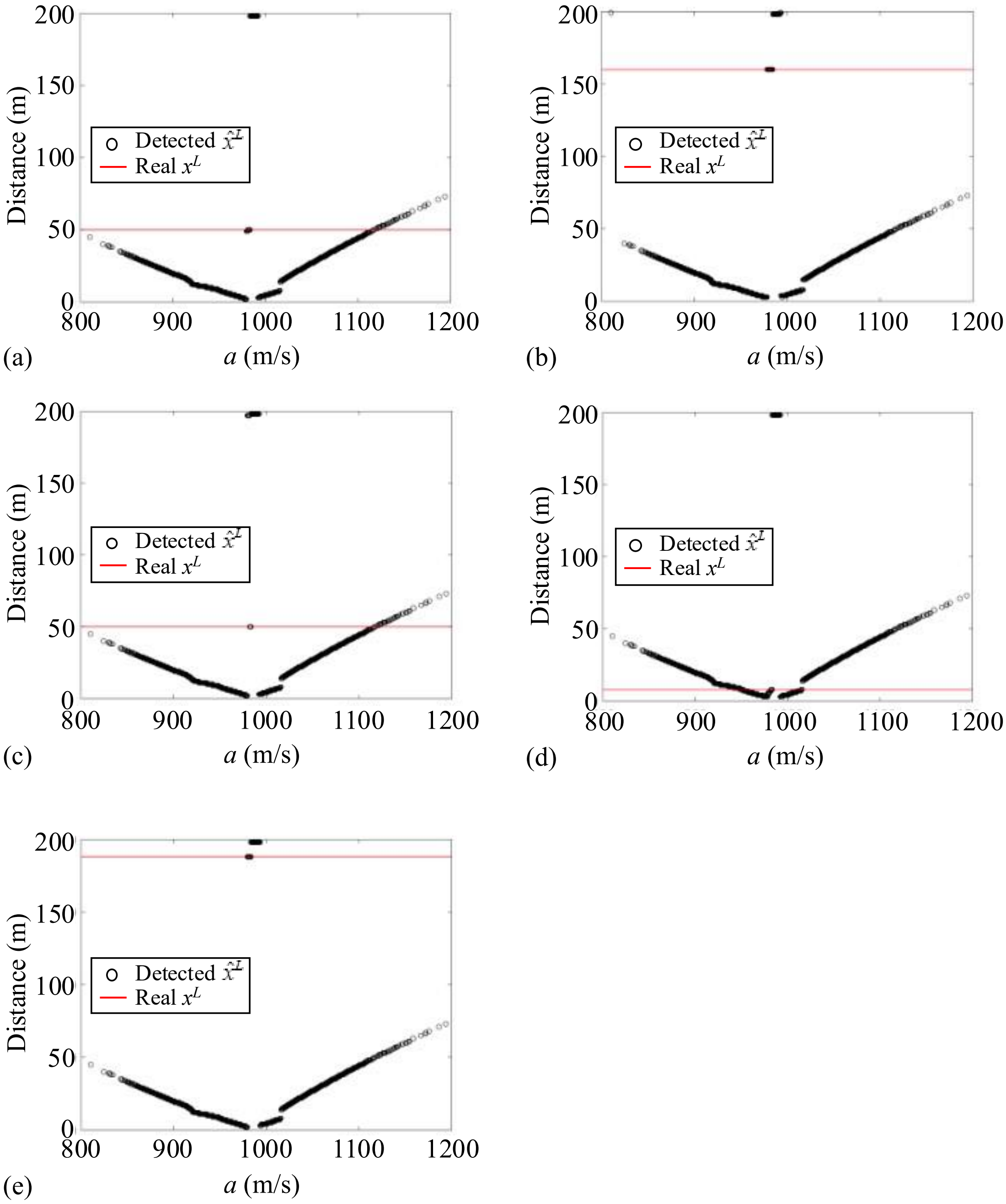

Figure 6.3. Leak localization results for wavespeed uncertainty: (a) Case S1; (b) Case S2; (c) Case S3; (d) Case S4; (e) Case S5

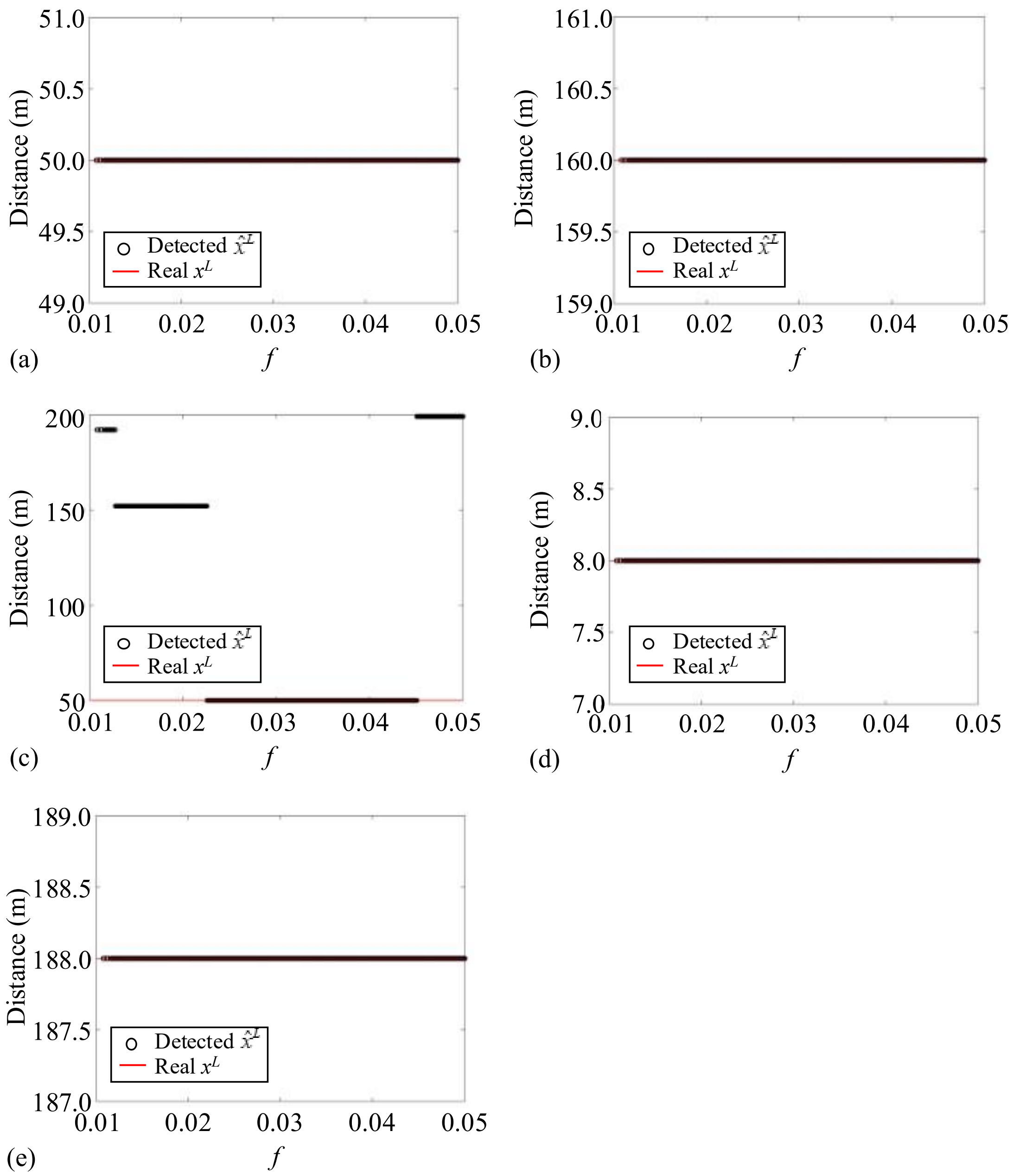

Figure 6.4. Leak localization results for steady friction uncertainty: (a) Case S1; (b) Case S2; (c) Case S3; (d) Case S4; (e) Case S5

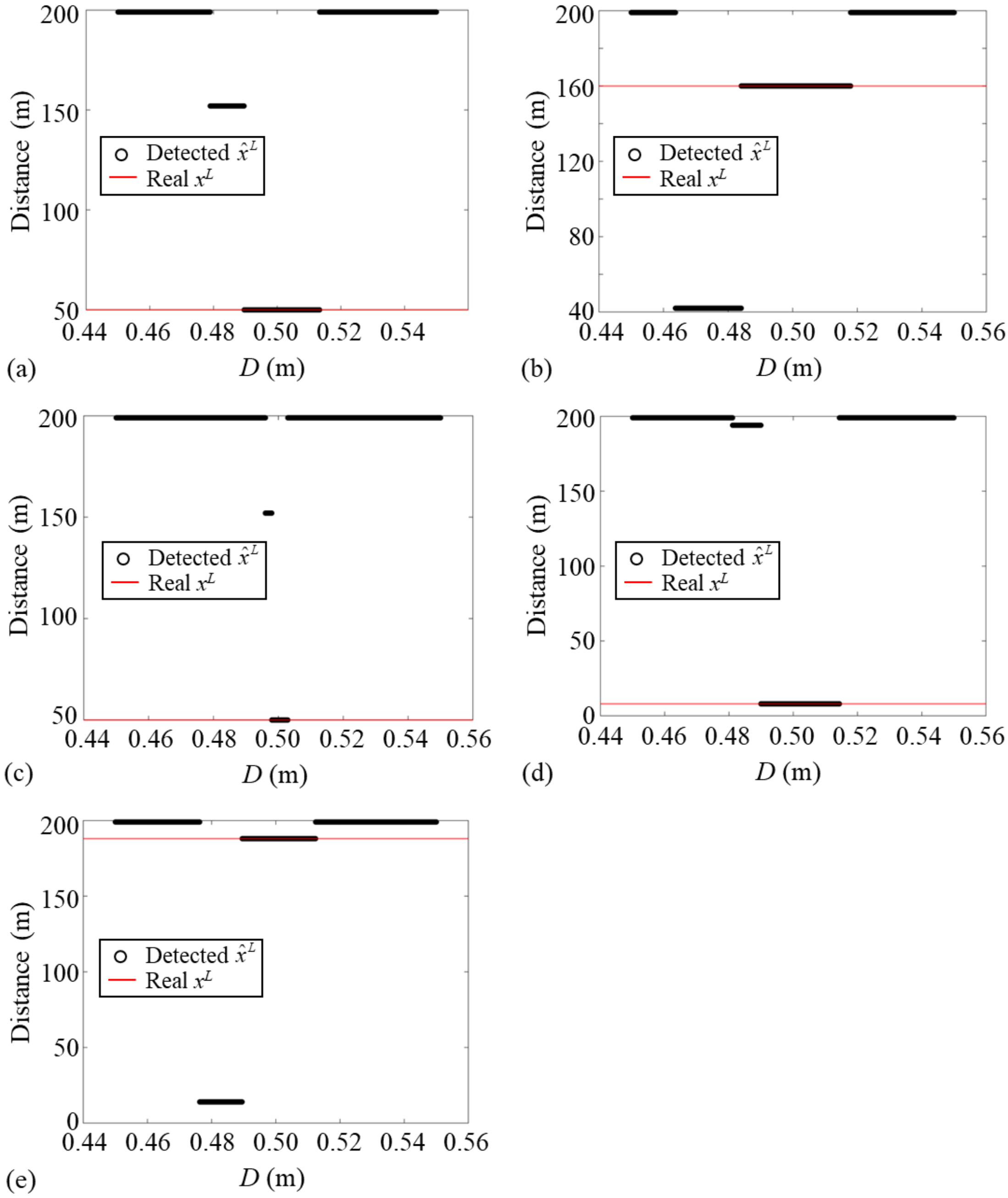

Figure 6.5. Leak localization results for diameter uncertainty: (a) Case S1; (b) Case S2; (c) Case S3; (d) Case S4; (e) Case S5

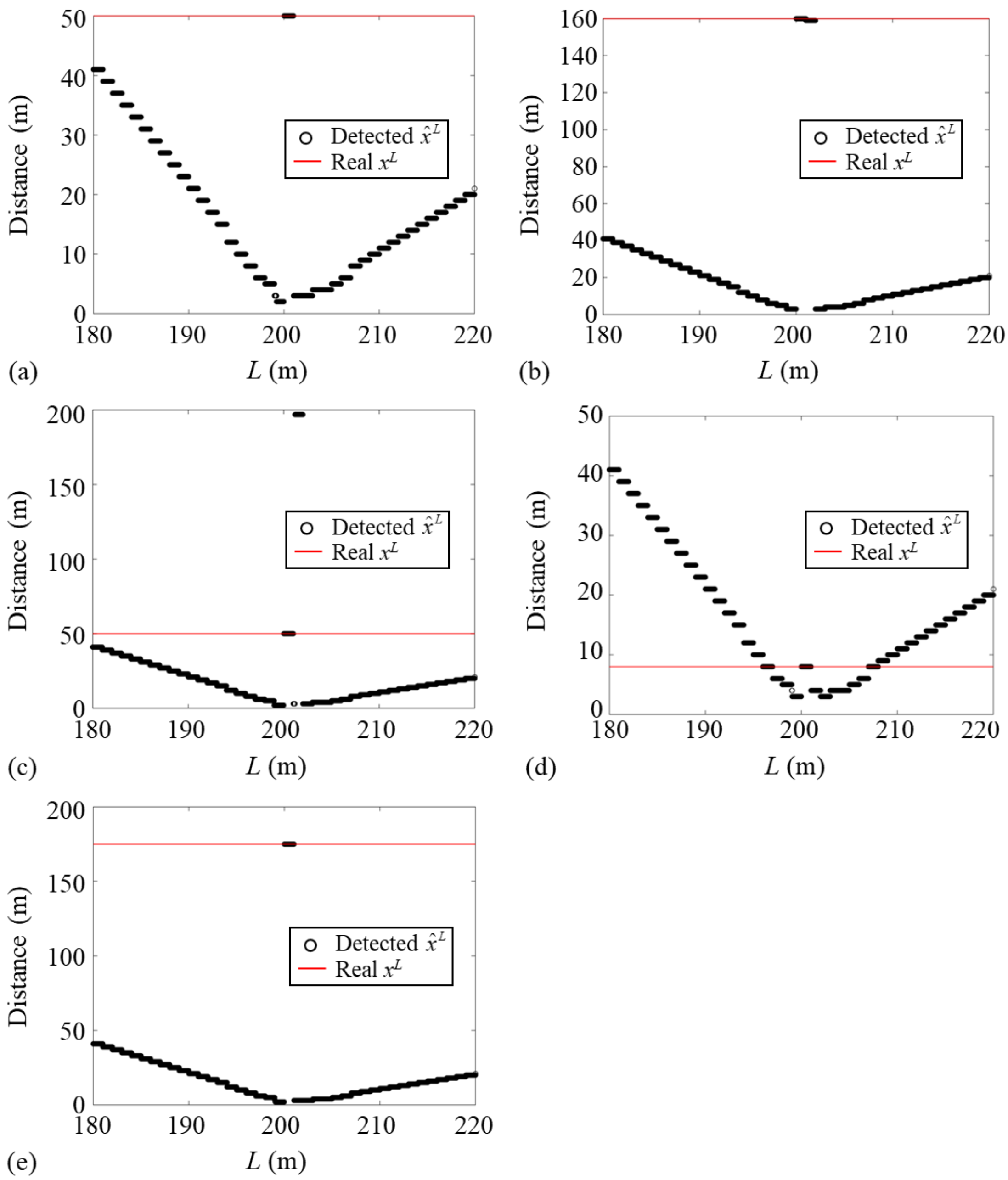

Figure 6.6. Leak localization results for length uncertainty: (a) Case S1; (b) Case S2; (c) Case S3; (d) Case S4; (e) Case S5

Table 6.3 Uncertainty of successful leak localization results

Case No.	Uncertainty											
	a						*f*					
	Total test No.	Total results μ	Total results σ	Success test No.	Success μ_{as}	Success σ_{as}	Total test No.	Total results μ	Total results σ	Success test No.	Success μ_{fs}	Success σ_{fs}
S1	10000	26.86	48.10	193	981.8712	0.7287	10000	50.00	0.00	10000	0.0366	0.0094
S2		33.27	55.85	491	981.2026	1.8760		160.00	0.00	10000	0.0366	0.0094
S3		29.48	53.04	103	982.4744	0.3338		94.68	64.75	6693	0.0356	0.0062
S4		25.71	48.02	103	982.4744	0.3338		8.00	0.00	10000	0.0366	0.0094
S5		32.63	57.22	281	981.2831	1.0797		188.00	0.00	10000	0.0366	0.0094

Case No.	Uncertainty											
	D						*L*					
	Total test No.	Total results μ	Total results σ	Success test No.	Success μ_{Ds}	Success σ_{Ds}	Total test No.	Total results μ	Total results σ	Success test No.	Success μ_{Ls}	Success σ_{Ls}
S1	10000	158.65	62.24	2372	0.5015	0.0068	10000	17.31	11.86	250	200.5001	0.2893
S2		153.79	59.12	3387	0.5010	0.0098		23.98	32.78	250	200.5001	0.2893
S3		190.70	32.77	495	0.5005	0.0014		21.32	28.09	250	200.5001	0.2893
S4		151.88	81.84	2444	0.5022	0.5022		16.30	10.66	250	200.5001	0.2893
S5		171.99	61.89	2288	0.5010	0.0066		20.43	26.94	250	200.5001	0.2893

Table 6.4. Success-uncertainty ratio for all the cases

Case No.	Uncertainty							
	a		*f*		*D*		*L*	
	δ	*S*	δ	*S*	δ	*S*	δ	*S*
S1	0.0007	1.48%	0.2568	100.00%	0.0136	23.46%	0.0014	2.50%
S2	0.0019	3.81%	0.2568	100.00%	0.0196	33.84%	0.0014	2.50%
S3	0.0003	0.68%	0.1742	67.81%	0.0028	4.84%	0.0014	2.50%
S4	0.0003	0.68%	0.2568	100.00%	0.0141	24.46%	0.0014	2.50%
S5	0.0011	2.19%	0.2568	100.00%	0.0132	22.79%	0.0014	2.50%

6.6 Multiple Leak Localization

6.6.1 Multiple leak cases setup

The setups for the four multiple leak cases, used for evaluating the proposed method's performance, are listed in Table 6.5. Among the four cases, Case M1 can be considered the superposition of single leak Cases S1 and S2. Case M2 examines the situation where two leaks of significantly different sizes exist simultaneously. Case M3 combines Cases S4 and S5, where two leaks are near the system boundaries but far away from each other. Case M4, on the other hand, simulates the two leaks that are close together, with their distance being half the minimum incident wavelength, $\lambda_{\min}/2$. Again, special consideration applies to L uncertainty, with the location of the large leak is set at 175m instead of 188m in Case M3.

Table 6.5. Multiple leak cases setup

Case No.	x^{L1} (m)	s^{L1} (% of Q_0)	x^{L2} (m)	s^{L2} (% of Q_0)
M1	160	15	50	10
M2	160	25	50	5
M3	188 or 175 (for L cases)	15	8	10
M4	60	15	50	10

6.6.2 Leak localization results

Based on the MCS uncertainty analysis flowchart shown in Figure 6.1, the two leaks in the four cases were localized and plotted in Figures 6.7-10. The uncertainty parameters related to the successful results are listed in Table 6.6, which excludes the fixed localization results that align with the actual leak locations.

For all cases under wave speed uncertainty, the detected leak locations show V-shaped trends with changes in wave speed with relatively fixed localization results. The detection results for x^{L1} (i.e., large leaks) follow a more regular trend, highly similar to the single leak results in Figure 6.3. In contrast, the results of x^{L2} (i.e., small leaks) appear closer to the downstream boundary of the pipeline more frequently, increasing the risk of under detection. Similarly to the detection results in a single pipe, the detection accuracy here is closely related to the wave speed. Accurate detection results are concentrated in the middle of the V-shape curve, corresponding to a narrow range near μ_a. Quantitative analysis in Table 6.6 indicates that among the 10,000 tests, the numbers of successful tests are less than 400, which is a 4% success rate. Additionally, the proposed method performs better for larger leaks and less effectively for small leaks (see the results of Cases M1 and M2). In Case M3, where leaks are close to the system boundaries, since the transient wave signal is generated using a 20 ms impulse response function, during its propagation, the leak signal may be partially covered or overlapped by the transient signal, especially when there are wave speed modeling inaccuracies, leading to inaccurate detection results. In contrast, in Case M4, when the distance between the two leaks is precisely half the minimum incident wavelength (10m), the detection accuracy is better than that of Case M3, particularly x_{L2} in Case M3, which is 8m from the upstream boundary. These results demonstrate that in addition to the effect of wave speed uncertainty on transient signal period, the relative distance of leaks and leak sizes also affect detection accuracy.

The localization results under steady friction are the best among the four uncertainties. Especially for Cases M1 and M4, all tests are successful, achieving 100% accuracy. This demonstrates the robust performance of the proposed method under f when the leak sizes are relatively comparable. When the leak sizes have a big difference, the method still performs precise localization for both leaks, except when the elevated steady friction causes severe transient signal attenuation, interfering with the detection of small leaks. In Case M3, the identified leak locations are reversed when f is low, as it allows the signal to propagate with low energy loss, increasing the difficulty of distinguishing two nearly symmetrical leaks. However, as f increases, enhanced energy loss and transient signal damping provide additional information to help differentiate and clarify the two leaks.

Under D uncertainty, the leak detection results show strong inconsistencies in Figure 6.9, while the successful tests concentrated around μ_D. Quantitative analysis in Table 6.6 demonstrates that when dealing with D uncertainty, the detection performance of the proposed method is strongly dependent on the leak size. When the leak is the largest (25% flowrate for x_{L1} in Case M2), the success rate is the highest at 72.82%. Conversely, for the smallest leak (5% flowrate for x_{L2} in Case M2), the success rate reaches the minimum of 11.61%. Across different cases, the success rates for leaks of 15% flowrate are concentrated between 42%-43%, while that of the 10% flowrate leaks are around 20%. This result is due to the fact that large leaks generally cause more detectable transient signals than small leaks.

Additionally, changes in diameter may affect transient signal dispersion and waveform distortion, with a greater degradation on high-frequency signals (mainly from small leaks) than on low-frequency signals (which dominate in large leaks).

All successful results under length uncertainty show a consistent success rate of 2.5%, the same as the results in single leak cases, with the related uncertainties around μ_L. The detection results for other L are relatively stable, with the results for x^{L1} demonstrating more stability compared to the ones for x^{L2}, as small leaks tend to have weaker transient reflections, and minor changes in L can result in unstable recognition of their features, leading to unpredictable jumps and inconsistencies in localization results.

Table 6.7 presents the COV and success-uncertainty ratios for all multiple leak cases are listed in Table 6.7, supporting the observation on leak localization. Consistent with single leak detection, the proposed method performs the highest success detection rate under steady friction uncertainty, with S > 90%. This is followed by diameter uncertainty, which shows S > 40% for large leaks and S > 10% for small leaks. Moreover, inaccuracies in the modeling of length and wave speed uncertainties significantly impact the detection accuracy, resulting in S = 2.5% for L and S < 1% for a.

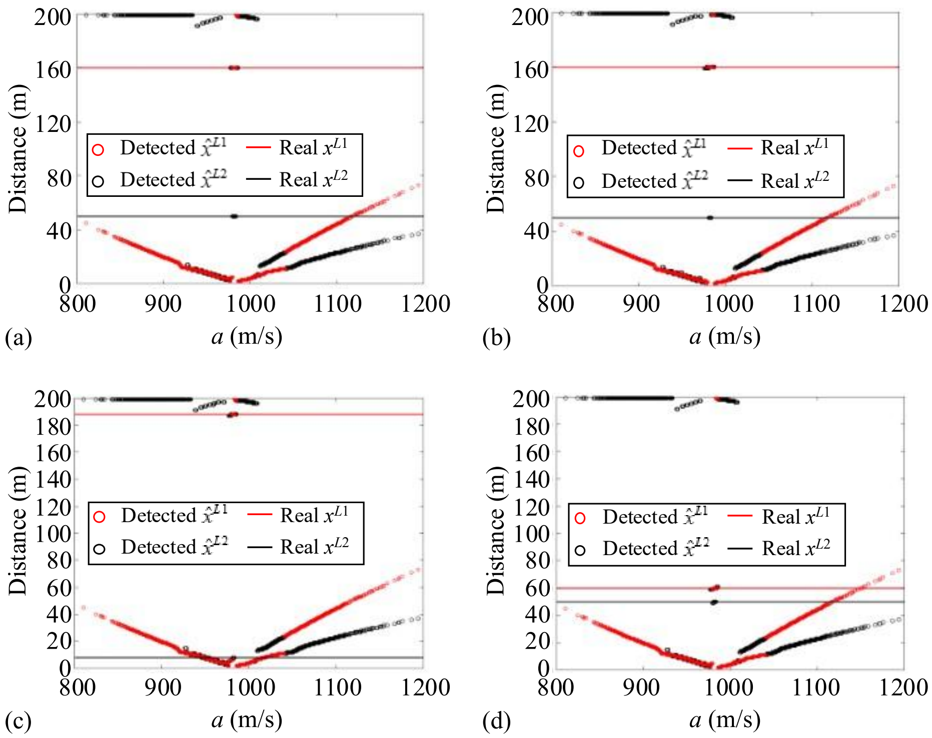

Figure 6.7 Leak localization results for wavespeed uncertainty: (a) Case M1; (b) Case M2; (c) Case M3; (d) Case M4

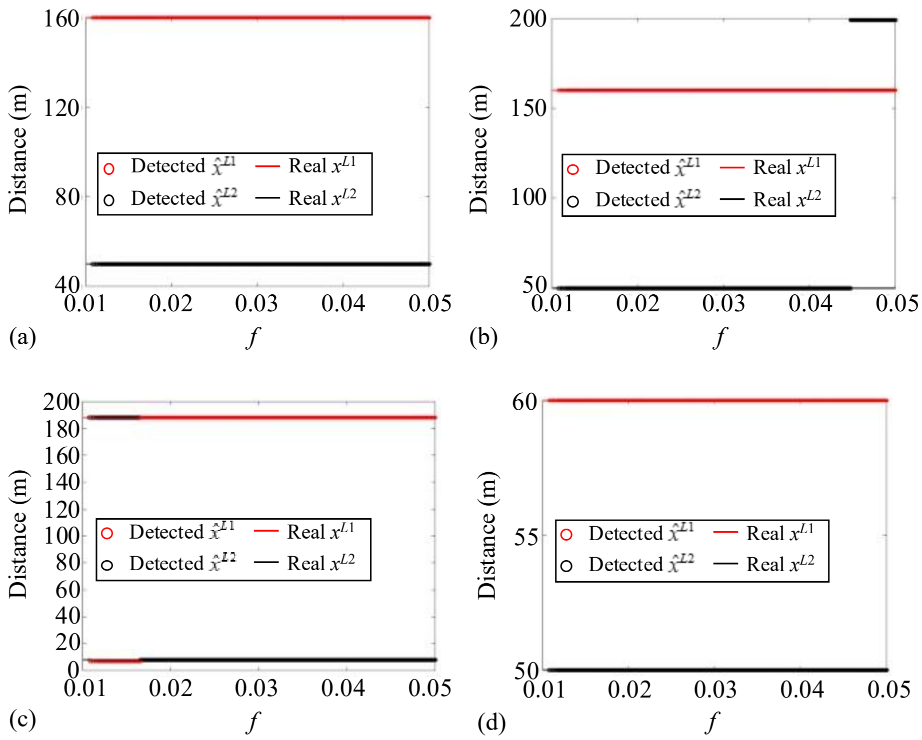

Figure 6.8 Leak localization results for steady friction uncertainty: (a) Case M1; (b) Case M2; (c) Case M3; (d) Case M4

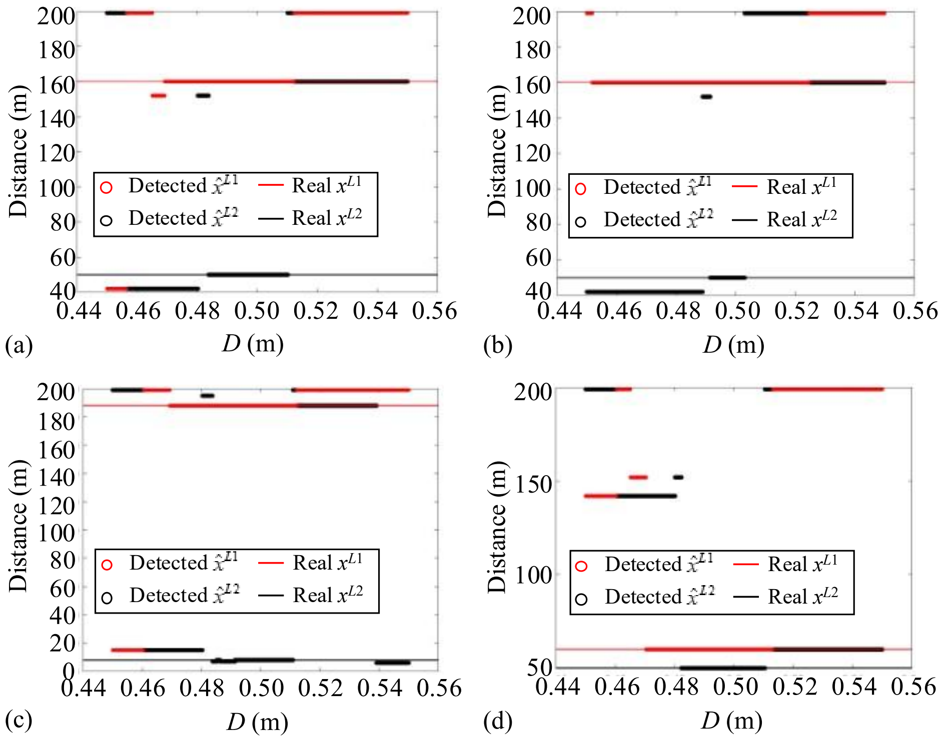

Figure 6.9 Leak localization results for diameter uncertainty: (a) Case M1; (b) Case M2; (c) Case M3; (d) Case M4

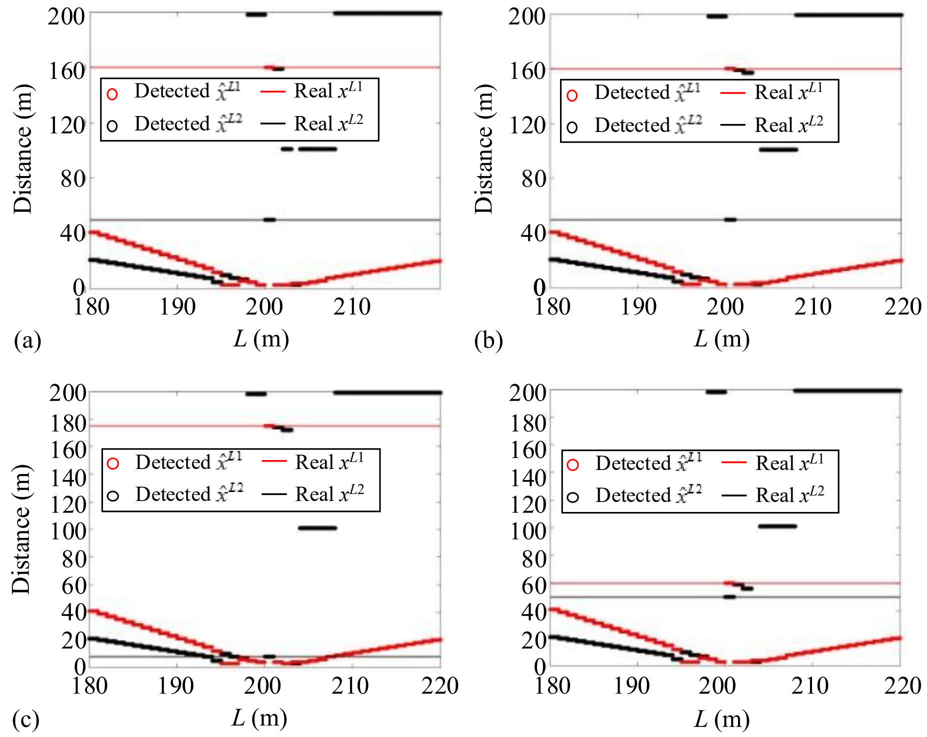

Figure 6.10 Leak localization results for length uncertainty: (a) Case M1; (b) Case M2; (c) Case M3; (d) Case M4

Table 6.6 Uncertainty of multiple leak localization results

Case No.	Uncertainty										
	a										
	x^{L1}						x^{L2}				
	Total test No.	Total μ	Total σ	Success test No.	Success μ_{as}	Success σ_{as}	Total μ	Total σ	Success test No.	Success μ_{as}	Success σ_{as}
M1	10000	18.92	36.01	281	981.2831	1.0797	86.28	89.08	281	981.2831	1.0797
M2		20.55	38.84	379	981.9393	1.4610	90.65	89.25	193	981.8712	0.7287
M3		18.11	35.91	193	981.8712	0.7287	92.55	91.62	103	982.4744	0.3338
M4		16.10	27.85	193	981.8712	0.7287	82.13	87.88	193	981.8712	0.7287
Case No.	Uncertainty										
	f										
	x^{L1}						x^{L2}				
	Total test No.	Total μ	Total σ	Success test No.	Success μ_{fs}	Success σ_{fs}	Total μ	Total σ	Success test No.	Success μ_{fs}	Success σ_{fs}
M1	10000	160.00	0.00	10000	0.0366	0.0094	50.00	0.00	10000	0.0366	0.0094
M2		160.00	0.00	10000	0.0366	0.0094	86.03	63.80	7582	0.0332	0.0082
M3		183.17	29.18	9733	0.0372	0.0088	12.81	29.02	9733	0.0372	0.0088
M4		160.00	0.00	10000	0.0366	0.0094	50.00	0.00	10000	0.0366	0.0094

Table 6.7 Uncertainty of multiple leak localization results (Cont.)

Case No.	Uncertainty										
	D										
		x^{L1}					x^{L2}				
	Total test No.	Total μ	Total σ	Success test No.	Success μ_{Ds}	Success σ_{Ds}	Total μ	Total σ	Success test No.	Success μ_{Ds}	Success σ_{Ds}
M1	10000	170.12	38.84	4303	0.4907	0.0124	106.03	60.96	2634	0.4970	0.0076
M2		170.60	17.35	7282	0.4882	0.0210	109.54	67.86	1161	0.4972	0.0034
M3		175.21	54.75	4279	0.4907	0.0124	86.19	89.77	1958	0.5011	0.0057
M4		131.30	64.15	4267	0.4917	0.0123	93.40	54.11	2816	0.4964	0.0081

Case No.	Uncertainty										
	L										
		x^{L1}					x^{L2}				
	Total test No.	Total μ	Total σ	Success test No.	Success μ_{Ls}	Success σ_{Ls}	Total μ	Total σ	Success test No.	Success μ_{Ls}	Success σ_{Ls}
M1	10000	19.78	24.96	250	200.5001	0.2893	93.35	84.75	250	200.5001	0.2893
M2		19.78	24.96	250	200.5001	0.2893	94.75	85.32	250	200.5001	0.2893
M3		20.20	27.06	250	200.5001	0.2893	94.45	86.74	250	200.5001	0.2893
M4		17.28	12.87	250	200.5001	0.2893	89.73	84.40	250	200.5001	0.2893

Table 6.7 Success-uncertainty ratio for all the cases for multiple leak detection

Case No.	Uncertainty							
	a				f			
	x^{L1}		x^{L2}		x^{L1}		x^{L2}	
	δ	S	δ	S	δ	S	δ	S
M1	0.0011	0.22%	0.0011	0.22%	0.2581	100.00%	0.2581	100.00%
M2	0.0015	0.30%	0.0007	0.15%	0.2581	100.00%	0.2481	96.61%
M3	0.0007	0.15%	0.0003	0.07%	0.2370	92.29%	0.2370	92.29%
M4	0.0007	0.15%	0.0007	0.15%	0.2581	100.00%	0.2581	100.00%

Case No.	Uncertainty							
	D				L			
	x^{L1}		x^{L2}		x^{L1}		x^{L2}	
	δ	S	δ	S	δ	S	δ	S
M1	0.0253	43.81%	0.0153	26.48%	0.0014	2.50%	0.0014	2.50%
M2	0.0431	74.51%	0.0067	11.67%	0.0014	2.50%	0.0014	2.50%
M3	0.0252	43.56%	0.0114	19.68%	0.0014	2.50%	0.0014	2.50%
M4	0.0251	43.35%	0.0164	28.34%	0.0014	2.50%	0.0014	2.50%

6.7Sensitivity Analysis

6.7.1 Single leak detection sensitivity analysis

To study the sensitivity of the proposed leak detection method to each uncertainty considered in this study, the distributions of all the localization errors and the joint distribution of uncertainty and absolute localization error are plotted and analyzed. For each uncertainty, the error and joint distribution of Case S1 are plotted below as a representative to reveal the statistical regularities intuitively. The correlation between each uncertainty and the errors is also discussed.

For the localization errors in the wave speed uncertainty, the error histogram in Figure 6.11(a) shows a left-skewed distribution, indicating that the majority of localization results are on the upstream of than the true leak with large error fluctuations, demonstrating significant variability of the localization results and the low robustness of the approach due to the inaccuracies between the modeling and designed wave speed. In Figure 6.11(b), the joint distribution shows an overall S-shaped trend, proving the highly nonlinear relationship between wave speed and $|e|$. In the central part of the curve, where a is close to its mean value (in blue dashed line), $|e|$ appeared minimal, suggesting high detection accuracy. The increased probability density function (PDF) of this region is due to the alignment of fixed localization results with real location, as evidenced in Figure 6.3(a). Conversely, when a is far away from its mean, the distribution of $|e|$ becomes wider. The mean of $|e|$ (in the red dashed line) is higher than the $|e|$ corresponding to the mean of a, indicating that the large errors of an increase the overall average localization error.

For steady friction uncertainty, the detection accuracy is 100% in the tests for

Case S1. Therefore, the localization error distribution shown in Figure 6.12(a) has a uniform value of 0. Accordingly, the distribution of $|e|$ under different f is presented in Figure 6.12(b), which also appears uniform, indicating no significant relationship between $|e|$ and f.

For diameter uncertainty, the distribution of localization error in Figure 6.13(a) is discrete, concentrating on a few specific values, as also shown in Figure 6.5(a). The mean error is clearly biased toward larger error values, since large errors exert a greater influence on the mean. This discrete distribution is further illustrated in the joint distribution in Figure 6.13(b), which appears as high probability density areas of $|e|$ distributed across different values of D, indicating no evident linear or nonlinear relationship between $|e|$ and D. When D is close to its mean, $|e|$ equals 0 with accurate localization results. It implies that the proposed method performs best when D near its mean, demonstrating the strongest applicability.

In cases of length uncertainty, localization errors are typically negative, indicating a systematic underestimation of the leak location. The error distribution is concentrated between -40m and -25m, dispersing to 0m. This is due to the deviation between the fixed localization result and the actual leak. The joint distribution in Figure 6.14(b) shows an inverted V-shaped trend, with the absolute error being smallest near the L mean and increasing as it moves further away from the L mean.

To further quantitatively analyze the relationship between the uncertainties and the localization results, the statistical significance (p-value) of the correlation between the uncertainty and absolute error is calculated using Spearman's rank correlation coefficient (ρ). The absolute value of ρ reflects the strength of correlation;

the closer ρ is to 0, the weaker the correlation. On the other hand, the p-value demonstrates the significance of the correlation, a smaller the p-value indicates a more significant correlation.

Assume the two variables are X and Y, each with n samples. Sort X and Y respectively by their numerical values, and the rank of each data point is its position after sorting. The Spearman's correlation coefficient ρ is calculated with

$$\rho = \frac{1-6\sum_{i=1}^{n} d_i^2}{n(n^2-1)} \tag{6.6}$$

in which d_i is the rank difference of the i-th sample in X and Y. Followed by the calculation of *the* t-statistic by

$$t = \rho\sqrt{\frac{n-2}{1-\rho^2}} \tag{6.7}$$

This statistic follows a t-distribution with degrees of freedom $df = n - 2$. The p-value can then be found through a t-distribution table or statistical software.

The results are listed in Figure 6.5. The findings include:

(1). Wave speed uncertainty: The correlation with $|e|$ is weak ($|\rho|$ ranges from 0.157 to 0.364) but statistically significant ($p \approx 0$).

(2). Steady friction uncertainty: All the leaks are accurately located except for Case S3, where f shows a moderately strong correlation with high significance.

(3). Diameter uncertainty: The correlation with $|e|$ is extremely weak in most cases ($|\rho|$ ranges from 0.005 to 0.246) but remains statistically significant.

(4). Length uncertainty: A strong positive correlation with $|e|$ is indicated ($|\rho|$ is close to 0.5), and it is statistically significant.

The findings indicate the sensitivity and tolerance of the proposed method in single leak localization. Among the four uncertainties, the method demonstrates the highest sensitivity and the lowest tolerance to changes in pipe length, with wave speed following closely behind. On the contrary, it shows low sensitivity and high tolerance to changes in diameter. Nevertheless, it maintains the highest tolerance for steady friction changes, as long as the leak size is not overly small.

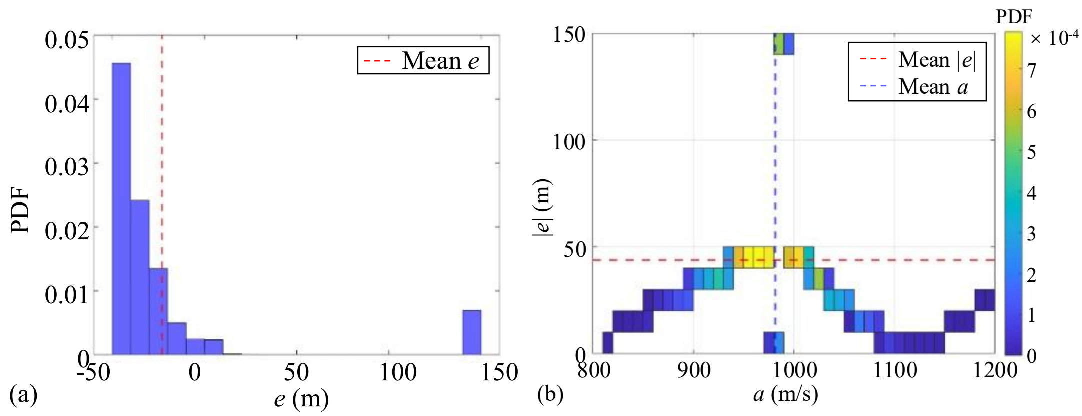

Figure 6.11. Localization error distribution and wavespeed-absolute error joint distribution for Case S1 under wavespeed uncertainty: (a) detection error distribution; (b) wavespeed-absolute error joint distribution

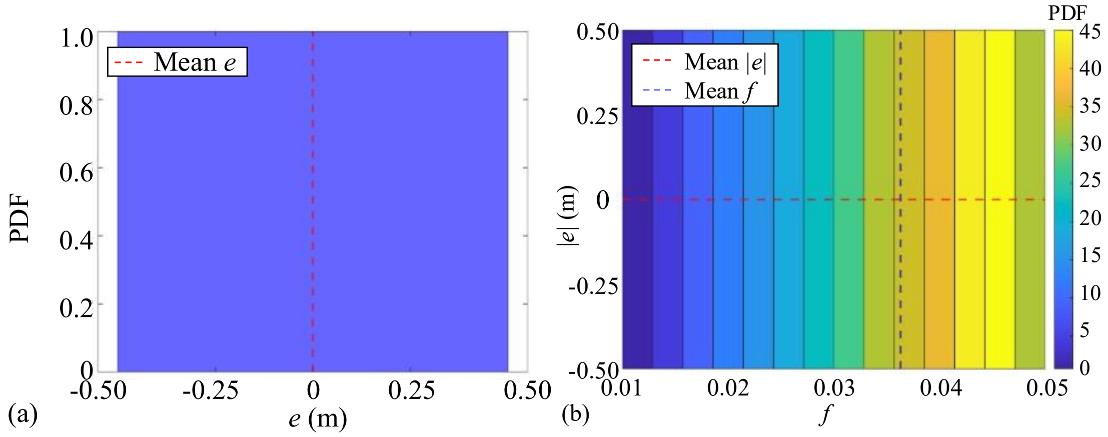

Figure 6.12 Localization error distribution and steady friction-absolute error joint distribution for Case S1 under steady friction uncertainty: (a) detection error distribution; (b) steady friction-absolute error joint distribution

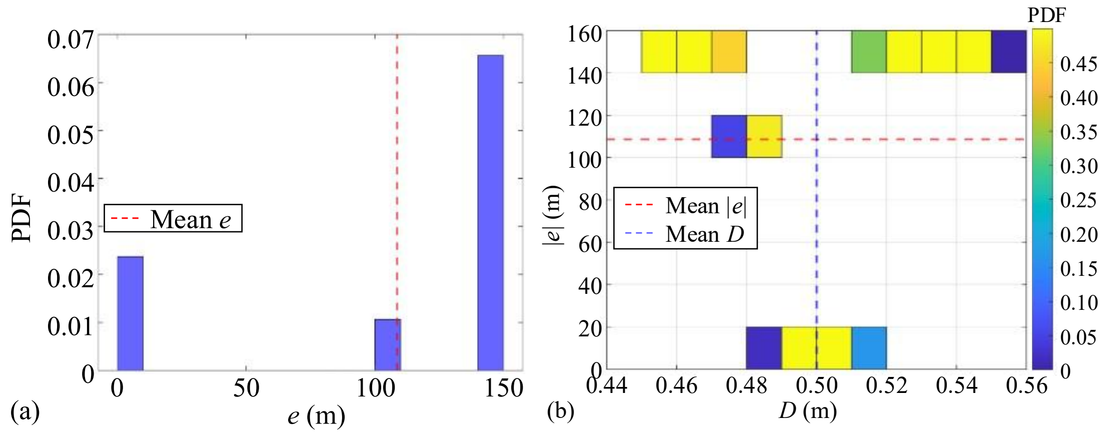

Figure 6.13 Localization error distribution and diameter-absolute error joint distribution for Case S1 under diameter uncertainty: (a) detection error distribution; (b) diameter-absolute error joint distribution

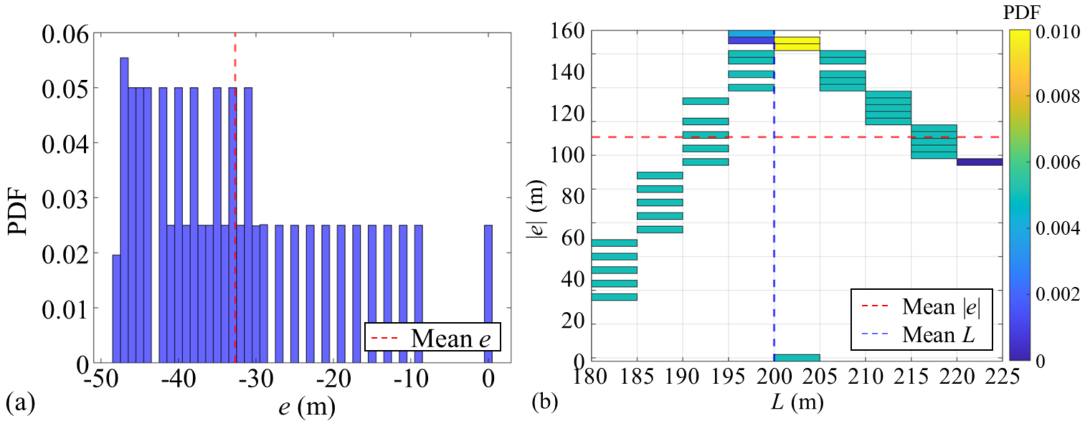

Figure 6.14 Localization error distribution and length-absolute error joint distribution for Case S1 under length uncertainty: (a) detection error distribution; (b) length-absolute error joint distribution

Table 6.8 Sensitivity analysis among uncertainties and absolute localization errors for single leak cases

Case No.	Uncertainty							
	a		*f*		*D*		*L*	
	$\|\rho\|$	p	$\|\rho\|$	p	$\|\rho\|$	p	$\|\rho\|$	p
S1	0.16	2.28E-58	N/A	N/A	0.064	1.63E-10	0.468	0.00E+00
S2	0.207	5.12E-97	N/A	N/A	0.246	1.93E-137	0.457	0.00E+00
S3	0.157	4.37E-56	0.45	0.00E+00	0.005	6.43E-01	0.468	0.00E+00
S4	0.364	2.321E-310	N/A	N/A	0.028	4.57E-03	0.499	0.00E+00
S5	0.213	2.05E-103	N/A	N/A	0.136	9.01E-43	0.468	0.00E+00

6.7.2 Multiple leak detection sensitivity analysis

To analyze the sensitivity of the proposed method for detecting multiple leaks across four uncertainties, the localization error distribution histogram and the joint distribution of uncertainty and the absolute value of localization error for both Leak 1 and Leak 2 in Case M1 are plotted in Figures 6.15-18 as representative.

The localization error for x^{L1} when dealing with wave speed uncertainty in Figure 6.15(a) primarily concentrates between -150m and -100m, exhibiting a clear left-skewed distribution with a negative mean value. This aligns with the x_{L1} localization result in Figure 6.11(a), where most detected leaks are upstream of the actual position. Correspondingly, Figure 6.15(b) shows that $|e|$ follows an inverted U-shaped distribution and is concentrated in the upper part, with low |e| values observed in the central section around μ_a. For x^{L2} localization, the error reveals a bimodal distribution with peaks at approximately -50 m and 150 m, as seen in Figure 6.15(c). Meanwhile, the joint distribution of $|e|$ and a in Figure 6.15(d) shows a dispersed pattern, lacking a clear linear or monotonic relationship. The comparison between the detection errors for x^{L1} and x^{L2} indicates that the large leak shows obvious and consistent errors, whereas the small leak demonstrates more complex performance with inconsistent results and frequent misinterpretations. This proves that the performance of the proposed method is more stable for large leak detection.

For leak detection under f uncertainty, both leaks are correctly located in all the tests with e = 0 m. The joint distributions of f and absolute errors also show uniform and stable distributions, indicating the robustness and stability of the method.

Under the D uncertainty, similar to the single leak detection, the error distributions in this case show a discrete pattern concentrated around specific values (see Figure 6.17 (a) and (b)), where the error of x^{L1} is more concentrated than that of x^{L2}. As D increases, the $|e|$ distribution of x^{L2} widens significantly than the |e| of x^{L1}. This indicates that the detection of small leaks is more susceptible to diameter changes, showing greater instability.

Under the L uncertainty, the error distribution for x^{L1} in Figure 6.18(a) is highly concentrated in negative values with a left-skewed pattern, indicating the constant underestimate of the real leak location with the fixed results. This trend is also reflected in Figure 6.18(b), where an inverted U-shaped distribution is formed. Conversely, x^{L2}'s errors showed no distinct distribution trend, reflecting unstable detection performance for small leak detection under L.

A sensitivity analysis of uncertainties and absolute localization errors for multiple leak cases is conducted, with corresponding $|\rho|$ and p values plotted in Table 6.9. For a uncertainty, the $|e|$ for big leaks (x^{L1}) exhibit minor $|\rho|$ values (0 – 0.008) and high p values ($p > 0.4$), indicating the weak and statistically insignificant correlation between $|e|$ and a. In contrast, a shows a strong and significant impact on small leaks (x^{L2}) with large $|\rho|$ and low p values. For f uncertainty, except for the accurate test results, f exhibits a moderate yet significant correlation with $|e|$. For both leaks, the D uncertainty shows strong correlation for Cases M2 and M4 ($|\rho|$>0.5), and smaller correlation for Cases M1 and M3; all correlations are significant. The L uncertainty exhibits a large and significant correlation with $|e|$ in all four cases, highlighting the dominant influence of L for different cases. In general, the effect of uncertainties on the proposed leak detection method is ranked as $L > a >> D > f$.

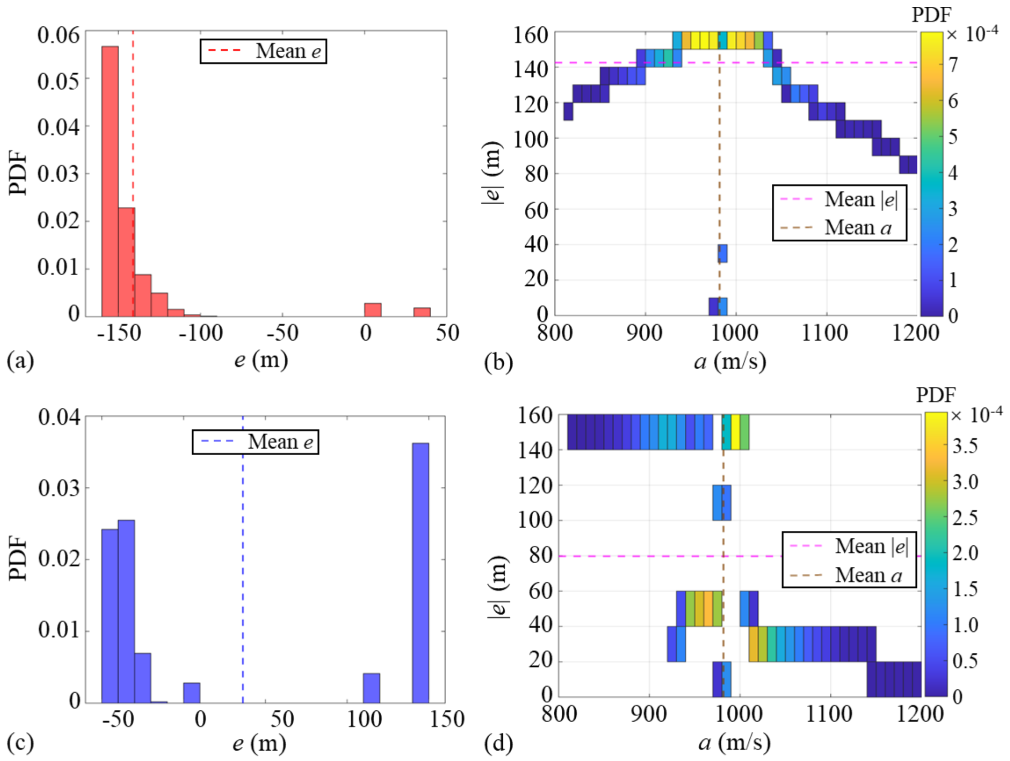

Figure 6.15 Localization error distribution and wavespeed-absolute error joint distribution for Case M1 under wavespeed uncertainty: (a) detection error distribution for x^{L1}; (b) wavespeed-absolute error joint distribution for x^{L1}; (c) detection error distribution for x^{L2}; (d) wavespeed-absolute error joint distribution for x^{L2}

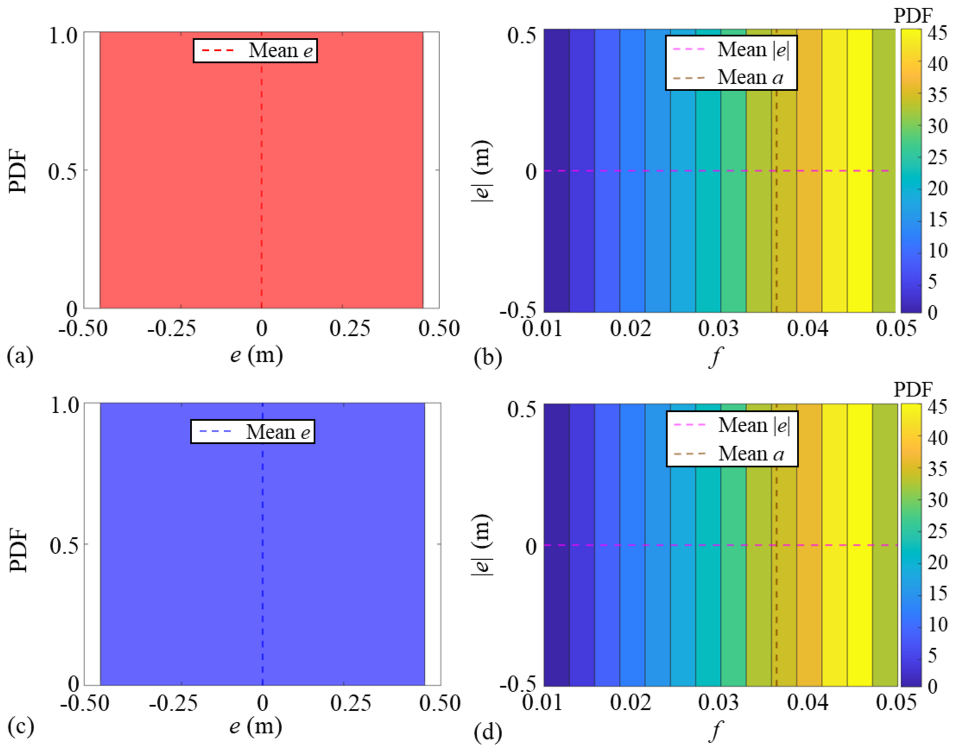

Figure 6.16 Localization error distribution and steady friction-absolute error joint distribution for Case M1 under steady friction uncertainty: (a) detection error distribution for x^{L1}; (b) steady friction-absolute error joint distribution for x^{L1}; (c) detection error distribution for x^{L2}; (d) steady friction-absolute error joint distribution for x^{L2}

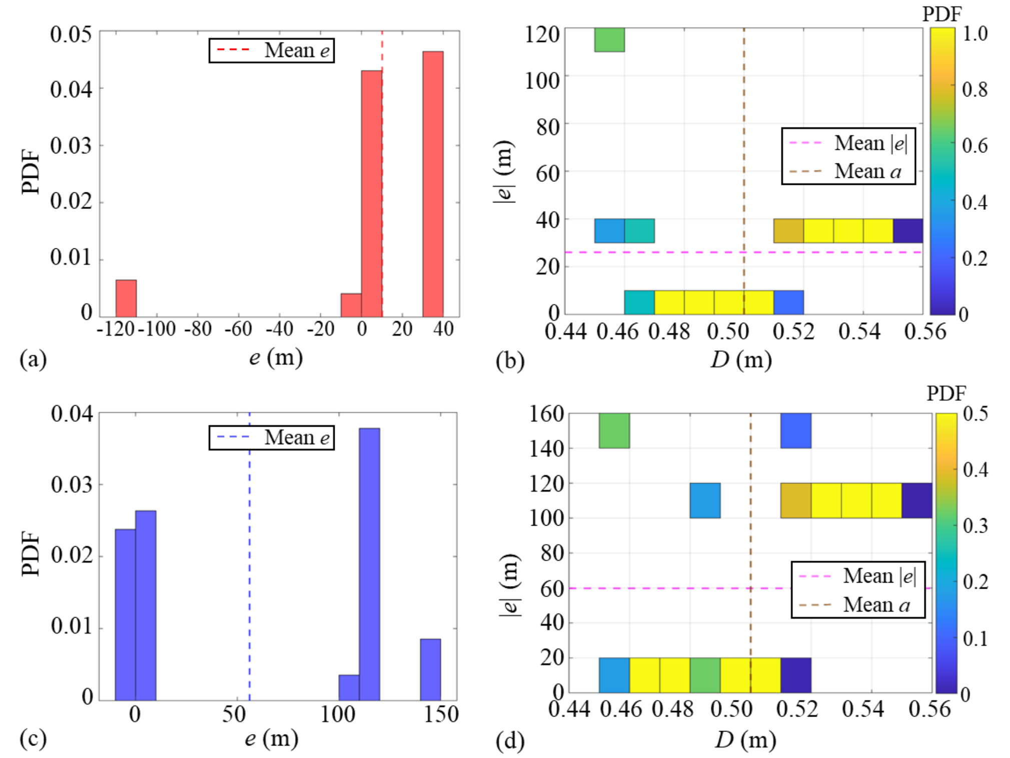

Figure 6.17 Localization error distribution and diameter-absolute error joint distribution for Case M1 under diameter uncertainty: (a) detection error distribution for x^{L1}; (b) diameter-absolute error joint distribution for x^{L1}; (c) detection error distribution for x^{L2}; (d) diameter-absolute error joint distribution for x^{L2}

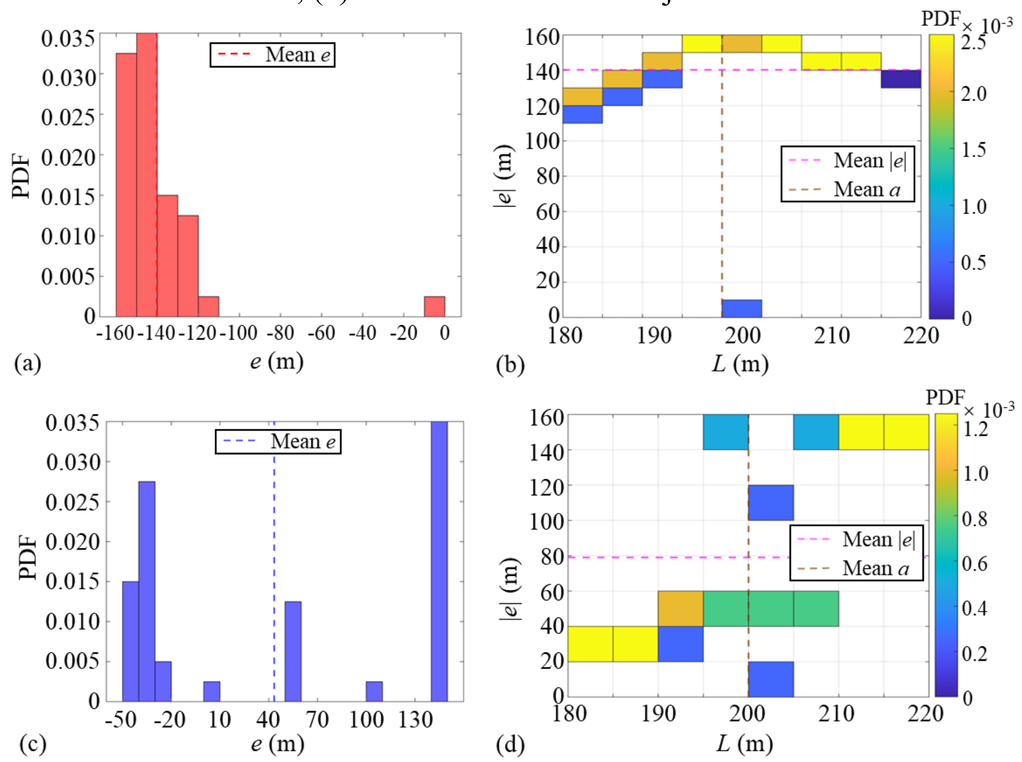

Figure 6.18 Localization error distribution and length-absolute error joint distribution for Case M1 under length uncertainty: (a) detection error distribution for x^{L1}; (b) length-absolute error joint distribution for x^{L1}; (c) detection error distribution for x^{L2}; (d) length-absolute error joint distribution for x^{L2}

Table 6.9 Sensitivity analysis among uncertainties and absolute localization errors for multiple leak cases

Case No.	Uncertainty							
	a				f			
	x^{L1}		x^{L2}		x^{L1}		x^{L2}	
	$\|\rho\|$	p	$\|\rho\|$	p	$\|\rho\|$	p	$\|\rho\|$	p
M1	0.008	4.32E-01	0.631	0.00E+00	N/A	N/A	N/A	N/A
M2	0.008	4.15E-01	0.640	0.00E+00	N/A	N/A	0.742	0.00E+00
M3	0.006	5.20E-01	0.173	1.06E-67	0.279	1.73E-178	0.279	1.72E-178
M4	0.000	9.79E-01	0.605	0.00E+00	N/A	N/A	N/A	N/A

Case No.	Uncertainty							
	D				L			
	x^{L1}		x^{L2}		x^{L1}		x^{L2}	
	$\|\rho\|$	p	$\|\rho\|$	p	$\|\rho\|$	p	$\|\rho\|$	p
M1	0.198	1.01E-88	0.319	6.47E-235	0.444	0.00E+00	0.923	0.00E+00
M2	0.669	0.00E+00	0.634	0.00E+00	0.444	0.00E+00	0.922	0.00E+00
M3	0.060	1.78E-09	0.156	2.05E-55	0.443	0.00E+00	0.715	0.00E+00
M4	0.507	0.00E+00	0.442	0.00E+00	0.444	0.00E+00	0.839	0.00E+00

6.8 Summary and Conclusion

This chapter investigates the impact of various uncertainties on the detection effectiveness of the proposed transient-based time-domain parameter separation method for leak detection. An RPV system, with single and multiple leaks, is employed, and four common uncertainty factors - wave speed, steady friction, pipe diameter, and pipe length - are considered to evaluate and discuss the performance of the proposed method in leak localization. The two systems include 5 and 4 different cases, respectively, and each case consisted of 10,000 tests.

The results indicate that modeling uncertainties can induce substantial variations in transient flow responses and, consequently, in transient-based leak localization outcomes. A preliminary sensitivity analysis reveals that the proposed method exhibits significantly higher detection effectiveness and robustness under uncertainties in pipe diameter and steady friction, whereas variations in wave speed and pipe length have a more pronounced impact on localization accuracy. These findings highlight the relative sensitivity of transient-based leak detection to different physical parameters and provide guidance for prioritizing parameter calibration in practical applications.

CHAPTER 7 CONCLUSIONS AND RECOMMENDATIONS

7.1 Conclusions

The overall aim of this thesis is to develop an efficient time-domain transient wave analysis framework, grounded in an improved understanding of transient wave dynamics and their interaction with pipe walls. To achieve this aim, a factorized transient model and a new leak detection method are proposed, and their validation is conducted using both RPV and pipe network systems. A sensitivity analysis is then carried out to evaluate the robustness of the proposed method under different sources of uncertainty.

First, a factorized transient wave model for pressurized pipeline systems with both single and multiple leaks is analytically developed. Building upon this model, a transient-based time-domain leak detection method is proposed, which involves parameter separation for single leaks and a combination of iterative beamforming with parameter separation for multiple leaks.

Second, the case studies and discussion of the proposed leak detection framework in RPV systems are investigated numerically and experimentally. The validation begins with an experimental single leak case to illustrate the basic working mechanism of the method, followed by two leak cases for a more comprehensive evaluation through both numerical simulations and experimental tests. The results indicate that the proposed approach is accurate, efficient, super-resolved, and robust in localizing both single and multiple leaks in RPV systems.

Afterwards, the proposed method is numerically extended to more complex network systems with a single leak is investigated. Numerical applications and sensitivity analyses demonstrate that the method is accurate and effective for single leak detection in complex pipe systems, while its robustness is further evidenced through successful leak parameter separation applications. Collectively, these results confirm the applicability, accuracy, efficiency, and robustness of the proposed method.

Finally, the impact of four different uncertainties on the effectiveness of the proposed leak detection method is investigated in an RPV system with both single and multiple leaks. The performance of the method in leak localization is evaluated and discussed. The results indicate that these uncertainties can induce substantial variations in transient wave modeling, and consequently in transient-based leak localization results. The method demonstrates considerably higher effectiveness and robustness against uncertainties in pipe diameter and steady friction compared with variations in wave speed and pipe length.

7.2 Recommendations for Future Work

The following research directions are recommended for future work:

1. In this study, multiple-leak localization is primarily investigated in reservoir-pipe-valve systems, while applications to pipe network systems are limited to single-leak scenarios. Future work should extend the proposed framework to multiple-leak detection in complex pipe networks, including comprehensive uncertainty and

sensitivity analyses to assess scalability and reliability.

2. Currently, the effectiveness of the proposed method remains dependent on modeling accuracy, leading to performance variations under different sources of uncertainty. Further research is therefore needed to enhance the robustness of the developed method, for example through improved parameter calibration, adaptive modeling strategies, or uncertainty-aware inversion techniques, to achieve more reliable leak localization under modeling errors.

3. Current study focuses primarily on leak detection, whereas multiple simultaneous leaks are relatively uncommon in real-world pipeline systems. Future research should broaden the scope of the detection framework to include other types of pipeline defects, such as blockages, air pockets, and structural deformations, to improve its applicability to realistic operational conditions.

REFERENCE

Al-Washali, T. M. (2021). *Water loss assessment in distribution networks: Methods, applications and implications in intermittent supply*. CRC Press.

Amein, M., & Chu, H.-L. (1975). Implicit numerical modeling of unsteady flows. *Journal of the Hydraulics Division*, *101*(6), 717-731.

Asghari, V., Kazemi, M. H., Duan, H.-F., Hsu, S.-C., & Keramat, A. (2023). Machine learning modeling for spectral transient-based leak detection. *Automation in Construction*, *146*, 104686.

Ayati, A. H., Haghighi, A., & Lee, P. J. (2019). Statistical review of major standpoints in hydraulic transient-based leak detection. *Journal of Hydraulic Structures*, *5*(1), 1-26.

Barfuss, S. L., & Fugal, M. (2025). Water main break rates in the United States and Canada. *Journal of the American Water Works Association*, *117*(2), 22-33.

Beck, S. B., Curren, M., Sims, N. D., & Stanway, R. (2005). Pipeline network features and leak detection by cross-correlation analysis of reflected waves. *Journal of hydraulic engineering*, *131*(8), 715-723.

Bergant, A., Ross Simpson, A., & Vìtkovsk, J. (2001). Developments in unsteady pipe flow friction modelling. *Journal of Hydraulic Research*, *39*(3), 249-257.

Bergant, A., Tijsseling, A. S., Vítkovský, J. P., Covas, D. I., Simpson, A. R., &

Lambert, M. F. (2008). Parameters affecting water-hammer wave attenuation, shape and timing—Part 1: Mathematical tools. *Journal of Hydraulic Research*, *46*(3), 373-381.

Bohorquez, J., Alexander, B., Simpson, A. R., & Lambert, M. F. (2020). Leak detection and topology identification in pipelines using fluid transients and artificial neural networks. *Journal of Water Resources Planning and Management*, *146*(6), 04020040.

Born, M. (1926). Quantenmechanik der stoßvorgänge. *Zeitschrift für physik*, *38*(11), 803-827.

Brunone, B. (1999). Transient test-based technique for leak detection in outfall pipes. *Journal of Water Resources Planning and Management*, *125*(5), 302-306.

Brunone, B., & Ferrante, M. (2001). Detecting leaks in pressurised pipes by means of transients. *Journal of Hydraulic Research*, *39*(5), 539-547.

Brunone, B., Golia, U., & Greco, M. (1991). Modelling of fast transient by numerical methods. Int. Meeting on hydraulic transient and water column separation,

Brunone, B., Golia, U., & Greco, M. (1995). Effects of two-dimensionality on pipe transients modeling. *Journal of hydraulic engineering*, *121*(12), 906-912.

Brunone, B., Maietta, F., Capponi, C., Keramat, A., & Meniconi, S. (2022). A review of physical experiments for leak detection in water pipes through transient tests for addressing future research. *Journal of Hydraulic Research*, *60*(6), 894-906.

Brunone, B., Meniconi, S., & Capponi, C. (2018). Numerical analysis of the transient pressure damping in a single polymeric pipe with a leak. *Urban Water Journal*, *15*(8), 760-768.

Capelo, M., Brentan, B., Monteiro, L., & Covas, D. (2021). Near–Real Time Burst Location and Sizing in Water Distribution Systems Using Artificial Neural Networks. *Water*, *13*(13), 1841.

Capponi, C., Ferrante, M., Zecchin, A. C., & Gong, J. (2017). Leak detection in a branched system by inverse transient analysis with the admittance matrix method. *Water Resources Management*, *31*(13), 4075-4089.

Capponi, C., Meniconi, S., Lee, P. J., Brunone, B., & Cifrodelli, M. (2020). Time-domain analysis of laboratory experiments on the transient pressure damping in a leaky polymeric pipe. *Water Resources Management*, *34*, 501-514.

Chaudhry, M., & Hussaini, M. (1985). Second-order accurate explicit finite-difference schemes for waterhammer analysis. *Journal of Fluids Engineering*, *107*(4), 523-529.

Chaudhry, M. H. (2014). *Applied hydraulic transients* (Vol. 415). Springer.

Che, T.-C., Duan, H.-F., & Lee, P. J. (2021). Transient wave-based methods for anomaly detection in fluid pipes: A review. *Mechanical Systems and Signal*

Processing, *160*, 107874.

Che, T.-C., Wang, X., & Ghidaoui, M. S. (2022). Leak localization in looped pipe networks based on a factorized transient wave model: Theoretical framework. *Water Resources Research*, *58*(4), e2021WR031364.

Che, T.-C., Wang, X., Louati, M., Zhou, L., & Ghidaoui, M. S. (2022). Leak localization in looped pipe networks based on a factorized transient wave model: 2. regularization of ill-conditioned problems. *Water Resources Research*, *58*(11).

Che, T.-C., Wang, X., Zhou, L., & Duan, H. F. (2022). Modified factorized transient wave model in tree pipe networks for leak localization with less boundary measurements. *Water Resources Research*, *58*(12), e2022WR032856.

Chen, J., Tang, P., Rakstad, T., Patrick, M., & Zhou, X. (2020). Augmenting a deep-learning algorithm with canal inspection knowledge for reliable water leak detection from multispectral satellite images. *Advanced engineering informatics*, *46*, 101161.

Covas, D., & Ramos, H. (2010). Case studies of leak detection and location in water pipe systems by inverse transient analysis. *Journal of Water Resources Planning and Management*, *136*(2), 248-257.

Covas, D., Stoianov, I., Mano, J. F., Ramos, H., Graham, N., & Maksimovic, C. (2005). The dynamic effect of pipe-wall viscoelasticity in hydraulic transients. Part II—Model development, calibration and verification. *Journal of Hydraulic Research*, *43*(1), 56-70.

Covas, D., Stoianov, I., Ramos, H., Graham, N., & Maksimovic, C. (2004). The dynamic effect of pipe-wall viscoelasticity in hydraulic transients. Part I—Experimental analysis and creep characterization. *Journal of Hydraulic Research*, *42*(5), 517-532.

Di Pierro, F., Khu, S.-T., Savić, D., & Berardi, L. (2009). Efficient multi-objective optimal design of water distribution networks on a budget of simulations using hybrid algorithms. *Environmental modelling & software*, *24*(2), 202-213.

Duan, H.-F. (2017). Transient frequency response based leak detection in water supply pipeline systems with branched and looped junctions. *Journal of Hydroinformatics*, *19*(1), 17-30.

Duan, H.-F. (2018). Accuracy and sensitivity evaluation of TFR method for leak detection in multiple-pipeline water supply systems. *Water Resources Management*, *32*(6), 2147-2164.

Duan, H.-F., Che, T.-C., Lee, P. J., & Ghidaoui, M. S. (2018). Influence of nonlinear turbulent friction on the system frequency response in transient pipe flow modelling and analysis. *Journal of Hydraulic Research*, *56*(4), 451-463.

Duan, H.-F., Ghidaoui, M. S., & Tung, Y.-K. (2009). An efficient quasi-2D simulation of waterhammer in complex pipe systems.

Duan, H.-F., Lee, P. J., Ghidaoui, M. S., & Tung, Y.-K. (2011). Leak detection in complex series pipelines by using the system frequency response method. *Journal of Hydraulic Research*, *49*(2), 213-221.

Duan, H.-F., Lee, P. J., Ghidaoui, M. S., & Tung, Y.-K. (2012). System response function–based leak detection in viscoelastic pipelines. *Journal of hydraulic engineering*, *138*(2), 143-153.

Duan, H.-F., Pan, B., Wang, M., Chen, L., Zheng, F., & Zhang, Y. (2020). State-of-the-art review on the transient flow modeling and utilization for urban water supply system (UWSS) management. *Journal of Water Supply: Research and Technology-Aqua*, *69*(8), 858-893.

Duan, H. F., & Keramat, A. (2022). Uncertainty quantification of transient-based leakage identification: a frequency domain framework. *Water Resources Research*, *58*(12).

Farah, E., & Shahrour, I. (2024). Water leak detection: a comprehensive review of methods, challenges, and future directions. *Water*, *16*(20), 2975.

Farley, M., & Trow, S. (2003). *Losses in water distribution networks*. IWA publishing.

Ferrante, M., & Brunone, B. (2003a). Pipe system diagnosis and leak detection by unsteady-state tests. 1. Harmonic analysis. *Advances in water resources*, *26*(1), 95-105.

Ferrante, M., & Brunone, B. (2003b). Pipe system diagnosis and leak detection by unsteady-state tests. 2. Wavelet analysis. *Advances in water resources*, *26*(1), 107-116.

Ferrante, M., Brunone, B., & Meniconi, S. (2007). Wavelets for the analysis of transient pressure signals for leak detection. *Journal of hydraulic engineering*, *133*(11), 1274-1282.

Ferrante, M., Brunone, B., & Meniconi, S. (2009a). Leak-edge detection. *Journal of Hydraulic Research*, *47*(2), 233-241.

Ferrante, M., Brunone, B., & Meniconi, S. (2009b). Leak detection in branched pipe systems coupling wavelet analysis and a Lagrangian model. *Journal of Water Supply: Research and Technology—AQUA*, *58*(2), 95-106.

Ferry, J. D. (1980). *Viscoelastic properties of polymers*. John Wiley & Sons.

Ghazali, M., Beck, S., Shucksmith, J., Boxall, J., & Staszewski, W. (2012). Comparative study of instantaneous frequency based methods for leak detection in pipeline networks. *Mechanical Systems and Signal Processing*, *29*, 187-200.

Ghidaoui, M. S. (2004). On the fundamental equations of water hammer. *Urban Water Journal*, *1*(2), 71-83.

Ghidaoui, M. S., Zhao, M., McInnis, D. A., & Axworthy, D. H. (2005). A review of water hammer theory and practice. *Appl. Mech. Rev.*, *58*(1), 49-76.

Gong, J., Che, T.-C., Zeng, W., & Bilal, M. (2024). Advances in Hydraulic Transient-Based Pipeline Condition Assessment and Feature Diagnosis.

Gong, J., Stephens, M. L., Arbon, N. S., Zecchin, A. C., Lambert, M. F., & Simpson, A. R. (2015). On-site non-invasive condition assessment for cement mortar–lined metallic pipelines by time-domain fluid transient analysis. *Structural Health Monitoring*, *14*(5), 426-438.

Gong, J., Zecchin, A. C., Simpson, A. R., & Lambert, M. F. (2014). Frequency response diagram for pipeline leak detection: Comparing the odd and even harmonics. *Journal of Water Resources Planning and Management*, *140*(1), 65-74.

Haghighi, A., & Ramos, H. M. (2012). Detection of leakage freshwater and friction factor calibration in drinking networks using central force optimization. *Water Resources Management*, *26*, 2347-2363.

Henry, R., & Luxmoore, A. (1996). A pipe-profiling adapter for CCTV inspection cameras: development of a pipe-profiling instrument. *Measurement Science and Technology*, *7*(4), 495.

HKWSD. (2025). *Risk-based Improvement Programme of Water Mains*.

Hu, Z., Chen, B., Chen, W., Tan, D., & Shen, D. (2021). Review of model-based and data-driven approaches for leak detection and location in water distribution systems. *Water Supply*, *21*(7), 3282-3306.

Hu, Z., Tariq, S., & Zayed, T. (2021). A comprehensive review of acoustic based leak localization method in pressurized pipelines. *Mechanical Systems and Signal Processing*, *161*, 107994.

Huang, Y., Zheng, F.-F., Kapelan, Z. S., Savic, D. A., Duan, H.-F., & Zhang, Q.-z. (2020). Efficient leak localization in water distribution systems using multistage optimal valve operations and smart demand metering. *Water Resources Research*, *56*(10).

Hunaidi, O. (1998). Ground-penetrating radar for detection of leaks in buried plastic water distribution pipes. Proceedings of the seventh international conference on Ground Penetrating Radar, 1998,

Jung, B., & Karney, B. (2008). Systematic exploration of pipeline network calibration using transients. *Journal of Hydraulic Research*, *46*(sup1), 129-137.

Kapelan, Z. S., Savic, D. A., & Walters, G. A. (2003). A hybrid inverse transient model for leakage detection and roughness calibration in pipe networks. *Journal of Hydraulic Research*, *41*(5), 481-492.

Kapelan, Z. S., Savic, D. A., & Walters, G. A. (2004). Incorporation of prior information on parameters in inverse transient analysis for leak detection and roughness calibration. *Urban Water Journal*, *1*(2), 129-143.

Keramat, A., Ahmadianfar, I., Duan, H.-F., & Hou, Q. (2023). Spectral transient-based multiple leakage identification in water pipelines: An efficient hybrid gradient-metaheuristic optimization. *Expert Systems with Applications*, *224*, 120021.

Keramat, A., Duan, H.-F., Pan, B., & Hou, Q. (2022). Gradient-based optimization for spectral-based multiple-leak identification. *Mechanical Systems and Signal Processing*, *171*, 108840.

Kim, S. (2022). Time-domain impedance method for transient analysis and leakage detection in reservoir pipeline valve systems. *Mechanical Systems and Signal Processing*, *167*, 108527.

Kim, S. H. (2016). Impedance method for abnormality detection of a branched pipeline system. *Water Resources Management*, *30*, 1101-1115.

Kim, S. H. (2018). Development of multiple leakage detection method for a reservoir pipeline valve system. *Water Resources Management*, *32*(6), 2099-2112.

Kim, S. H. (2020). Multiple leak detection algorithm for pipe network. *Mechanical Systems and Signal Processing*, *139*, 106645.

Kim, S. H. (2022). Dimensionless impedance method for the transient response of pressurized pipeline system. *Engineering applications of computational fluid mechanics*, *16*(1), 1641-1654.

Lee, P., Tuck, J., Davidson, M., & May, R. (2017). Piezoelectric wave generation system for condition assessment of field water pipelines. *Journal of Hydraulic Research*, *55*(5), 721-730.

Lee, P. J. (2013). Energy analysis for the illustration of inaccuracies in the linear modelling of pipe fluid transients. *Journal of Hydraulic Research*, *51*(2), 133-144.

Lee, P. J., Lambert, M. F., Simpson, A. R., Vítkovský, J. P., & Liggett, J. (2006). Experimental verification of the frequency response method for pipeline leak detection. *Journal of Hydraulic Research*, *44*(5), 693-707.

Lee, P. J., Vítkovský, J. P., Lambert, M. F., Simpson, A. R., & Liggett, J. A. (2005a). Frequency domain analysis for detecting pipeline leaks. *Journal of hydraulic engineering*, *131*(7), 596-604.

Lee, P. J., Vítkovský, J. P., Lambert, M. F., Simpson, A. R., & Liggett, J. A. (2005b). Leak location using the pattern of the frequency response diagram in pipelines: A numerical study. *Journal of Sound and Vibration*, *284*(3-5), 1051-1073.

Lei, Y., Lin, J., He, Z., & Zuo, M. J. (2013). A review on empirical mode decomposition in fault diagnosis of rotating machinery. *Mechanical Systems and Signal Processing*, *35*(1-2), 108-126.

Li, R., Huang, H., Xin, K., & Tao, T. (2015). A review of methods for burst/leakage detection and location in water distribution systems. *Water Science and Technology: Water Supply*, *15*(3), 429-441.

Liemberger, R., & Marin, P. (2006). The challenge of reducing non-revenue water in developing countries--how the private sector can help: A look at performance-based service contracting.

Liemberger, R., & Wyatt, A. (2019). Quantifying the global non-revenue water problem. *Water Supply*, *19*(3), 831-837.

Liggett, A., & Chen, L. (1994). Inverse transient analysis in pipe networks. *Journal of hydraulic engineering*, *120*(8), 934-955.

Lin, J., Wang, X., & Ghidaoui, M. S. (2021). Multi-sensor fusion for transient-based pipeline leak localization in the dempster-shafer evidence framework. *Water Resources Research*, *57*(9).

Liou, C. P. (1998). Pipeline leak detection by impulse response extraction.

Lister, M. (1960). The numerical solution of hyperbolic partial differential equations by the method of characteristics. *Mathematical methods for digital computers*, *1*, 165-179.

Meniconi, S., Brunone, B., Ferrante, M., Capponi, C., Carrettini, C., Chiesa, C., Segalini, D., & Lanfranchi, E. (2015). Anomaly pre-localization in distribution–transmission mains by pump trip: preliminary field tests in the Milan pipe system. *Journal of Hydroinformatics*, *17*(3), 377-389.

Meyers, M. A., & Chawla, K. K. (2008). *Mechanical behavior of materials*. Cambridge university press.

Motazedi, N., & Beck, S. (2018). Leak detection using cepstrum of cross-correlation of transient pressure wave signals. *Proceedings of the Institution of Mechanical Engineers, Part C: Journal of Mechanical Engineering Science*, *232*(15), 2723-2735.

Mounce, S., & Boxall, J. (2010). Implementation of an on-line artificial intelligence district meter area flow meter data analysis system for abnormality detection: a case study. *Water Science and Technology: Water Supply*, *10*(3), 437-444.

Nguyen, S. T. N., Gong, J., Lambert, M. F., Zecchin, A. C., & Simpson, A. R. (2018). Least squares deconvolution for leak detection with a pseudo random binary sequence excitation. *Mechanical Systems and Signal Processing*, *99*, 846-858.

Nixon, W., Ghidaoui, M., & Kolyshkin, A. (2006). Range of validity of the transient damping leakage detection method. *Journal of hydraulic engineering*, *132*(9), 944-957.

Norooz, R., Shamloo, H., & Mousavıfard, M. (2015). A review of one-dimensional unsteady friction models for transient pipe flow. *Cumhuriyet Üniversitesi Fen Edebiyat Fakültesi Fen Bilimleri Dergisi*, *36*(3), 2278-2288.

Ofwat. (2024). *Overview of Thames Water's PR24 final determination*. The Water

Services Regulation Authority

Ostfeld, A., Uber, J. G., Salomons, E., Berry, J. W., Hart, W. E., Phillips, C. A., Watson, J.-P., Dorini, G., Jonkergouw, P., & Kapelan, Z. (2008). The battle of the water sensor networks (BWSN): A design challenge for engineers and algorithms. *Journal of Water Resources Planning and Management*, *134*(6), 556-568.

Pan, B., Capponi, C., Meniconi, S., Brunone, B., & Duan, H.-F. (2022). Efficient leak detection in single and branched polymeric pipeline systems by transient wave analysis. *Mechanical Systems and Signal Processing*, *162*, 108084.

Pan, B., Duan, H.-F., Meniconi, S., & Brunone, B. (2021). FRF-based transient wave analysis for the viscoelastic parameters identification and leak detection in water-filled plastic pipes. *Mechanical Systems and Signal Processing*, *146*, 107056.

Pan, B., Duan, H., Meniconi, S., Urbanowicz, K., Che, T., & Brunone, B. (2020). Multistage frequency-domain transient-based method for the analysis of viscoelastic parameters of plastic pipes. *Journal of hydraulic engineering*, *146*(3), 04019068.

Puust, R., Kapelan, Z. S., Savic, D. A., & Koppel, T. (2010). A review of methods for leakage management in pipe networks. *Urban Water Journal*, *7*(1), 25-45.

Qin, H.-P., Su, Q., & Khu, S.-T. (2011). An integrated model for water management in a rapidly urbanizing catchment. *Environmental modelling & software*, *26*(12), 1502-1514.

Raychaudhuri, S. (2008). Introduction to monte carlo simulation. 2008 Winter simulation conference,

Sarkamaryan, S., Haghighi, A., & Adib, A. (2018). Leakage detection and calibration of pipe networks by the inverse transient analysis modified by Gaussian functions for leakage simulation. *Journal of Water Supply: Research and Technology—AQUA*, *67*(4), 404-413.

Schohl, G. (1993). Improved approximate method for simulating frequency-dependent friction in transient laminar flow.

Shamloo, H., & Haghighi, A. (2010). Optimum leak detection and calibration of pipe networks by inverse transient analysis. *Journal of Hydraulic Research*, *48*(3), 371-376.

Shucksmith, J. D., Boxall, J. B., Staszewski, W. J., Seth, A., & Beck, S. B. (2012). Onsite leak location in a pipe network by cepstrum analysis of pressure transients. *Journal-American Water Works Association*, *104*(8), E457-E465.

Soares, A. K., Covas, D. I., & Reis, L. F. R. (2011). Leak detection by inverse transient analysis in an experimental PVC pipe system. *Journal of Hydroinformatics*, *13*(2), 153-166.

Sun, J., Wang, R., & Duan, H.-F. (2016). Multiple-fault detection in water pipelines using transient-based time-frequency analysis. *Journal of Hydroinformatics*, *18*(6), 975-989.

Suo, L., & Wylie, E. (1989). Impulse response method for frequency-dependent pipeline transients.

Taghvaei, M., Beck, S., & Staszewski, W. (2006). Leak detection in pipelines using cepstrum analysis. *Measurement Science and Technology*, *17*(2), 367.

Tjuatja, V., Keramat, A., Pan, B., Duan, H.-F., Brunone, B., & Meniconi, S. (2023). Transient flow modeling in viscoelastic pipes: A comprehensive review of literature and analysis. *Physics of Fluids*, *35*(8).

Trikha, A. K. (1975). An efficient method for simulating frequency-dependent friction in transient liquid flow.

Urbanowicz, K., Duan, H.-F., & Bergant, A. (2020). Transient liquid flow in plastic pipes. *J. Mech. Eng*, *66*, 77-90.

Vardy, A. E., & Brown, J. M. (1995). Transient, turbulent, smooth pipe friction. *Journal of Hydraulic Research*, *33*(4), 435-456.

Vardy, A. E., & Brown, J. M. (2004). Transient turbulent friction in fully rough pipe flows. *Journal of Sound and Vibration*, *270*(1-2), 233-257.

Vardy, A. E., & Hwang, K.-L. (1991). A characteristics model of transient friction in pipes. *Journal of Hydraulic Research*, *29*(5), 669-684.

Vítkovský, J. P., Bergant, A., Simpson, A. R., & Lambert, M. F. (2006). Systematic evaluation of one-dimensional unsteady friction models in simple pipelines. *Journal of hydraulic engineering*, *132*(7), 696-708.

Vítkovský, J. P., Lambert, M. F., Simpson, A. R., & Bergant, A. (2000). Advances in unsteady friction modelling in transient pipe flow. Proc., 8th Int. Conf. on Pressure Surges,

Vítkovský, J. P., Lambert, M. F., Simpson, A. R., & Liggett, J. A. (2007). Experimental observation and analysis of inverse transients for pipeline leak detection. *Journal of Water Resources Planning and Management*, *133*(6), 519-530.

Vítkovský, J. P., Simpson, A. R., & Lambert, M. F. (2000). Leak detection and calibration using transients and genetic algorithms. *Journal of Water Resources Planning and Management*, *126*(4), 262-265.

Wang, X.-J., Lambert, M. F., Simpson, A. R., Liggett, J. A., & Vítkovský, J. P. (2002). Leak detection in pipelines using the damping of fluid transients. *Journal of hydraulic engineering*, *128*(7), 697-711.

Wang, X. (2021). Uncertainty quantification and global sensitivity analysis for transient wave propagation in pressurized pipes. *Water Resources Research*, *57*(4), Article e2020WR028975.

Wang, X., Camino, G. A., Che, T.-C., & Ghidaoui, M. S. (2021). Factorized wave propagation model in tree-type pipe networks and its application to leak localization. *Mechanical Systems and Signal Processing*, *147*.

Wang, X., & Ghidaoui, M., S. (2018). Pipeline leak detection using the matched-field processing method. *Journal of hydraulic engineering*, *144*(6), 04018030.

Wang, X., & Ghidaoui, M. S. (2018). Identification of multiple leaks in pipeline: Linearized model, maximum likelihood, and super-resolution localization. *Mechanical Systems and Signal Processing*, *107*, 529-548.

Wang, X., & Ghidaoui, M. S. (2019). Identification of multiple leaks in pipeline II: Iterative beamforming and leak number estimation. *Mechanical Systems and Signal Processing*, *119*, 346-362.

Wang, X., & Ghidaoui, M. S. (2021). Leak detection in viscoelastic pipes by matched-field processing method. In: Google Patents.

Wang, X., Ghidaoui, M. S., & Lin, J. (2019). Identification of multiple leaks in pipeline III: Experimental results. *Mechanical Systems and Signal Processing*, *130*, 395-408.

Wang, X., Lin, J., Keramat, A., Ghidaoui, M. S., Meniconi, S., & Brunone, B. (2019). Matched-field processing for leak localization in a viscoelastic pipe: An experimental study. *Mechanical Systems and Signal Processing*, *124*, 459-478.

Wang, X., Waqar, M., Yan, H.-C., Louati, M., Ghidaoui, M. S., Lee, P. J., Meniconi, S., Brunone, B., & Karney, B. (2020). Pipeline leak localization using matched-field processing incorporating prior information of modeling error. *Mechanical Systems and Signal Processing*, *143*, 106849.

Waqar, M., Louati, M., & Ghidaoui, M. S. (2023). Time-reversal technique for pipeline defect detection. *Water research*, *243*, 120375.

Waqar, M., Louati, M., Wang, X., & Ghidaoui, M. S. (2021). Model-free matched field processing for condition assessment of pressurized pipes. *Journal of Water Resources Planning and Management*, *147*(10), 04021066.

Wineman, A. S., & Rajagopal, K. R. (2000). *Mechanical response of polymers: an introduction*. Cambridge university press.

Wu, H., Duan, H.-F., Lai, W. W., Zhu, K., Cheng, X., Yin, H., Zhou, B., Lai, C.-C., Lu, C., & Ding, X. (2023). Leveraging optical communication fiber and AI for distributed water pipe leak detection. *IEEE Communications Magazine*, *62*(2), 126-132.

Wylie, E. B., Streeter, V. L., & Suo, L. (1993). *Fluid transients in systems* (Vol. 1). Prentice Hall Englewood Cliffs, NJ.

Ye, J., Zeng, W., Do, N. C., & Lambert, M. (2024). Reconstructing transient pressures in pipe networks from local observations by using physics-informed neural networks. *Water research*, *257*, 121648.

Zaman, D., Tiwari, M. K., Gupta, A. K., & Sen, D. (2020). A review of leakage detection strategies for pressurised pipeline in steady-state. *Engineering Failure Analysis*, *109*, 104264.

Zeng, W., Lambert, M. F., Gong, J. Z., Zecchin, A. C., Cazzolato, B. S., & Simpson, A. R. (2024). Anomaly Detection in Targeted Pipe Sections in Water Pipe Systems Using Hydroacoustic Signal Deconvolution. *Journal of hydraulic engineering*, *150*(1), Article 04023059.

Zettili, N. (2009). Quantum mechanics: concepts and applications.

Zhang, C., Gong, J., Zecchin, A., Lambert, M., & Simpson, A. (2018). Faster inverse transient analysis with a head-based method of characteristics and a flexible computational grid for pipeline condition assessment. *Journal of hydraulic engineering*, *144*(4), 04018007.

Zhang, C., Zecchin, A. C., Lambert, M. F., Gong, J., & Simpson, A. R. (2018). Multi-stage parameter-constraining inverse transient analysis for pipeline condition assessment. *Journal of Hydroinformatics*, *20*(2), 281-300.

Zhang, Y., Duan, H.-F., Keramat, A., & Che, T.-C. (2022). On the leak-induced transient wave reflection and dominance analysis in water pipelines. *Mechanical Systems and Signal Processing*, *167*, 108512.

Zhao, M., & Ghidaoui, M. (2006). Investigation of turbulence behavior in pipe transient using ak–∊ model. *Journal of Hydraulic Research*, *44*(5), 682-692.

Zielke, W. (1968). Frequency-dependent friction in transient pipe flow.

APPENDIX

Appendix A. Detailed Derivation of Leak Parameter Separation Method

As mentioned in the former methodology part, leak related transient signal $\Delta\mathbf{h} = s^L \mathcal{G}(x^L) + \mathbf{n}$, where the noise $\mathbf{n}$ is a white noise with the Gaussian distribution $\mathcal{N}(0, \sigma^2 \mathbf{I}_J)$. As a result, $\Delta\mathbf{h} \sim \mathcal{N}(s^L \mathcal{G}(x^L), \sigma^2 \mathbf{I}_J)$. Thus, the probability density function (PDF) of $\Delta\mathbf{h}$ is:

$$F(\Delta\mathbf{h}) = \frac{1}{\sqrt{2\pi\sigma^2}} e^{-\frac{\left|\Delta\mathbf{h} - s^L \mathcal{G}(x^L)\right|^2}{2\sigma}} \tag{A1}$$

The likelihood function of $\Delta\mathbf{h}$ can be expressed as

$$L(x^L, s^L) = \prod_{J=1}^{J} F(\Delta h, x^L, s^L) = \left(\frac{1}{\sqrt{2\pi\sigma^2}}\right)^J e^{-\sum_{J=1}^{J} \frac{\left|\Delta h - s^L \mathcal{G}(x^L)\right|^2}{2\sigma}} \tag{A2}$$

The log likelihood function is

$$\ln L(x^L, s^L) = J \ln\left(\frac{1}{\sqrt{2\pi\sigma^2}}\right) + \left(-\sum_{J=1}^{J} \frac{\left|\Delta h - s^L \mathcal{G}(x^L)\right|^2}{2\sigma}\right) \tag{A3}$$

The optimal solution for leak location and size is

$$\begin{aligned}\{\hat{x}^L, \hat{s}^L\} &= \arg\max_{x^L, s^L} \left(\ln L(x^L, s^L) \right) \\ &= \arg\max_{x^L, s^L} \left(-\sum_{J=1}^{J} \frac{\left| \Delta h - s^L \mathcal{G}(x^L) \right|^2}{2\sigma} \right) \\ &= \arg\max_{x^L, s^L} \left(-\sum_{J=1}^{J} \left| \Delta h - s^L \mathcal{G}(x^L) \right|^2 \right) \\ &= \arg\min_{x^L, s^L} \left\| \Delta \mathbf{h} - s^L \boldsymbol{\mathcal{G}}(x^L) \right\|_2^2 \end{aligned} \tag{A4}$$

Let F denote the norm function $\left\| \Delta \mathbf{h} - s^L \boldsymbol{\mathcal{G}}(x^L) \right\|_2^2$,

$$\begin{aligned} F &= \left\| \Delta \mathbf{h} - s^L \boldsymbol{\mathcal{G}}(x^L) \right\|_2^2 \\ &= \left(\Delta \mathbf{h} - s^L \boldsymbol{\mathcal{G}}(x^L) \right)^T \left(\Delta \mathbf{h} - s^L \boldsymbol{\mathcal{G}}(x^L) \right) \\ &= \Delta \mathbf{h}^T \Delta \mathbf{h} - s^L \boldsymbol{\mathcal{G}}^T(x^L) \Delta \mathbf{h} - s^L \Delta \mathbf{h}^T \boldsymbol{\mathcal{G}}(x^L) + (s^L)^2 \boldsymbol{\mathcal{G}}^T(x^L) \boldsymbol{\mathcal{G}}(x^L) \end{aligned} \tag{A5}$$

Due to the properties of the dot product, $\boldsymbol{\mathcal{G}}(x^L)^T \Delta \mathbf{h} = \Delta \mathbf{h}^T \boldsymbol{\mathcal{G}}(x^L)$ .Therefore, Eq. (A5) can be further simplified as

$$F = \Delta \mathbf{h}^T \Delta \mathbf{h} - 2 s^L \boldsymbol{\mathcal{G}}^T(x^L) \Delta \mathbf{h} + (s^L)^2 \boldsymbol{\mathcal{G}}^T(x^L) \boldsymbol{\mathcal{G}}(x^L) \tag{A6}$$

When F reaches its minimum value, as indicated in Eq. (A4), its derivative becomes zero. That is

$$\frac{\partial F}{\partial s^L} = -2 \boldsymbol{\mathcal{G}}^T(x^L) \Delta \mathbf{h} + 2 s^L \boldsymbol{\mathcal{G}}^T(x^L) \boldsymbol{\mathcal{G}}(x^L) = 0 \tag{A7}$$

Solving Eq. (A7), the maximum likelihood estimation for leak size is

$$\hat{s}^L = \frac{\boldsymbol{\mathcal{G}}^T(x^L) \Delta \mathbf{h}}{\boldsymbol{\mathcal{G}}^T(x^L) \boldsymbol{\mathcal{G}}(x^L)} \tag{A8}$$

Substituting Eq. (A8) back to Eq. (A4), the maximum likelihood estimation for leak location is

$$\begin{aligned}\left\{\hat{x}^L\right\} &= \arg\min_{x^L}\left\|\Delta\mathbf{h} - \mathcal{G}(x^L)\frac{\mathcal{G}(x^L)^T\Delta\mathbf{h}}{\mathcal{G}(x^L)^T\mathcal{G}(x^L)}\right\|_2^2 \\ &= \arg\min_{x^L}\left(\Delta\mathbf{h} - \mathcal{G}(x^L)\frac{\mathcal{G}^T(x^L)\Delta\mathbf{h}}{\mathcal{G}^T(x^L)\mathcal{G}(x^L)}\right)^T\left(\Delta\mathbf{h} - \mathcal{G}(x^L)\frac{\mathcal{G}^T(x^L)\Delta\mathbf{h}}{\mathcal{G}^T(x^L)\mathcal{G}(x^L)}\right) \\ &= \arg\min_{x^L}\left(\Delta\mathbf{h}^T\Delta\mathbf{h} - 2\Delta\mathbf{h}^T\mathcal{G}(x^L)\frac{\mathcal{G}^T(x^L)\Delta\mathbf{h}}{\mathcal{G}^T(x^L)\mathcal{G}(x^L)} + \left(\mathcal{G}(x^L)\frac{\mathcal{G}^T(x^L)\Delta\mathbf{h}}{\mathcal{G}^T(x^L)\mathcal{G}(x^L)}\right)^T\left(\mathcal{G}(x^L)\frac{\mathcal{G}^T(x^L)\Delta\mathbf{h}}{\mathcal{G}^T(x^L)\mathcal{G}(x^L)}\right)\right)\end{aligned} \tag{A9}$$

To minimize Eq. (A9) is equivalent to maximizing the term $-2\Delta\mathbf{h}^T\mathcal{G}(x^L)\dfrac{\mathcal{G}(x^L)^T\Delta\mathbf{h}}{\mathcal{G}(x^L)^T\mathcal{G}(x^L)}$. Accordingly, Eq. (A9) is simplified, and the objective function of leak location is given

$$\begin{aligned}\left\{\hat{x}^L\right\} &= \arg\max_{x^L}\left(\Delta\mathbf{h}^T\mathcal{G}(x^L)\frac{\mathcal{G}^T(x^L)\Delta\mathbf{h}}{\mathcal{G}^T(x^L)\mathcal{G}(x^L)}\right) \\ &= \arg\max_{x^L}(B^2)\end{aligned} \tag{A10}$$

Appendix B. Detailed Derivation of the Iterative Beamforming Algorithm for Localizing Multiple Leaks

Let $\mathbf{\Phi} = \{\mathbf{x}^L, \mathbf{s}^L\}$ be the unknown leak parameter vector. Its log-likelihood function is

$$\ell(\mathbf{\Phi}) = \ln \mathcal{P}(\Delta\mathbf{h} \mid \mathbf{\Phi}) = \ln \sum_{\Delta\mathbf{h}} \mathcal{P}(\Delta\mathbf{h} \mid \Delta\mathbf{h}^L, \mathbf{\Phi}) \mathcal{P}(\Delta\mathbf{h}^L \mid \mathbf{\Phi}) \tag{B1}$$

The iterative beamforming algorithm maximizes $\ell(\mathbf{\Phi})$ through iterative procedures. Assume $\mathbf{\Phi}_{j-1}$ is the estimation of $\mathbf{\Phi}$ after $j-1$ iterations. The objective of a new iteration is to update $\mathbf{\Phi}$ by maximizing the following log-likelihood difference

$$\begin{aligned}
\ell(\mathbf{\Phi}) - \ell(\mathbf{\Phi}_{j-1}) &= \ln \sum_{\Delta\mathbf{h}^L} \mathcal{P}(\Delta\mathbf{h} \mid \Delta\mathbf{h}^L, \mathbf{\Phi}) \mathcal{P}(\Delta\mathbf{h}^L \mid \mathbf{\Phi}) - \ln \mathcal{P}(\Delta\mathbf{h} \mid \mathbf{\Phi}_{j-1}) \\
&= \ln \sum_{\Delta\mathbf{h}^L} \mathcal{P}(\Delta\mathbf{h}^L \mid \Delta\mathbf{h}, \mathbf{\Phi}_{j-1}) \frac{\mathcal{P}(\Delta\mathbf{h} \mid \Delta\mathbf{h}^L, \mathbf{\Phi}) \mathcal{P}(\Delta\mathbf{h}^L \mid \mathbf{\Phi})}{\mathcal{P}(\Delta\mathbf{h}^L \mid \Delta\mathbf{h}, \mathbf{\Phi}_{j-1})} - \ln \mathcal{P}(\Delta\mathbf{h} \mid \mathbf{\Phi}_{j-1}) \\
&\geq \sum_{\Delta\mathbf{h}^L} \mathcal{P}(\Delta\mathbf{h}^L \mid \Delta\mathbf{h}, \mathbf{\Phi}_{j-1}) \ln \frac{\mathcal{P}(\Delta\mathbf{h} \mid \Delta\mathbf{h}^L, \mathbf{\Phi}) \mathcal{P}(\Delta\mathbf{h}^L \mid \mathbf{\Phi})}{\mathcal{P}(\Delta\mathbf{h}^L \mid \Delta\mathbf{h}, \mathbf{\Phi}_{j-1})} - \ln \mathcal{P}(\Delta\mathbf{h} \mid \mathbf{\Phi}_{j-1}) \\
&= \sum_{\Delta\mathbf{h}^L} \mathcal{P}(\Delta\mathbf{h}^L \mid \Delta\mathbf{h}, \mathbf{\Phi}_{j-1}) \ln \frac{\mathcal{P}(\Delta\mathbf{h} \mid \Delta\mathbf{h}^L, \mathbf{\Phi}) \mathcal{P}(\Delta\mathbf{h}^L \mid \mathbf{\Phi})}{\mathcal{P}(\Delta\mathbf{h}^L \mid \Delta\mathbf{h}, \mathbf{\Phi}_{j-1}) \mathcal{P}(\Delta\mathbf{h} \mid \mathbf{\Phi}_{j-1})}
\end{aligned} \tag{B2}$$

The "≥" sign in Eq. (B2) is achieved by Jensen's inequality given $\mathcal{P}(\Delta\mathbf{h}^L \mid \Delta\mathbf{h}, \mathbf{\Phi}_{j-1}) \geq 0$ and $\sum_{\Delta\mathbf{h}^L} \mathcal{P}(\Delta\mathbf{h}^L \mid \Delta\mathbf{h}, \mathbf{\Phi}_{j-1}) = 1$.

Eq. (B2) can be rewritten as

$$\ell(\mathbf{\Phi}) \geq \ell(\mathbf{\Phi}_{j-1}) + \sum_{\Delta\mathbf{h}^L} \mathcal{P}(\Delta\mathbf{h}^L \mid \Delta\mathbf{h}, \mathbf{\Phi}_{j-1}) \ln \frac{\mathcal{P}(\Delta\mathbf{h} \mid \Delta\mathbf{h}^L, \mathbf{\Phi}) \mathcal{P}(\Delta\mathbf{h}^L \mid \mathbf{\Phi})}{\mathcal{P}(\Delta\mathbf{h}^L \mid \Delta\mathbf{h}, \mathbf{\Phi}_{j-1}) \mathcal{P}(\Delta\mathbf{h} \mid \mathbf{\Phi}_{j-1})} := \mathcal{Q}(\mathbf{\Phi} \mid \mathbf{\Phi}_{j-1}) \tag{B3}$$

Eq. (B3) implies that the log-likelihood function $\ell(\mathbf{\Phi})$ is the upper bound of

$\mathcal{Q}(\mathbf{\Phi} \mid \mathbf{\Phi}_{j-1})$. It is interesting that when $\mathbf{\Phi}$ = $\mathbf{\Phi}_{j-1}$, the functions $\ell(\mathbf{\Phi})$ and $\mathcal{Q}(\mathbf{\Phi} \mid \mathbf{\Phi}_{j-1})$ are equal. Formally, this is expressed as

$$\begin{aligned}\mathcal{Q}(\Phi_{j-1} \middle| \Phi_{j-1}) &= \ell(\Phi_{j-1}) + \sum_{\Delta\mathbf{h}^L} \mathcal{P}(\Delta\mathbf{h}^L \mid \Delta\mathbf{h}, \Phi_{j-1}) \ln \frac{\mathcal{P}(\Delta\mathbf{h} \mid \Delta\mathbf{h}^L, \Phi_{j-1})\mathcal{P}(\Delta\mathbf{h}^L \mid \Phi_{j-1})}{\mathcal{P}(\Delta\mathbf{h}^L \mid \Delta\mathbf{h}, \Phi_{j-1})\mathcal{P}(\Delta\mathbf{h} \mid \Phi_{j-1})} \\ &= \ell(\mathbf{\Phi}_{j-1}) + \sum_{\Delta\mathbf{h}^L} \mathcal{P}(\Delta\mathbf{h}^L \mid \Delta\mathbf{h}, \mathbf{\Phi}_{j-1}) \ln 1 \\ &= \ell(\mathbf{\Phi}_{j-1})\end{aligned} \tag{B4}$$

The aim is to estimate the unknown leak parameter vector $\mathbf{\Phi}$ by maximizing $\ell(\mathbf{\Phi})$, whose explicit form is unavailable. Fortunately, Equations B3 and B4 shows that $\ell(\mathbf{\Phi})$ is the upper bound of $\mathcal{Q}(\mathbf{\Phi} \mid \mathbf{\Phi}_{j-1})$ and that the values of $\ell(\mathbf{\Phi})$ and $\mathcal{Q}(\mathbf{\Phi} \mid \mathbf{\Phi}_{j-1})$ are equal at $\mathbf{\Phi}$ = $\mathbf{\Phi}_{j-1}$. Therefore, any adjustment to $\mathbf{\Phi}$ that improves $\mathcal{Q}(\mathbf{\Phi} \mid \mathbf{\Phi}_{j-1})$ must improve $\ell(\mathbf{\Phi})$. To achieve the largest increase in $\ell(\mathbf{\Phi})$, the iterative beamforming selects the $\mathbf{\Phi}$ that maximizes $\mathcal{Q}(\mathbf{\Phi} \mid \mathbf{\Phi}_{j-1})$. The updated vector is denoted as $\mathbf{\Phi}_j$, which is obtained as

$$\begin{aligned}\mathbf{\Phi}_j &= \arg\max_{\mathbf{\Phi}} \{\mathcal{Q}(\mathbf{\Phi} \mid \mathbf{\Phi}_{j-1})\} \\ &= \arg\max_{\mathbf{\Phi}} \left\{ \ell(\mathbf{\Phi}_{j-1}) + \sum_{\Delta\mathbf{h}^L} \mathcal{P}(\Delta\mathbf{h}^L \mid \Delta\mathbf{h}, \mathbf{\Phi}_{j-1}) \ln \frac{\mathcal{P}(\Delta\mathbf{h} \mid \Delta\mathbf{h}^L, \mathbf{\Phi})\mathcal{P}(\Delta\mathbf{h}^L \mid \mathbf{\Phi})}{\mathcal{P}(\Delta\mathbf{h}^L \mid \Delta\mathbf{h}, \mathbf{\Phi}_{j-1})\mathcal{P}(\Delta\mathbf{h} \mid \mathbf{\Phi}_{j-1})} \right\} \\ &= \arg\max_{\mathbf{\Phi}} \left\{ \sum_{\Delta\mathbf{h}^L} \mathcal{P}(\Delta\mathbf{h}^L \mid \Delta\mathbf{h}, \mathbf{\Phi}_{j-1}) \ln\left[\mathcal{P}(\Delta\mathbf{h} \mid \Delta\mathbf{h}^L, \mathbf{\Phi})\mathcal{P}(\Delta\mathbf{h}^L \mid \mathbf{\Phi}) \right] \right\} \\ &= \arg\max_{\mathbf{\Phi}} \left\{ \sum_{\Delta\mathbf{h}^L} \mathcal{P}(\Delta\mathbf{h}^L \mid \Delta\mathbf{h}, \mathbf{\Phi}_{j-1}) \ln \mathcal{P}(\Delta\mathbf{h} \mid \Delta\mathbf{h}^L, \mathbf{\Phi}) \right\} \\ &= \arg\max_{\mathbf{\Phi}} \left\{ \mathbb{E}_{\Delta\mathbf{h}^L \mid \Delta\mathbf{h}, \mathbf{\Phi}_{j-1}} \left[\ln \mathcal{P}(\Delta\mathbf{h}, \Delta\mathbf{h}^L \mid \mathbf{\Phi}) \right] \right\} \\ &= \arg\max_{\mathbf{\Phi}} \left\{ \mathbb{E}_{\Delta\mathbf{h}^L \mid \Delta\mathbf{h}, \mathbf{\Phi}_{j-1}} \left[\ln \mathcal{P}(\Delta\mathbf{h}^L \mid \mathbf{\Phi}) + \ln \mathcal{P}(\Delta\mathbf{h} \mid \Delta\mathbf{h}^L) \right] \right\} \\ &= \arg\max_{\mathbf{\Phi}} \left\{ \mathbb{E}_{\Delta\mathbf{h}^L \mid \Delta\mathbf{h}, \mathbf{\Phi}_{j-1}} \left[\ln \mathcal{P}(\Delta\mathbf{h}^L \mid \mathbf{\Phi}) \right] \right\} \\ &= \underbrace{\arg\max_{\mathbf{\Phi}} \underbrace{\left\{ \mathbb{E}\left[\ell(\mathbf{\Phi} \mid \Delta\mathbf{h}^L) \mid \Delta\mathbf{h}, \mathbf{\Phi}_{j-1} \right] \right\}}_{\text{Step 1: expectation}}}_{\text{Step 2: maximization}}\end{aligned} \tag{B5}$$

Appendix C. Detailed Derivation of the Expectation Step

The conditional expectation in Eq. (B5) can be expressed as

$$\begin{aligned}
\mathbb{E}\left[\ell(\mathbf{\Phi} \mid \Delta\mathbf{h}^{L}) \mid \Delta\mathbf{h}, \mathbf{\Phi}_{j-1}\right] &= \mathbb{E}\left[-\sum_{n=1}^{N}\left\|\Delta\mathbf{h}^{L_n} - s^{L_n}\mathcal{G}(x^{L_n})\right\|_2^2 \mid \Delta\mathbf{h}, \mathbf{\Phi}_{j-1}\right] \\
&= -\sum_{n=1}^{N}\mathbb{E}\left[\left\|\Delta\mathbf{h}^{L_n} - s^{L_n}\mathcal{G}(x^{L_n})\right\|_2^2 \mid \Delta\mathbf{h}, \mathbf{\Phi}_{j-1}\right] \\
&= -\sum_{n=1}^{N}\left\{\left\|\mathbb{E}(\Delta\mathbf{h}^{L_n} \mid \Delta\mathbf{h}, \mathbf{\Phi}_{j-1}) - s^{L_n}\mathcal{G}(x^{L_n})\right\|_2^2 + \mathrm{Tr}[\mathrm{Cov}(\Delta\mathbf{h}^{L_n} \mid \Delta\mathbf{h}, \mathbf{\Phi}_{j-1})]\right\} \\
&= -\sum_{n=1}^{N}\left\|\mathbb{E}(\Delta\mathbf{h}^{L_n} \mid \Delta\mathbf{h}, \mathbf{\Phi}_{j-1}) - s^{L_n}\mathcal{G}(x^{L_n})\right\|_2^2 + c
\end{aligned} \tag{C1}$$

$(\Delta\mathbf{h}, \Delta\mathbf{h}^{L_n})^T$ follows a multivariate Gaussian distribution with mean 0 and covariance matrix.

$$\mathbf{\Sigma} = \begin{bmatrix} \mathrm{Cov}(\Delta\mathbf{h}) & \mathrm{Cov}(\Delta\mathbf{h}, \Delta\mathbf{h}^{L_n}) \\ \mathrm{Cov}(\Delta\mathbf{h}^{L_n}, \Delta\mathbf{h}) & \mathrm{Cov}(\Delta\mathbf{h}^{L_n}) \end{bmatrix} = \sigma^2 \begin{bmatrix} \mathbf{I} & \frac{1}{N}\mathbf{I} \\ \frac{1}{N}\mathbf{I} & \frac{1}{N}\mathbf{I} \end{bmatrix} \tag{C2}$$

Let **X** and **Y** be Gaussian random vectors with means $\mu_{\mathbf{X}}$ and $\mu_{\mathbf{Y}}$ and covariance matrices $\Sigma_{\mathbf{XX}}$ and $\Sigma_{\mathbf{YY}}$, respectively. Let $\Sigma_{\mathbf{XY}}$ = Cov(**X**,**Y**) and $\Sigma_{\mathbf{YX}}$ = Cov(**Y**,**X**), the conditional probability density function follows a Gaussian distribution is

$$\mathcal{P}(\mathbf{X} \mid \mathbf{Y}) \sim \mathcal{N}\left(\mu_{\mathbf{X|Y}}, \Sigma_{\mathbf{X|Y}}\right) = \mathcal{N}\left[\mu_{\mathbf{X}} + \Sigma_{\mathbf{XY}}\Sigma_{\mathbf{YY}}^{-1}(\mathbf{Y} - \mu_{\mathbf{Y}}), \Sigma_{\mathbf{XX}} - \Sigma_{\mathbf{XY}}\Sigma_{\mathbf{YY}}^{-1}\Sigma_{\mathbf{YX}}\right] \tag{C3}$$

Similarly, the conditional distribution of $\Delta\mathbf{h}^{Ln}$ given $\Delta\mathbf{h}$ also follows the Gaussian distribution

$$\begin{aligned}
\mathcal{P}(\Delta\mathbf{h}^{L_n} \middle| \Delta\mathbf{h}) &\sim \mathcal{N}\left(\mu_{\Delta\mathbf{h}^{L_n}|\Delta\mathbf{h}}, \Sigma_{\Delta\mathbf{h}^{L_n}|\Delta\mathbf{h}}\right) \\
&= \mathcal{N}\left\{s^{L_n}\mathcal{G}(x^{L_n}) + \frac{1}{N}\left[\Delta\mathbf{h} - \mathbf{s}^{L}\mathcal{G}(\mathbf{x}^{L})\right], \sigma^2\frac{N-1}{N^2}\mathbf{I}\right\}
\end{aligned} \tag{C4}$$

Hence,

$$\mathbb{E}(\Delta\mathbf{h}^{L_n} \mid \Delta\mathbf{h}, \mathbf{\Phi}_{j-1}) = s_{j-1}^{L_n}\mathcal{G}(x_{j-1}^{L_n}) + \frac{1}{N}\left[\Delta\mathbf{h} - \mathbf{s}_{j-1}^{L}\mathcal{G}(\mathbf{x}_{j-1}^{L})\right] := \Delta\mathbf{h}_j^{L_n} \tag{C5}$$

where $\Delta\mathbf{h}_j^{L_n}$ is the optimal decomposed wave signals.

Therefore, Eq. (C1) becomes

$$\mathbb{E}\left[\ell(\mathbf{\Phi} \mid \Delta\mathbf{h}^{L}) \mid \Delta\mathbf{h}, \mathbf{\Phi}_{j-1}\right] = -\sum_{n=1}^{N}\left\|\Delta\mathbf{h}_j^{L_n} - s^{L_n}\mathcal{G}(x^{L_n})\right\|_2^2 + c \tag{C6}$$